



저작자표시-비영리 2.0 대한민국

이용자는 아래의 조건을 따르는 경우에 한하여 자유롭게

- 이 저작물을 복제, 배포, 전송, 전시, 공연 및 방송할 수 있습니다.
- 이차적 저작물을 작성할 수 있습니다.

다음과 같은 조건을 따라야 합니다:



저작자표시. 귀하는 원저작자를 표시하여야 합니다.



비영리. 귀하는 이 저작물을 영리 목적으로 이용할 수 없습니다.

- 귀하는, 이 저작물의 재이용이나 배포의 경우, 이 저작물에 적용된 이용허락조건을 명확하게 나타내어야 합니다.
- 저작권자로부터 별도의 허가를 받으면 이러한 조건들은 적용되지 않습니다.

저작권법에 따른 이용자의 권리는 위의 내용에 의하여 영향을 받지 않습니다.

이것은 [이용허락규약\(Legal Code\)](#)을 이해하기 쉽게 요약한 것입니다.

[Disclaimer](#) 

공학박사학위논문

비압축성 해석의 안정성을 고려한
향상된 혼합 유한요소법 개발

**Development of an enhanced mixed finite
element method considering the stability
in incompressible analysis**

2022년 2월

서울대학교 대학원
기계항공공학부
윤기석

비압축성 해석의 안정성을 고려한
향상된 혼합 유한요소법 개발

Development of an enhanced mixed finite element method
considering the stability in incompressible analysis

지도교수 김도년

이 논문을 공학박사 학위논문으로 제출함

2021년 10 월

서울대학교 대학원
기계항공공학부
윤기석

윤기석의 공학박사 학위논문을 인준함

2021년 12 월

위원장	김운영	(인)
부위원장	김도년	(인)
위원	윤병동	(인)
위원	Dhadwal, Manoj Kumar	(인)
위원	노건우	(인)

Abstract

The finite element analysis has provided a powerful numerical technique to solve complex boundary value problems in engineering field. Despite the robustness and effectiveness of the finite element analysis, the cumbersome meshing procedure limits the efficiency of the overall analysis procedure. The quadrilateral element or hexahedral meshing is challengeable for geometrically complex objects. Adopting high-order elements might increase the computational costs. Moreover, determining the adequate mesh refinement level or proper interpolation order requires additional effort. It would be optimal if we could achieve high accuracy solution using small number of low-order triangles, which would make the meshing process much simpler. For this reason we adopt the recently proposed overlapping element which shows high accuracy and insensitive to the mesh distortion.

The incompressible analysis is another challengeable subject in the aspect of computational efficiency, because when the displacement-pressure mixed formulation is introduced to solve eessible problem, the stability of mixed element becomes important. For this stability issue, the conventional mixed finite elements are, in general, confined to high-order elements, which could raise the computational cost.

In this study, we incorporated the overlapping element with the displacement-pressure mixed formulation to avoid the difficulty of meshing process and reduce the computational cost using low-order triangular meshes. In overlapping element, displacement-pressure mixed formulation is available using the low-order triangles or tetrahedrons due to its enlarged displacement space without breaking the stability. We present the available combinations of displacement and pressure variables, which are stable independent of mesh patterns. Also, we present the effective combinations which show more accuracy and efficiency compared to the conventional mixed finite elements. Finally, we present a practical three-dimensional problem introducing the new procedure for the protein dynamics. By adopting the mixed overlapping element in protein dynamics, we could reduce the computational cost significantly without loss of accuracy.

Keyword : Finite element analysis, Enhanced finite element, Overlapping element, Mixed formulation, Inf-Sup condition, Stability of mixed overlapping element

Student Number : 2016-33943

Contents

Abstract	1
Contents	2
List of Figures	5
List of Tables	10
Chapter 1 Introduction	12
1.1 Background and objectives	12
1.2 Research outline	16
Chapter 2 Introduction to the overlapping element	18
2.1 Introduction	18
2.2 Approximation of the displacement field in 2D domain	21
2.3 Approximation of the displacement field in 3D domain	27
Chapter 3 Displacement-pressure mixed formulation of overlapping element	33
3.1 Introduction	33
3.2 Construction of matrices for the mixed overlapping element	35
3.2.1 Matrices for 2D incompressible plane strain analysis	38
3.2.2 Matrices for 3D incompressible solid analysis.....	40
3.3 The approximation of the pressure field.....	42
Chapter 4 Stability of mixed overlapping element	47
4.1 Introduction	47
4.2 The inf-sup test.....	49
4.3 Numerical inf-sup test for a simple mechanical system.....	54
4.4 Conclusion	62

Chapter 5 Numerical examples in 2D domain.....	63
5.1 Introduction	63
5.2 Cantilever plate	64
5.3 Cook’s membrane.....	69
5.4 Thick circular beam.....	73
5.5 Thin circular beam	77
5.6 Conclusion	81
Chapter 6 Application to 3D problems : Protein dynamics.....	83
6.1 Introduction	83
6.2 Generating finite element models for protein dynamics	88
6.2.1 Finite element modeling of protein	88
6.2.2 Finite element modeling of solvent.....	91
6.2.3 Calculation of Friction matrix	92
6.3 Diffusion coefficients	94
6.3.1 Diffusion coefficient of a reference sphere	94
6.3.2 Diffusion coefficients of other proteins.....	98
6.4 Brownian dynamics simulation.....	102
6.4.1 Procedures for Brownian dynamics.	102
6.4.2 Results	103
6.4.3 Computational efficiency	109
6.5. Conclusion	115
Chapter 7 Concluding remark	116

Chapter A	Appendix.....	118
A1. Remarks on pressure interpolation		118
A2. The profiles of pressure and xx-stress		121
A3. The cantilever plate with material discontinuity		122
A4. Mesh filtering steps		124
A5. Calculation of the diffusion coefficients		125
A6. Integration of Brownian dynamics equation		127
Bibliography		129
Abstract in Korean.....		137

List of Figures

- Figure 2.1.** The local support I corresponding to node I of triangular element ε^e . The additional virtual nodes (nodes 4, 5, and 6) are marked as red dots.
- Figure 2.2.** Additional nodes (marked as red) for interpolation of Shepard functions on a tetrahedral overlapped region ε^e .
- Figure 3.1.** List of the conventional mixed finite elements.
- Figure 3.2.** List of the combinations of mixed finite overlapping elements with the discontinuous pressure field.
- Figure 3.3.** List of the combinations of mixed finite overlapping elements with the continuous pressure field.
- Figure 4.1.** The mechanical systems used for the numerical inf-sup test and the pressure distribution test.
- Figure 4.2.** The numerical inf-sup values, γ_h , of the conventional stable mixed finite elements depending on the mesh refinement. The letter ‘N’ denotes the total number of elements.
- Figure 4.3.** The pressure solutions of the conventional mixed element. Three different mesh patterns (striped, crossed, and Union-Jack pattern) are plotted for the triangular elements (Tri7/3 and Tri6/3c). A square pattern is used for the quadrilateral elements (Quad9/3, Quad9/4c).
- Figure 4.4.** The numerical inf-sup values, γ_h , of the mixed overlapping element formulated with the discontinuous pressure approximation, depending on the mesh refinement. The letter ‘N’ denotes the total number of elements.
- Figure 4.5.** The pressure solutions of the mixed overlapping element with the discontinuous pressure approximation. Three different mesh patterns (striped, crossed, and Union-Jack pattern) are tested for each combination of mixed overlapping element.

Figure 4.6. The numerical inf-sup values, γ_h , of the mixed overlapping element formulated with the continuous pressure approximation versus the mesh refinement. The letter ‘N’ denotes the total number of elements

Figure 4.7. The pressure solutions of the mixed overlapping element with the continuous pressure approximation. Three different mesh patterns (striped, crossed, and Union-Jack pattern) are tested for each combination of mixed overlapping element.

Figure 5.1. Description of the cantilever plate problem. The cantilever plate is under the normal pressure on the upper side with clamped boundary on the left side. A set of meshes used in the numerical test is also plotted below the problem description.

Figure 5.2. The strain energy error of cantilever plate problem. The convergence curve of (A) the conventional mixed finite elements and (B) the mixed overlapping elements in log scale. The percent error in strain energy of (C) the conventional mixed finite elements and (D) the mixed overlapping elements versus total number of the displacement degree of freedoms.

Figure 5.3. Description of the Cook’s membrane problem. The Cook’s membrane is under the tangential traction on the right side with clamped boundary on the left side. A set of meshes used in the numerical test is also plotted below the problem description.

Figure 5.4. The strain energy error of Cook’s membrane problem. The convergence curve of (A) the conventional mixed finite elements and (B) the mixed overlapping elements in log scale. The percent error of strain energy of (C) the conventional mixed finite elements and (D) the mixed overlapping elements versus total number of the displacement degree of freedoms.

Figure 5.5. Description of the thick circular beam problem. The thick circular beam is under the tangential traction on the upper left end with clamped boundary on the lower right end. A set of meshes used in the numerical test is also plotted below the problem description.

Figure 5.6. The strain energy error of thick circular beam problem. The convergence curve of (A) the conventional mixed finite elements and (B) the mixed overlapping elements in log scale. The percent error of strain energy of (C) the conventional mixed finite elements and (D) the mixed overlapping elements versus total number of the displacement degree of freedoms.

Figure 5.7. Description of the thin circular beam problem. The thin circular beam is under the tangential traction on the upper left end with clamped boundary on the lower right end. A set of meshes used in the numerical test is also plotted below the problem description.

Figure 5.8. The strain energy error of thin circular beam problem. The convergence curve of (A) the conventional mixed finite elements and (B) the mixed overlapping elements in log scale. The percent error of strain energy of (C) the conventional mixed finite elements and (D) the mixed overlapping elements versus total number of the displacement degree of freedoms.

Figure 6.1. Finite element framework for the protein dynamics simulation. The X-ray crystal structure of Taq polymerase (Protein Data Bank ID 1TAQ) (*top*) is obtained from the Protein Data Bank and its molecular surface is calculated. Then, the finite element models for solvent and protein body are defined to calculate the friction matrix and stiffness matrix (*middle*). The matrices can be used for the calculation of diffusion coefficients, Brownian dynamics simulation, and Brownian mode analysis (*bottom*).

- Figure 6.2.** Molecular surface of C-terminal domain of bamC protein (Protein Data Bank ID: 2YH5) modeled with different surface parameters. The protein modeled with finer surface parameter (*left*) captures the detailed characteristic shapes of the protein than the protein modeled with coarse surface parameter (*right*).
- Figure 6.3.** The cross-section of the mesh between the protein (Taq Polymerase) surface and the sphere. (A) All the eleven layers of the mesh are shown. (B) Only the two innermost layers of the mesh are shown.
- Figure 6.4.** The cross-section of the mesh between the inner and outer spherical surfaces. (A) All the eleven layers of the mesh are shown. (B) Only the two innermost layers of the mesh are shown.
- Figure 6.5.** The root-mean-square fluctuations (RMSFs) of residues of Taq polymerase obtained using the Brownian dynamics (BD) trajectories compared with those calculated using the molecular dynamics (MD) simulation. The Brownian dynamics trajectories are obtained from (A) the conventional procedure (Tet10/1+Tet10) and (B) the new procedure (OL4/1+Tet4).
- Figure 6.6.** The root-mean-square fluctuations (RMSFs) of residues of Lysozyme obtained using the Brownian dynamics (BD) trajectories compared with those calculated using the molecular dynamics (MD) simulation. The Brownian dynamics trajectories are obtained from (A) the conventional procedure (Tet10/1+Tet10) and (B) the new procedure (OL4/1+Tet4).
- Figure 6.7.** The root-mean-square fluctuations (RMSFs) of residues of GroEL obtained the molecular dynamics (MD) simulation. The Brownian dynamics trajectories are obtained from (A) the conventional procedure (Tet10/1+Tet10) and (B) the new procedure (OL4/1+Tet4).

Figure 6.8. The comparisons of (A) the number of nodes and (B) the computational time between two different procedures for the Brownian dynamics simulation. Brownian dynamics for both procedures were simulated using the same computational machine (Intel® Xeon® CPU E-5-2407 with 2.2GHz (CPU)).

Figure A1.1. The numerical inf-sup values of the mixed overlapping element formulated with the continuous pressure approximated by the standard linear shape functions.

Figure A1.2. The numerical inf-sup values of the mixed overlapping element formulated with the continuous pressure approximated by the overlapping element enriched by linear polynomial basis.

Figure A1.3. The numerical inf-sup values of the mixed overlapping element formulated with the continuous pressure approximated by the overlapping element enriched by bilinear polynomial basis.

Figure A1.4. The convergence curve of the mixed overlapping element formulated with the continuous pressure approximated by (A) the standard linear shape functions (B) the modified shape function of linearly enriched overlapping element (C) the modified shape function of bilinearly enriched overlapping element.

Figure A2.1. The distribution of pressure calculated from the pressure solution.

Figure A2.2. The distribution of xx-stress (τ_{xx}) calculated from the displacement solution

Figure A3.1. Description of the cantilever plate problem with material discontinuity. A set of meshes used in the numerical test is also plotted below the problem description.

Figure A3.2. The strain energy error of cantilever plate problem with material discontinuity. The convergence curve of (A) the conventional mixed finite elements and (B) the mixed overlapping elements in log scale.

Figure A3.3 The distribution of pressure when material discontinuity are present.

List of Tables

- Table 2.1.** Nodal values used in interpolating Shepard functions on a triangular element.
- Table 2.2.** Nodal values used in interpolating Shepard functions on a tetrahedral element.
- Table 5.1.** The percent error of the cantilever plate problem compared with the number of displacement degree of freedoms.
- Table 5.2.** The percent error of the Cook's membrane problem compared with the number of displacement degree of freedoms.
- Table 5.3.** The percent error of the thick circular beam bending problem compared with the number of displacement degree of freedoms.
- Table 5.4.** The percent error of the thin circular beam bending problem compared with the number of displacement degree of freedoms.
- Table 6.1.** The comparison of solvent models for 'Tet10/1' and 'OL4/1'.
- Table 6.2.** The diffusion coefficients and percent errors of a reference sphere model calculated by 'Tet10/1' and 'OL4/1' models.
- Table 6.3.** The diffusion coefficients calculated by conventional 'Tet10/1' model and 'OL4/1' model. The experimental values are also included for 10 different proteins whose atomic structures are obtained from Protein Data Bank (PDB).
- Table 6.4.** The size of the stiffness matrix of the solvent FE model, and the size of the friction matrix of resulting friction matrix. The matrices calculated from 'Tet10/1' model and 'OL4/1' model are compared for ten different proteins.
- Table 6.5.** Pearson correlation of root-mean-square fluctuations of Taq polymerase obtained using the Brownian dynamics simulation with two different procedures and the molecular dynamics (MD) simulation.

- Figure 6.6.** The root-mean-square fluctuations (RMSFs) of residues of Lysozyme obtained using the Brownian dynamics (BD) trajectories compared with those calculated using the molecular dynamics (MD) simulation. The Brownian dynamics trajectories are obtained from (A) the conventional procedure (Tet10/1+Tet10) and (B) the new procedure (OL4/1+Tet4).
- Table 6.7.** Pearson correlation of root-mean-square fluctuations of GroEL obtained using the Brownian dynamics simulation with two different procedures and the molecular dynamics (MD) simulation.
- Table 6.8.** Analysis information of Brownian dynamics simulation and molecular dynamics simulation for Lysozyme.
- Table 6.9.** Analysis information of Brownian dynamics simulation and molecular dynamics simulation for Taq polymerase.
- Table 6.10.** Analysis information of Brownian dynamics simulation and molecular dynamics simulation for GroEL.

Chapter 1

Introduction

1.1 Background and objectives

The finite element analysis is a well-established numerical procedure, which have been widely used to solve complex boundary value problems appearing in engineering and scientific fields. Starting from 1940s with the classical approach of solid mechanics problems by replacing small portions of continuum by arrangement of simple elements¹⁻⁴, the method had been developed and simplified by considering small portions or ‘elements’ in a continuum behave in a simplified manner^{5, 6}. Clough first used the term ‘finite element’ for such numerical methods⁷. Well known for its robustness and effectiveness in the solution of boundary value problems, the finite element analysis has been extensively developed in the past 80 years ranging from analysis of solids, fluids, and multi-physics problems to solution of complex nonlinear problems⁸⁻¹³.

Despite the success of the finite element analysis, obtaining a good conformal mesh for solving problems remains a challenge. In engineering practice, the refinement level of mesh should be carefully determined as certain regions should be meshed fine enough if those regions contain steep stress gradient or singularities in geometry. It should be avoided that all the regions meshed too fine to avoid the excessive burden on available computational resources⁸. For some cases where the adaptive meshing is required, for example a large deformation analysis or crack analysis, the mesh can be distorted which might affect the solution negatively¹⁴. For another example, although the hexahedral element is commonly used for its

accuracy and efficiency, discretizing the complex geometries using the hexahedral mesh with the desired level of mesh refinement level requires a large effort, sometimes not available at all, whereas the discretization is straight-forward for tetrahedral mesh. Therefore, the meshing process requires an effortful judgement by a skilled engineer, which might make the process inefficient.

In order to avoid such difficulties in the meshing process, various alternative techniques have been presented. One way to avoid the difficult meshing process is using the meshless or meshfree method. Starting from the work of Belytschko et al.¹⁵, who presented the element-free Galerkin methods, the meshless technique have been developed until recently such as the smoothed particle hydrodynamics (SPH) method¹⁶ and the method of finite spheres¹⁷⁻²¹. However, these meshless or meshfree methods have limitations in directly adopting the standard numerical techniques well-established in traditional finite element analysis. For example, applying the boundary conditions or performing the numerical integration might require additional effort, and sometimes, the method might require additional artificial stability parameters.

Another approach is to enhance the performance of conventional finite elements by adopting the special enrichment functions to the conventional finite elements. The first approach have been presented in 1980s by Bathe and Almeida²²⁻²⁴ who adopted the enrichment function in pipe problems to describe the cubic behavior of ovalization. Later on, Bathe and Chaudhary²⁵ adopted the enrichment function to effectively describe the warping effects of beams. Moes and Belytschko²⁶ provided the concept of extended finite element (XFEM) which is based on the generalized finite element method (GFEM) and the partition of unity method (PUM)^{27, 28}. The extended finite element method adopted the enrichment functions to account for the presence of cracks or material discontinuities.

More recently, Kim and Bathe¹⁴ focused on a scheme to increase the convergence rate of the traditional low-order finite elements using 3-node triangular and 4-node tetrahedral elements in two- and three-dimensional domains, respectively. The authors adopt the underlying finite element mesh enriched by

interpolation covers to significantly increase the convergence rates of solution. Zhang and Bathe²⁹ had presented the improved version of such method, the overlapping element. The overlapping element incorporates the concept of the method of finite spheres (one kind of a meshless method) and the traditional finite elements enriched by interpolation covers²⁹⁻³². The overlapping element is proven to have more increased convergence rates and insensitive to the mesh distortions still using the low-order elements such as 3-node triangles and 4-node tetrahedrons. They also provided a new scheme of solution, so called ‘AMORE (automatic meshing with overlapping and regular elements)’ scheme. In AMORE paradigm^{29-31, 33, 34}, the traditional finite elements, such as low-order quadrilateral or hexahedral elements, are used for the interior domain and the triangular or tetrahedral overlapping element are used for the boundary domains in which the conventional quadrilateral or hexahedral meshing is restricted and still require a high solution accuracy regardless of the mesh distortion. Using the AMORE scheme, both the efficiency of meshing process and the accuracy of solution can be achieved. Since the overlapping element provides effective solutions using low-order meshes, it can provide effective tool for solving incompressible problems where the conventional low-order mesh are restricted.

Mixed finite element analysis is another important research area that has been developed and analyzed ranging from the classical contributions³⁵⁻³⁷ to more recent references^{8, 38-45}. Unlike the traditional finite element analysis incorporating the single variable (usually displacement) as unknown variables, mixed finite element analysis incorporates at least two variables as unknown variables (usually displacement and pressure). The mixed finite element formulation typically results in a linear algebraic system of the general form

$$\begin{bmatrix} \mathbf{A} & \mathbf{B}^T \\ \mathbf{B} & \mathbf{C} \end{bmatrix} \begin{Bmatrix} \mathbf{x} \\ \mathbf{y} \end{Bmatrix} = \begin{Bmatrix} \mathbf{f} \\ \mathbf{g} \end{Bmatrix} \quad (1.1)$$

where \mathbf{A} and \mathbf{B} are matrices and \mathbf{x} , \mathbf{y} , \mathbf{f} , and \mathbf{g} are vectors.

When the problem is discretized with the mixed formulation, another

important property apart from the solvability, should be considered to have a good solution, the stability. The stability of the linear system is assured by examining whether the matrix \mathbf{B} appearing in Eq.(1.1) satisfies a certain condition. This stability condition have been presented by Brezzi and Babuška^{38, 46, 47}, so called the inf-sup condition (or Brezzi-Babuška condition). Additionally, the numerical procedure have been presented by Chapelle and Bathe⁴⁸ for testing the inf-sup condition in pursuit of easy access to inf-sup condition for various finite elements developed.

By the strict requirements of the inf-sup condition, the available mixed combinations of number of unknown displacement variables and the number of pressure variables are confined to certain quantities. In general, this strict condition leads to use only the high-order elements for conventional mixed finite element, such as 4-node triangular, 10-node tetrahedral, 9-node quadrilateral, and 27-node hexahedral elements.

In this study, we focus on applying the overlapping element using low-order meshes, such as 3-node triangular and 4-node tetrahedral meshes to the displacement-pressure mixed formulation where the usage of low-order meshes is strictly restricted. Using the overlapping element, we expect the meshing process to be much simpler by using only triangular and tetrahedral discretization on the analyzed object. Also, we expect the overlapping element, for its enlarged displacement function spaces, to embrace the mixed pressure variables without breaking the stability condition. We present the effective combinations of displacement-pressure mixed overlapping element by testing various combinations of mixed overlapping elements. In addition, to show the effectiveness of the mixed overlapping element, we present a practical example of a three-dimensional problem introducing the new procedure of protein dynamics simulation using the mixed overlapping element. We expect to reduce the computational cost significantly without the loss of solution accuracy.

1.2 Research outline

In Chapter 2, we introduce the formulation of the overlapping element in two-dimensional domain. Then we expand the concept of overlapping element to three-dimensional domain using the similar process established in two-dimensional domain. Also, we present the new shape function vector calculated from the overlapping element for later use in construction of finite element matrices.

In Chapter 3, we present the concept of displacement-pressure mixed formulation with the procedure for constructing finite element matrices involving the displacement field obtained from the overlapping element. We introduce some traditional mixed finite elements, which have been proven to be stable. Also, we present the possible combinations of number of displacement variables and pressure variables for the mixed overlapping element which we expect to show stable solutions.

In Chapter 4, we introduce the numerical procedure for the inf-sup test applicable in the mixed overlapping element. Then, we examine the stability of presented mixed overlapping element by performing the numerical inf-sup test. In addition, we examine the pressure solution whether it shows a smooth and reasonable profile for each tested mixed overlapping element. The results for inf-sup test shows consistency with the results for the pressure distribution test. The mixed overlapping elements which pass the inf-sup test show the smooth and reasonable pressure distribution, whereas the mixed overlapping element which failed in the inf-sup test show the unphysical pressure distribution.

In Chapter 5, we present four numerical example problems in two-dimensional domain. We solve the example problems by using the stable mixed overlapping elements filtered out in the Chapter 4. Apart from the stability point of view, we present example problems to evaluate the accuracy and efficiency of mixed overlapping element in comparison with the conventional mixed finite elements. The results show that the linearly enriched overlapping element mixed with a single pressure variable shows effectiveness in general. For extreme cases, such as when bending of thin structures are considered, the quadratically enriched

overlapping element mixed with the continuous pressure variables shows effectiveness.

In Chapter 6, we show the effectiveness of the mixed overlapping element by applying it to a practical three-dimensional problem, a protein dynamics. The conventional finite element procedure for protein dynamics adopts the traditional high-order mixed finite elements for solving the incompressible solvent medium around the protein structure. However, by using the low-order mixed overlapping element for the incompressible model, we reduced the computational cost significantly without deteriorating the accuracy. This chapter provides the good example for showing the effectiveness of the mixed overlapping element.

Chapter 2

Introduction to the overlapping element

2.1 Introduction

Although the traditional finite element analysis is a powerful numerical technique that provides robust solutions for various engineering problems, it is often less accessible to general users due to the difficulties in the meshing process. The mesh refinement level should be carefully treated as a finer mesh is required for the regions with concentrated stress gradients or the regions across the geometries with singularities such as corners or interfaces of different parts. Additionally, when the structure of interest is to be discretized into quadrilateral or hexahedral elements with the predefined refinement level, it is often restricted to obtain the conformal hexahedral mesh of the arbitrary geometries by only using the desired range of number of elements. Using a simple triangular or tetrahedral discretization can be an alternative option, which is more accessible in the meshing process. However, the performance of such elements are relatively poorer than quadrilateral or hexahedral element, sometimes not available at all when analyzing, for example, incompressible structures⁸. So using a higher order element is required occasionally for triangular or tetrahedral meshes, and this causes the raise of the computational cost^{8, 38}. For these issues, generating a finite element model to solve engineering problem requires a careful judgement of a skilled engineer with severe amount of time.

To overcome the difficulties of meshing process without raising the computational cost, there have been many alternative approaches presented such as meshless methods, polygonal or polyhedral finite elements, etc^{15-18, 20, 21, 49, 50}. However, these alternative numerical methods still have limitations in that, for example, treating the boundary condition or numerical integration requires additional effort.

Overlapping element is another numerical technique that was proposed to reduce the effort of meshing process without raising the computational cost^{29-32, 34, 51, 52}. The overlapping is organized the combination of the traditional finite element method and the method of finite spheres (one kind of the meshless method). The simple triangular or tetrahedral mesh is used same as ones used in the lower-order triangular or tetrahedral element in the traditional finite element method. Since we use the simple triangular or tetrahedral mesh, the meshing process is as simple as the traditional finite element. Any arbitrary geometries can be discretized into triangular or tetrahedral mesh simply by using tessellation algorithms such as advancing front method⁵³ and Delaunay triangulation⁵⁴. The displacement field of overlapping element is approximated by using the modified local field functions adopting the concept of method of finite spheres. Since the displacement field can be expressed within a polynomial space, the numerical integration is straight forward as the traditional finite elements, which makes the integration process quite efficient. The newly proposed displacement field of overlapping element make it possible to have its solution to be more accurate even using the lower-order triangular and tetrahedral mesh. Also, the overlapping element is shown to be insensitive for the highly distorted meshes. The overlapping element can be used in combination with the traditional element. The finite element model can be generated computationally efficient even more by using the traditional element in a simple domain within a analyzed structure, and using the overlapping element in a complex domain, usually boundaries of geometry. The authors call this process the ‘AMORE paradigm (automatic meshing with overlapping and regular elements)’, see for example^{31, 33}. Regarding the advantages of overlapping element, it would be

a good alternative tool when solving the incompressible materials with complex geometry.

In this chapter, we introduce the formulation of overlapping element in two-dimensional domain presented most recently by Huang and Bathe³¹. Then, we expand the concept of overlapping element to three-dimensional domain using the similar process established in two-dimensional domain. Also, we present the new shape function vector calculated from the overlapping element for later use in construction of finite element matrices.

2.2 Approximation of the displacement field in 2D domain

Overlapping element uses a modified displacement field adopting the concepts of traditional finite element method⁸ and the method of finite spheres¹⁷⁻¹⁹. We use the similar mathematical notations from the original paper most recently proposed by Huang and Bathe³¹.

In the traditional finite element method, the displacement field is assumed to be the interpolation of several nodal unknowns attached to nodes of each element. In each local element, the displacement field is expressed as

$$u(\mathbf{x}) = \sum_{I=1}^q h_I(\mathbf{x}) u_I \quad (2.1)$$

where q denotes the number of nodes determined by the shape and the polynomial order of the element. The function, $h_I(\mathbf{x})$, is the nodal shape function corresponding to the node I . The symbol, u_I , is the nodal unknown variable which usually means the displacement in most elasticity problems.

In the overlapping element, the displacement field is expressed by the interpolation of local field functions, $\psi_I(\mathbf{x})$. The local field functions are the spatial functions over a local domain with its center located at the node I . The local field functions are interpolated by the shape functions, $h_I(\mathbf{x})$, which are the same shape functions for conventional three-node linear triangular element.

$$u(\mathbf{x}) = \sum_{I=1}^3 h_I(\mathbf{x}) \psi_I(\mathbf{x}) \quad (2.2)$$

The local field function, $\psi_I(\mathbf{x})$, is used instead of u_I in the overlapping element. The local field function is composed of the interpolated Shepard functions, $\phi_J^I(\mathbf{x})$, and a series of nodal unknowns, $u_J(\mathbf{x})$.

$$\psi_I(\mathbf{x}) = \sum_{J=1}^3 \phi_J^I(\mathbf{x}) u_J(\mathbf{x}) \quad (2.3)$$

The interpolated Shepard function, $\phi_J^I(\mathbf{x})$, is calculated by using nodal weight functions which will be described later on. The series of nodal unknowns $u_J(\mathbf{x})$ are nodal variables enriched by a set of predetermined polynomial basis and are expressed as following.

$$u_J(\mathbf{x}) = \sum_n p_n \hat{a}_{Jn} \quad (2.4)$$

Here, \hat{a}_{Jn} is the nodal unknown variables of corresponding polynomial order n and node J , and p_n is the polynomial term of n -th order polynomial basis.

$$p_n \in \mathbf{p}^T = [1 \quad x \quad y \quad xy \quad x^2 \quad y^2 \quad \dots]^T \quad (2.5)$$

For example, the series of nodal unknowns corresponding to the node J using linear, bilinear, and quadratic polynomial basis can be expressed as Eqs.(2.6, 2.7, and 2.8).

$$u_J(\mathbf{x}) = \hat{a}_{J1} + \hat{a}_{J2}\bar{x} + \hat{a}_{J3}\bar{y} \quad (2.6)$$

$$u_J(\mathbf{x}) = \hat{a}_{J1} + \hat{a}_{J2}\bar{x} + \hat{a}_{J3}\bar{y} + \hat{a}_{J4}\bar{x}\bar{y} \quad (2.7)$$

$$u_J(\mathbf{x}) = \hat{a}_{J1} + \hat{a}_{J2}\bar{x} + \hat{a}_{J3}\bar{y} + \hat{a}_{J4}\bar{x}\bar{y} + \hat{a}_{J5}\bar{x}^2 + \hat{a}_{J6}\bar{y}^2 \quad (2.8)$$

Here, \bar{x} (or \bar{y}) simply means the local coordinate attached to the node J (coordinates measured from node J), to avoid possible ill-conditioned matrices when calculating the stiffness matrices of large structures.

Calculation of the interpolated Shepard function in 2D domain

The interpolated Shepard functions, $\phi_j^I(\mathbf{x})$, can be any functions satisfying three criteria:

- i) Displacement compatibility along elements.
- ii) Partition of unity property ($\sum_j \phi_j^I = 1$).
- iii) Function of three weight functions located at three corner nodes of triangle.

In this study, we adopt the most recent version of interpolated Shepard functions which Huang and Bathe³¹ has presented. First, a circular region centered at node I with the radius defined by the maximum distance between the node I and the adjacent nodes (labeled as r_I^{\max} in the Figure 2.1) is defined. This circular region is called the local support I . Additionally the minimum distance between the node I and the adjacent nodes is labeled as r_I^{\min} for later use.

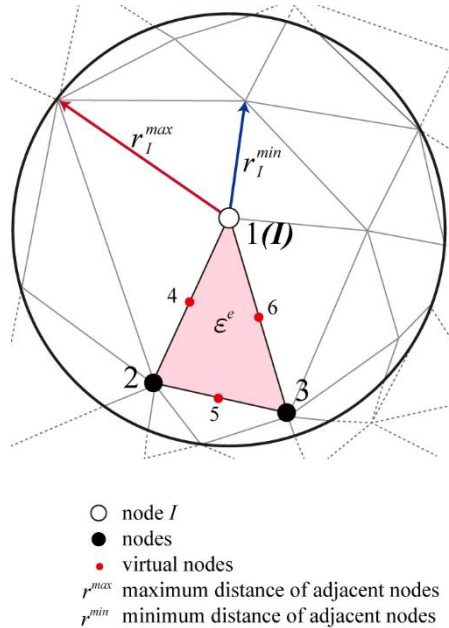


Figure 2.1. The local support I corresponding to node I of triangular element ε^e .

The additional virtual nodes (nodes 4, 5, and 6) are marked as red dots.

Next, the weight functions, $W_J(\mathbf{x})$, are defined for each corner nodes of triangular element region, ε^e , as following:

$$W_J(\mathbf{x}) = \begin{cases} 1 - 6s^2 + 8s^3 - 3s^4 & (0 \leq s < 1) \\ 0 & (\text{otherwise}) \end{cases} \quad (2.9)$$

with s given as

$$s = d_J(\mathbf{x}) / r_J^{\max} \quad (2.10)$$

where d_J denotes the distance between node J and a point \mathbf{x} inside the triangular element ε^e , and r_J^{\max} is the support radius of local support I . Here, three virtual nodes (nodes 4,5 and 6 in the Figure 2.1) are added to the triangular element ε^e as well as the original corner nodes (nodes 1, 2 and 3). These virtual nodes and the corner nodes are used temporarily for interpolating the approximated Shepard functions. The auxiliary Shepard functions, $\tilde{\phi}_J^I(\mathbf{x})$, are obtained by following relation.

$$\tilde{\phi}_J^I(\mathbf{x}) = \sum_{i=1}^6 \hat{h}_i(\mathbf{x}) \hat{\phi}_{ji}^I \quad (2.11)$$

where $\hat{h}_i(\mathbf{x})$ are the shape functions of classical 6-node triangular element each corresponding to original corner nodes and additional virtual nodes. The coefficients, $\hat{\phi}_{ji}^I$, are evaluated at six virtual and original nodal points defined previously. The details of the coefficients, $\hat{\phi}_{ji}^I$, are described in the Table 2.1.

Finally, the auxiliary Shepard function is updated by following relation, which is designed for minimizing the effect of severe mesh distortion.

$$\phi_J^I(\mathbf{x}) = \frac{\sqrt{r_I^{\min}}}{\sqrt{r_I^{\max}} + \sqrt{r_I^{\min}}} \tilde{\phi}_J^I + \frac{\sqrt{r_I^{\max}}}{\sqrt{r_I^{\max}} + \sqrt{r_I^{\min}}} \delta_{IJ} \quad (2.12)$$

Here, δ_{IJ} denotes the Kronecker delta symbol.

$\hat{\phi}_1^I(\mathbf{x}) = \sum_{i=1}^6 \hat{h}_i \hat{\phi}_{1i}^I$		$\hat{\phi}_2^I(\mathbf{x}) = \sum_{i=1}^6 \hat{h}_i \hat{\phi}_{2i}^I$		$\hat{\phi}_3^I(\mathbf{x}) = \sum_{i=1}^6 \hat{h}_i \hat{\phi}_{3i}^I$	
$\hat{\phi}_{11}^I$	1	$\hat{\phi}_{11}^I$	0	$\hat{\phi}_{11}^I$	0
$\hat{\phi}_{12}^I$	$\frac{W_1}{W_1 + W_2} \Big _{\mathbf{x}_2}$	$\hat{\phi}_{12}^I$	$\frac{W_2}{W_1 + W_2} \Big _{\mathbf{x}_2}$	$\hat{\phi}_{12}^I$	0
$\hat{\phi}_{13}^I$	$\frac{W_1}{W_1 + W_3} \Big _{\mathbf{x}_3}$	$\hat{\phi}_{13}^I$	0	$\hat{\phi}_{13}^I$	$\frac{W_3}{W_1 + W_3} \Big _{\mathbf{x}_3}$
$\hat{\phi}_{14}^I$	$\frac{W_1}{W_1 + W_2} \Big _{\mathbf{x}_4}$	$\hat{\phi}_{14}^I$	$\frac{W_2}{W_1 + W_2} \Big _{\mathbf{x}_4}$	$\hat{\phi}_{14}^I$	0
$\hat{\phi}_{15}^I$	$\frac{W_1}{W_1 + W_2 + W_3} \Big _{\mathbf{x}_5}$	$\hat{\phi}_{15}^I$	$\frac{W_2}{W_1 + W_2 + W_3} \Big _{\mathbf{x}_5}$	$\hat{\phi}_{15}^I$	$\frac{W_3}{W_1 + W_2 + W_3} \Big _{\mathbf{x}_5}$
$\hat{\phi}_{16}^I$	$\frac{W_1}{W_1 + W_3} \Big _{\mathbf{x}_6}$	$\hat{\phi}_{16}^I$	0	$\hat{\phi}_{16}^I$	$\frac{W_3}{W_1 + W_3} \Big _{\mathbf{x}_6}$

Table 2.1. Nodal values used in interpolating auxiliary Shepard functions on a triangular element.

The final form of the displacement field defined in Eq.(2.2) can be expressed as following.

$$u(\mathbf{x}) = \sum_{I=1}^3 h_I(\mathbf{x}) \sum_{J=1}^3 \phi_J^I(\mathbf{x}) \sum_n p_n \hat{a}_{Jn} \quad (2.13)$$

For simplification, we define a new function, $f_J(\mathbf{x})$, as

$$f_J(\mathbf{x}) = \sum_{I=1}^3 h_I(\mathbf{x}) \phi_J^I(\mathbf{x}) \quad (2.14)$$

which reduces the displacement field form of Eq.(2.13) to Eq.(2.15).

$$u(\mathbf{x}) = \sum_{J=1}^3 f_J(\mathbf{x}) \sum_n p_n \hat{a}_{Jn}(\mathbf{x}) \quad (2.15)$$

Using the newly defined function, $f_J(\mathbf{x})$, and the polynomial term p_n , we define a vector \mathbf{F}_J as

$$\mathbf{F}_J = f_J(\mathbf{x}) \times [1 \quad \bar{x} \quad \bar{y} \quad \bar{x}\bar{y} \quad \cdots] \quad (2.16)$$

The vector \mathbf{F}_J can be considered as a new shape function vector for node \mathbf{J} , derived by the overlapping element. The nodal unknown vectors corresponding to \mathbf{F}_J can be written as

$$\begin{aligned} \hat{\mathbf{a}}_J^u &= [\hat{a}_{J1}^u \quad \hat{a}_{Jx}^u \quad \hat{a}_{Jy}^u \quad \hat{a}_{Jxy}^u \quad \cdots] \\ \hat{\mathbf{a}}_J^v &= [\hat{a}_{J1}^v \quad \hat{a}_{Jx}^v \quad \hat{a}_{Jy}^v \quad \hat{a}_{Jxy}^v \quad \cdots] \end{aligned} \quad (2.17)$$

where the subscripts in, for example, \hat{a}_{Jx}^u , means that nodal unknown is related with node J and the enriched polynomial term x . Finally, we express the displacement field approximated by the overlapping element using the new shape function vector \mathbf{F} and nodal unknown vector $\hat{\mathbf{a}}^u$ for later use in construction of finite element matrices.

$$\begin{cases} u = \mathbf{F}\hat{\mathbf{a}}^u = [\mathbf{F}_1 \quad \mathbf{F}_2 \quad \mathbf{F}_3][\mathbf{a}_1^u \quad \mathbf{a}_2^u \quad \mathbf{a}_3^u]^T \\ v = \mathbf{F}\hat{\mathbf{a}}^v = [\mathbf{F}_1 \quad \mathbf{F}_2 \quad \mathbf{F}_3][\mathbf{a}_1^v \quad \mathbf{a}_2^v \quad \mathbf{a}_3^v]^T \end{cases} \quad (2.18)$$

The displacement expressed in the vector form comprised of the new shape function vector \mathbf{F} and nodal unknown vectors $\hat{\mathbf{a}}^u$ and $\hat{\mathbf{a}}^v$, we can perform differentiation directly on this new shape function vector \mathbf{F} to obtain strain-displacement matrix and to finally construct the overlapping element stiffness matrices.

2.3 Approximation of the displacement field in 3D domain

To expand our mixed overlapping element for three-dimensional problems, we use the same procedure for interpolating displacement field as we have proceeded in two-dimensional case (Section 2.2).

The displacement approximation consists of interpolation functions of conventional linear tetrahedral element, $h_I(\mathbf{x})$, and the local field function, $\psi_I(\mathbf{x})$, defined for a node I in a tetrahedral element region.

$$u(\mathbf{x}) = \sum_{I=1}^4 h_I(\mathbf{x}) \psi_I(\mathbf{x}) \quad (2.19)$$

We define the local field function, $\psi_I(\mathbf{x})$, composed of the interpolated Shepard functions, $\phi_J^I(\mathbf{x})$, and a series of nodal unknowns, $u_J(\mathbf{x})$.

$$\psi_I(\mathbf{x}) = \sum_{J=1}^4 \phi_J^I(\mathbf{x}) u_J(\mathbf{x}) \quad (2.20)$$

The interpolated Shepard function, $\phi_J^I(\mathbf{x})$, is calculated by using nodal weight functions which will be described later on. The series of nodal unknowns $u_J(\mathbf{x})$ are nodal variables enriched by a set of predetermined polynomial basis and are expressed as in the two-dimensional case of Eq.(2.4).

$$u_J(\mathbf{x}) = \sum_n p_n \hat{a}_{Jn} \quad (2.21)$$

Here, p_n is the polynomial term of n -th order three-dimensional polynomial basis which are given, for example, as

$$p_n \in \mathbf{p}^T = [1 \quad x \quad y \quad z \quad xy \quad yz \quad zx \quad x^2 \quad \dots]^T \quad (2.22)$$

Subsequently, \hat{a}_{Jn} is the nodal unknown variables of corresponding polynomial order n and node J . The series of nodal unknowns corresponding to the node J using linear and trilinear polynomial basis can be expressed as Eqs.(2.23 and 2.24).

$$u_J(\mathbf{x}) = \hat{a}_{J1} + \hat{a}_{J2}\bar{x} + \hat{a}_{J3}\bar{y} + \hat{a}_{J3}\bar{z} \quad (2.23)$$

$$u_J(\mathbf{x}) = \hat{a}_{J1} + \hat{a}_{J2}\bar{x} + \hat{a}_{J3}\bar{y} + \hat{a}_{J4}\bar{z} + \hat{a}_{J5}\bar{x}\bar{y} + \hat{a}_{J6}\bar{y}\bar{z} + \hat{a}_{J7}\bar{z}\bar{x} \quad (2.24)$$

Here, \bar{x} (or \bar{y} , \bar{z}) means the local coordinate attached to node J (coordinates measured from node J). This was intended for avoiding ill-conditioned matrices when some material points are located far away from the global origin.

Calculation of the interpolated Shepard function in 3D domain

In this section, we develop the concept of the interpolated Shepard function treated in the two-dimensional case (Section 2.2) to the three-dimensional case. As we had proceeded in the two-dimensional case, we define a spherical region centered at node I with the radius defined by the maximum distance between the node I and the adjacent nodes. We denote radius of the sphere as r_I^{\max} . The spherical region is called the local support I . The minimum distances between the node I and the adjacent nodes is denoted as r_I^{\max} for later use.

First, we define six additional virtual nodes located on the middle of each edge of a tetrahedral element ε^e as described in the Figure 2.2. The six virtual nodes located on each edge and four original nodes located on each corner of tetrahedron are used, temporarily, to calculate the approximated Shepard function, $\tilde{\phi}_J^I(\mathbf{x})$. The auxiliary Shepard function, $\hat{\phi}_J^I(\mathbf{x})$, are obtained by following relation.

$$\tilde{\phi}_J^I(\mathbf{x}) = \sum_{i=1}^{10} \hat{h}_i(\mathbf{x}) \hat{\phi}_{Ji}^I \quad (2.25)$$

where $\hat{h}_i(\mathbf{x})$ are the shape functions of classical 10-node tetrahedral element each corresponding to original corner nodes and additional virtual nodes. The coefficients, $\hat{\phi}_{ji}^l$, are evaluated at all virtual and original nodal points. We illustrate the detailed calculation of the coefficients, $\hat{\phi}_{ji}^l$, in the Table 2.2. We use the weight function, $W_j(\mathbf{x})$, same as the one defined in the two dimensional case Eq.(2.9).

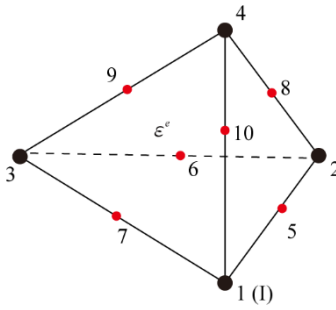


Figure 2.2. Additional nodes (marked as red) for interpolation of auxiliary Shepard functions on a tetrahedral overlapped region \mathcal{E}^e .

$\hat{\phi}'_1(\mathbf{x}) = \sum_{i=1}^{10} \hat{h}_i \hat{\phi}'_{1i}$		$\hat{\phi}'_2(\mathbf{x}) = \sum_{i=1}^{10} \hat{h}_i \hat{\phi}'_{2i}$		$\hat{\phi}'_3(\mathbf{x}) = \sum_{i=1}^{10} \hat{h}_i \hat{\phi}'_{3i}$		$\hat{\phi}'_4(\mathbf{x}) = \sum_{i=1}^{10} \hat{h}_i \hat{\phi}'_{4i}$	
$\hat{\phi}'_{11}$	1	$\hat{\phi}'_{21}$	0	$\hat{\phi}'_{31}$	0	$\hat{\phi}'_{41}$	0
$\hat{\phi}'_{12}$	$\frac{W_1}{W_1 + W_2} \Big _{\mathbf{x}_2}$	$\hat{\phi}'_{22}$	$\frac{W_2}{W_1 + W_2} \Big _{\mathbf{x}_2}$	$\hat{\phi}'_{32}$	0	$\hat{\phi}'_{42}$	0
$\hat{\phi}'_{13}$	$\frac{W_1}{W_1 + W_3} \Big _{\mathbf{x}_3}$	$\hat{\phi}'_{23}$	0	$\hat{\phi}'_{33}$	$\frac{W_3}{W_1 + W_3} \Big _{\mathbf{x}_3}$	$\hat{\phi}'_{43}$	0
$\hat{\phi}'_{14}$	$\frac{W_1}{W_1 + W_4} \Big _{\mathbf{x}_4}$	$\hat{\phi}'_{24}$	0	$\hat{\phi}'_{34}$	0	$\hat{\phi}'_{44}$	$\frac{W_4}{W_1 + W_4} \Big _{\mathbf{x}_4}$
$\hat{\phi}'_{15}$	$\frac{W_1}{W_1 + W_2} \Big _{\mathbf{x}_5}$	$\hat{\phi}'_{25}$	$\frac{W_2}{W_1 + W_2} \Big _{\mathbf{x}_5}$	$\hat{\phi}'_{35}$	0	$\hat{\phi}'_{45}$	0
$\hat{\phi}'_{16}$	$\frac{W_1}{W_1 + W_2 + W_3} \Big _{\mathbf{x}_6}$	$\hat{\phi}'_{26}$	$\frac{W_2}{W_1 + W_2 + W_3} \Big _{\mathbf{x}_6}$	$\hat{\phi}'_{36}$	$\frac{W_3}{W_1 + W_2 + W_3} \Big _{\mathbf{x}_6}$	$\hat{\phi}'_{46}$	0
$\hat{\phi}'_{17}$	$\frac{W_1}{W_1 + W_3} \Big _{\mathbf{x}_7}$	$\hat{\phi}'_{27}$	0	$\hat{\phi}'_{37}$	$\frac{W_3}{W_1 + W_3} \Big _{\mathbf{x}_7}$	$\hat{\phi}'_{47}$	0
$\hat{\phi}'_{18}$	$\frac{W_1}{W_1 + W_2 + W_4} \Big _{\mathbf{x}_8}$	$\hat{\phi}'_{28}$	$\frac{W_2}{W_1 + W_2 + W_4} \Big _{\mathbf{x}_8}$	$\hat{\phi}'_{38}$	0	$\hat{\phi}'_{48}$	$\frac{W_4}{W_1 + W_2 + W_4} \Big _{\mathbf{x}_8}$
$\hat{\phi}'_{19}$	$\frac{W_1}{W_1 + W_3 + W_4} \Big _{\mathbf{x}_9}$	$\hat{\phi}'_{29}$	0	$\hat{\phi}'_{39}$	$\frac{W_3}{W_1 + W_3 + W_4} \Big _{\mathbf{x}_9}$	$\hat{\phi}'_{49}$	$\frac{W_4}{W_1 + W_3 + W_4} \Big _{\mathbf{x}_9}$
$\hat{\phi}'_{110}$	$\frac{W_1}{W_1 + W_4} \Big _{\mathbf{x}_{10}}$	$\hat{\phi}'_{210}$	0	$\hat{\phi}'_{310}$	0	$\hat{\phi}'_{410}$	$\frac{W_4}{W_1 + W_4} \Big _{\mathbf{x}_{10}}$

Table 2.2. Nodal values used in interpolating auxiliary Shepard functions on a tetrahedral element.

Finally, we update the auxiliary Shepard function by following relation, which was designed for minimizing the effect of severe mesh distortion.

$$\phi_J^I(\mathbf{x}) = \frac{\sqrt{r_I^{\min}}}{\sqrt{r_I^{\max}} + \sqrt{r_I^{\min}}} \tilde{\phi}_J^I + \frac{\sqrt{r_I^{\max}}}{\sqrt{r_I^{\max}} + \sqrt{r_I^{\min}}} \delta_{IJ} \quad (2.26)$$

The final form of the displacement field defined in Eq.(2.19) can be expressed as following.

$$u(\mathbf{x}) = \sum_{I=1}^4 h_I(\mathbf{x}) \sum_{J=1}^4 \phi_J^I(\mathbf{x}) \sum_n p_n \hat{a}_{Jn} \quad (2.27)$$

To simplify the equation (2.27), we define a new function, $f_J(\mathbf{x})$, as

$$f_J(\mathbf{x}) = \sum_{I=1}^4 h_I(\mathbf{x}) \phi_J^I(\mathbf{x}) \quad (2.28)$$

which reduces the displacement field form of (2.27) to (2.29).

$$u(\mathbf{x}) = \sum_{J=1}^4 f_J(\mathbf{x}) \sum_n p_n \hat{a}_{Jn}(\mathbf{x}) \quad (2.29)$$

Using the newly defined function, $f_J(\mathbf{x})$, and the polynomial term p_n , we define a vector \mathbf{F}_J as

$$\mathbf{F}_J = f_J(\mathbf{x}) \times [1 \quad \bar{x} \quad \bar{y} \quad \bar{z} \quad \dots] \quad (2.30)$$

The vector \mathbf{F}_J can be considered as a new shape function vector for node J , derived by three-dimensional overlapping element. The nodal unknown vectors corresponding to \mathbf{F}_J can be written as

$$\begin{aligned}
\hat{\mathbf{a}}_J^u &= [\hat{a}_{J1}^u \quad \hat{a}_{Jx}^u \quad \hat{a}_{Jy}^u \quad \hat{a}_{Jz}^u \quad \cdots] \\
\hat{\mathbf{a}}_J^v &= [\hat{a}_{J1}^v \quad \hat{a}_{Jx}^v \quad \hat{a}_{Jy}^v \quad \hat{a}_{Jz}^v \quad \cdots] \\
\hat{\mathbf{a}}_J^w &= [\hat{a}_{J1}^w \quad \hat{a}_{Jx}^w \quad \hat{a}_{Jy}^w \quad \hat{a}_{Jz}^w \quad \cdots]
\end{aligned} \tag{2.31}$$

where the subscripts in, for example, \hat{a}_{Jx}^u , means that nodal unknown is related with node J and polynomial term x .

Finally, we express the displacement field approximated by the overlapping element using the new shape function vector \mathbf{F} and nodal unknown vectors, $\hat{\mathbf{a}}^u$, $\hat{\mathbf{a}}^v$, and $\hat{\mathbf{a}}^w$, for later use in construction of finite element matrices.

$$\begin{cases} u = \mathbf{F}\hat{\mathbf{a}}^u = [\mathbf{F}_1 \quad \mathbf{F}_2 \quad \mathbf{F}_3 \quad \mathbf{F}_4][\mathbf{a}_1^u \quad \mathbf{a}_2^u \quad \mathbf{a}_3^u \quad \mathbf{a}_4^u]^T \\ v = \mathbf{F}\hat{\mathbf{a}}^v = [\mathbf{F}_1 \quad \mathbf{F}_2 \quad \mathbf{F}_3 \quad \mathbf{F}_4][\mathbf{a}_1^v \quad \mathbf{a}_2^v \quad \mathbf{a}_3^v \quad \mathbf{a}_4^v]^T \\ w = \mathbf{F}\hat{\mathbf{a}}^w = [\mathbf{F}_1 \quad \mathbf{F}_2 \quad \mathbf{F}_3 \quad \mathbf{F}_4][\mathbf{a}_1^w \quad \mathbf{a}_2^w \quad \mathbf{a}_3^w \quad \mathbf{a}_4^w]^T \end{cases} \tag{2.32}$$

The displacement expressed in the vector form comprised of the new shape function vector \mathbf{F} and nodal unknown vectors $\hat{\mathbf{a}}^u$, $\hat{\mathbf{a}}^v$, and $\hat{\mathbf{a}}^w$, we can perform differentiation directly on this new shape function vector \mathbf{F} to obtain strain-displacement matrix and to finally construct the overlapping element stiffness matrices.

Chapter 3

Displacement-pressure mixed formulation of overlapping element

3.1 Introduction

In this chapter, we introduce the concept of displacement-pressure mixed formulation with the process of constructing finite element matrices involving the displacement field considered in the overlapping element. Also, we present the possible combinations of number of displacement variables and pressure variables for the mixed overlapping element which we expect to show stable solutions.

The pure displacement-based finite element formulation might lead to volumetric locking phenomena when solving incompressible materials ^{8, 38}. The solution might lead to severely deteriorated results regardless of the mesh refinement level if the displacement variable is used solely as the unknown variable. This volumetric locking phenomena occurs because the displacement variables are subject to a constraint such that the volumetric strain (divergence of the displacement) are very small (or zero) in nearly incompressible media while the pressure must be kept at the finite level of order of the boundary tractions. The displacement-pressure mixed finite element formulation can be a solution to this volumetric locking problem in incompressible analysis.

Although the displacement-pressure mixed formulation provides an effective treatment to the volumetric locking of incompressible problem, additional stability

issue might arise in mixed finite elements formed by mixed formulation. For this stability issue, the number of displacement unknown variables and the number of pressure unknown variables for each element should be carefully determined. If the pressure variables are used excessively compared to the number of the displacement variables, the element will behave similar to the pure displacement-based formulation showing volumetric locking problems. On the other hand, if the number of pressure variables are too low, the convergence rate of the solution can be too low. For this reason, conventional mixed finite elements are often confined to high-order elements to avoid that the ratio of the number of displacement variables and the number of pressure variables be too low. And this may result in increasing the computational cost.

On the other hand, the overlapping element can be mixed with the pressure variables still using the low-order triangles due to its enlarged displacement function spaces. For this reason, mixed overlapping element can achieve the better efficiency compared to the conventional mixed finite elements. Here, we introduce the process for the displacement-pressure mixed formulation of the overlapping element. Then, we present several kinds of mixed overlapping elements with the possible combinations of the number of displacement degrees of freedom and the number of pressure degrees of freedom.

3.2 Construction of matrices for the mixed overlapping element

In displacement-pressure mixed formulation, both the displacement and the pressure are involved as independent variables. Thus, the general weak form of governing equation for linear elasticity can be expressed in two separate equations.

$$2G \int_{\Omega} \varepsilon'_{ij}(\mathbf{u}_h) \varepsilon'_{ij}(\mathbf{v}_h) d\Omega - \int_{\Omega} p_h \varepsilon_V(\mathbf{v}_h) d\Omega = \int_{\Omega} \mathbf{f}^B \cdot \mathbf{v}_h d\Omega \quad (\forall \mathbf{v}_h \in V_h) \quad (3.1)$$

$$\int_{\Omega} \left(\frac{p_h}{\kappa} + \varepsilon_V(\mathbf{u}_h) \right) q_h d\Omega = 0 \quad (\forall q_h \in Q_h) \quad (3.2)$$

Here, V_h and Q_h are the space of finite element spaces where we seek for the displacement and pressure solution. The symbols \mathbf{u}_h and p_h denotes the finite element solutions of displacement and pressure respectively.

In the first equation Eq.(3.1), the strain energy is divided into the deviatoric strain energy part and the volumetric strain energy part in the first equation. The deviatoric strain energy part involves the deviatoric strain which is only related to the displacement unknown variables. The volumetric strain energy part involves the volumetric strain and the pressure which is related to both the displacement and pressure unknown variables. The second equation Eq.(3.2) constrains the relation between the volumetric strain and the pressure. The bulk modulus (κ), shear modulus (G), volumetric strain (ε_V), and deviatoric strain (ε'_{ij}) are given as

$$\kappa = \frac{E}{3(1-2\nu)} \quad (3.3)$$

$$G = \frac{E}{2(1+\nu)} \quad (3.4)$$

$$\varepsilon_V = \sum_{i=1}^3 \varepsilon_{ii} \quad (3.5)$$

$$\varepsilon'_{ij} = \varepsilon_{ij} = \frac{\varepsilon_V}{3} \delta_{ij} \quad (3.6)$$

where E is the Young's modulus, ν is the Poisson's ratio, ε_{ij} is the ij -th component of the strain, δ_{ij} is the Kronecker Delta symbol. By using the equations from Eq.(3.1) to Eq.(3.6), we can construct the mixed finite element matrices for solving incompressible analysis.

The governing equation of incompressible elasticity can be expressed in element-wise matrix form using the overlapping displacement field and the assumed pressure field. The resulting mixed overlapping element formulation typically has a linear algebraic system of the form

$$\begin{bmatrix} \mathbf{K}_{uu} & \mathbf{K}_{up} \\ \mathbf{K}_{pu} & -\frac{1}{\kappa} \mathbf{K}_{pp} \end{bmatrix} \begin{bmatrix} \hat{\mathbf{a}} \\ \hat{\mathbf{p}} \end{bmatrix} = \begin{bmatrix} \mathbf{R} \\ 0 \end{bmatrix} \quad (3.7)$$

where $\hat{\mathbf{a}}$ denotes the unknown displacement variable vector of the overlapping element, $\hat{\mathbf{p}}$ denotes the unknown pressure variable vector. The entries of the system of stiffness matrix are

$$\mathbf{K}_{pp} = \int_{\Omega} \mathbf{B}_D \mathbf{C}' \mathbf{B}_D dV \quad (3.8)$$

$$\mathbf{K}_{up} = \mathbf{K}_{pu}^T = -\int_{\Omega} \mathbf{B}_V^T \mathbf{H}_p dV \quad (3.9)$$

$$\mathbf{K}_{pp} = \int_{\Omega} \mathbf{H}_p^T \mathbf{H}_p dV \quad (3.10)$$

where \mathbf{B}_D denotes the deviatoric strain matrix, \mathbf{B}_V denotes the volumetric strain matrix, \mathbf{C}' denotes the stress-strain matrix which relates the deviatoric

stress and strain components, \mathbf{H}_p denotes the interpolation vector for the pressure field which will be introduced later in the **Section 3.3**. The load vectors are constructed as the classical way except for that it uses the new shape function vector, \mathbf{F} , calculated from the overlapping element.

$$\mathbf{R} = \int_S \begin{bmatrix} \mathbf{F} & 0 \\ 0 & \mathbf{F} \end{bmatrix}^T \begin{bmatrix} f_x \\ f_y \end{bmatrix} dS \quad \text{for 2D} \quad (3.11)$$

$$\mathbf{R} = \int_S \begin{bmatrix} \mathbf{F} & 0 & 0 \\ 0 & \mathbf{F} & 0 \\ 0 & 0 & \mathbf{F} \end{bmatrix}^T \begin{bmatrix} f_x \\ f_y \\ f_z \end{bmatrix} dS \quad \text{for 3D} \quad (3.12)$$

where \mathbf{F} denotes the new shape function vector for the displacement calculated from the overlapping element. The vectors, $[f_x \ f_y]^T$ and $[f_x \ f_y \ f_z]^T$, denote the external surface traction vectors.

3.2.1 Matrices for 2D incompressible plane strain analysis

The deviatoric strain matrix (\mathbf{B}_D) and the volumetric strain matrix (\mathbf{B}_V) for plane strain analysis can be built with differentiating the new shape functions (\mathbf{F}) obtained from the overlapping element. The deviatoric strain matrix, \mathbf{B}_D , is expressed as

$$\begin{aligned}
 \boldsymbol{\varepsilon}' &= \begin{bmatrix} \varepsilon'_{xx} & \varepsilon'_{yy} & \gamma'_{xy} & \varepsilon'_{zz} \end{bmatrix}^T \\
 &= \begin{bmatrix} \frac{2}{3} \frac{\partial u}{\partial x} & -\frac{1}{3} \frac{\partial u}{\partial x} & \frac{\partial u}{\partial y} & -\frac{1}{3} \frac{\partial u}{\partial x} \\ -\frac{1}{3} \frac{\partial v}{\partial y} & \frac{2}{3} \frac{\partial v}{\partial y} & \frac{\partial v}{\partial x} & -\frac{1}{3} \frac{\partial v}{\partial y} \end{bmatrix} \\
 &= \begin{bmatrix} \frac{2}{3} \frac{\partial \mathbf{F}^T}{\partial x} & -\frac{1}{3} \frac{\partial \mathbf{F}^T}{\partial x} & \frac{\partial \mathbf{F}^T}{\partial y} & -\frac{1}{3} \frac{\partial \mathbf{F}^T}{\partial x} \\ -\frac{1}{3} \frac{\partial \mathbf{F}^T}{\partial y} & \frac{2}{3} \frac{\partial \mathbf{F}^T}{\partial y} & \frac{\partial \mathbf{F}^T}{\partial x} & -\frac{1}{3} \frac{\partial \mathbf{F}^T}{\partial y} \end{bmatrix}^T \begin{bmatrix} \hat{\mathbf{a}}^u \\ \hat{\mathbf{a}}^v \end{bmatrix} \\
 &= \mathbf{B}_D \hat{\mathbf{a}}
 \end{aligned} \tag{3.13}$$

where $\boldsymbol{\varepsilon}'$ is the vector with its components of engineering strains, \mathbf{F} denotes the vector with its components of new shape functions developed in the overlapping element, and $\hat{\mathbf{a}}^u$ (or $\hat{\mathbf{a}}^v$) denotes the corresponding nodal unknown vector.

The volumetric strain matrix, \mathbf{B}_V , is expressed as

$$\begin{aligned}
 \boldsymbol{\varepsilon}_V &= \begin{bmatrix} \frac{\partial \mathbf{F}}{\partial x} & \frac{\partial \mathbf{F}}{\partial y} \end{bmatrix} \begin{bmatrix} \hat{\mathbf{a}}^u \\ \hat{\mathbf{a}}^v \end{bmatrix} \\
 &= \mathbf{B}_V \hat{\mathbf{a}}
 \end{aligned} \tag{3.14}$$

The stress-strain matrix for the deviatoric stress and strain components for the plane strain analysis is defined as

$$\mathbf{C}' = \begin{bmatrix} 2G & 0 & 0 & 0 \\ 0 & 2G & 0 & 0 \\ 0 & 0 & G & 0 \\ 0 & 0 & 0 & 2G \end{bmatrix} \quad (3.15)$$

where G is the shear modulus defined in Eq.(3.4).

The final stiffness matrix for the overlapping mixed element can be calculated by plugging in the vectors and matrices described in Eq.(3.13 - 3.15) into Eq.(3.7).

3.2.2 Matrices for 3D incompressible solid analysis

For three-dimensional analysis, the deviatoric strain matrix (\mathbf{B}_D) and the volumetric strain matrix (\mathbf{B}_V) can be built with differentiating the new shape functions (\mathbf{F}) obtained from the overlapping element as we had done in the previous section (**Section 3.2.1**).

The deviatoric strain matrix, \mathbf{B}_D , for three-dimensional analysis is expressed as

$$\begin{aligned}
 \boldsymbol{\varepsilon}' &= \left[\varepsilon'_{xx} \quad \varepsilon'_{yy} \quad \varepsilon'_{zz} \quad \gamma'_{xy} \quad \gamma'_{yz} \quad \gamma'_{zx} \right]^T \\
 &= \begin{bmatrix} \frac{2}{3} \frac{\partial u}{\partial x} & -\frac{1}{3} \frac{\partial u}{\partial x} & -\frac{1}{3} \frac{\partial u}{\partial x} & \frac{\partial u}{\partial y} & 0 & \frac{\partial u}{\partial z} \\ -\frac{1}{3} \frac{\partial u}{\partial y} & \frac{2}{3} \frac{\partial u}{\partial y} & -\frac{1}{3} \frac{\partial u}{\partial y} & \frac{\partial u}{\partial x} & \frac{\partial u}{\partial z} & 0 \\ -\frac{1}{3} \frac{\partial u}{\partial z} & -\frac{1}{3} \frac{\partial u}{\partial z} & \frac{2}{3} \frac{\partial u}{\partial z} & 0 & \frac{\partial u}{\partial y} & \frac{\partial u}{\partial x} \end{bmatrix}^T \\
 &= \begin{bmatrix} \frac{2}{3} \frac{\partial \mathbf{F}}{\partial x} & -\frac{1}{3} \frac{\partial \mathbf{F}}{\partial x} & -\frac{1}{3} \frac{\partial \mathbf{F}}{\partial x} & \frac{\partial \mathbf{F}}{\partial x} & 0 & \frac{\partial \mathbf{F}}{\partial x} \\ -\frac{1}{3} \frac{\partial \mathbf{F}}{\partial x} & \frac{2}{3} \frac{\partial \mathbf{F}}{\partial x} & -\frac{1}{3} \frac{\partial \mathbf{F}}{\partial x} & \frac{\partial \mathbf{F}}{\partial x} & \frac{\partial \mathbf{F}}{\partial x} & 0 \\ -\frac{1}{3} \frac{\partial \mathbf{F}}{\partial x} & -\frac{1}{3} \frac{\partial \mathbf{F}}{\partial x} & \frac{2}{3} \frac{\partial \mathbf{F}}{\partial x} & 0 & \frac{\partial \mathbf{F}}{\partial x} & \frac{\partial \mathbf{F}}{\partial x} \end{bmatrix}^T \begin{bmatrix} \hat{\mathbf{a}}^u \\ \hat{\mathbf{a}}^v \\ \hat{\mathbf{a}}^w \end{bmatrix} \\
 &= \mathbf{B}_D \hat{\mathbf{a}}
 \end{aligned} \tag{3.16}$$

where $\boldsymbol{\varepsilon}'$ is the vector with its components of engineering strains, \mathbf{F} denotes the vector with its components of new shape functions developed in the overlapping element, and $\hat{\mathbf{a}}^u$ (or $\hat{\mathbf{a}}^v$, $\hat{\mathbf{a}}^w$) denotes the corresponding nodal unknown vector.

The volumetric strain matrix, \mathbf{B}_V , is expressed as

$$\begin{aligned}\boldsymbol{\varepsilon}_v &= \begin{bmatrix} \frac{\partial \mathbf{F}}{\partial x} & \frac{\partial \mathbf{F}}{\partial y} & \frac{\partial \mathbf{F}}{\partial z} \end{bmatrix} \begin{bmatrix} \hat{\mathbf{a}}^u \\ \hat{\mathbf{a}}^v \\ \hat{\mathbf{a}}^w \end{bmatrix} \\ &= \mathbf{B}_v \hat{\mathbf{a}}\end{aligned}\tag{3.17}$$

The stress-strain matrix for the deviatoric stress and strain components for the three-dimensional solid analysis is defined as

$$\mathbf{C}' = \begin{bmatrix} 2G & 0 & 0 & 0 & 0 & 0 \\ 0 & 2G & 0 & 0 & 0 & 0 \\ 0 & 0 & 2G & 0 & 0 & 0 \\ 0 & 0 & 0 & G & 0 & 0 \\ 0 & 0 & 0 & 0 & G & 0 \\ 0 & 0 & 0 & 0 & 0 & G \end{bmatrix}\tag{3.18}$$

The final stiffness matrix for the overlapping mixed element can be calculated by plugging in the vectors and matrices described in Eqs.(3.16 – 18) into Eq.(3.7).

3.3 The approximation of the pressure field

The interpolation vector of the pressure depends on which vector space is used for the pressure approximation. For example, we can use the constant and linear polynomial basis to approximate the pressure. This constant and linear pressure approximation are conducted on each local element separately. The element-wise pressure approximation do not ensure the continuity of pressure between elements, but this discontinuous pressure approximation has the advantage in that the element pressure variables be statically condensed out at local element level prior to the element assemblage leading to the more efficient computation.

$$\text{discontinuous / constant :} \quad p = \mathbf{H}_p \mathbf{p} = [\hat{p}_1] [1] \quad (3.19)$$

$$\text{discontinuous / linear :} \quad p = \mathbf{H}_p \mathbf{p} = [1 \quad x \quad y]^T [\hat{p}_1 \quad \hat{p}_2 \quad \hat{p}_3] \quad (3.20)$$

Here, \mathbf{H}_p is the interpolation vector for pressure approximation, and \mathbf{p} is vector of unknown pressure variables.

On the other hand, we can also approximate the pressure using classical linear shape functions. Since the shape functions are attached to nodes, and has the compatibility property between the elements, the continuity of the approximated pressure is ensured at the expense of more computational loads compared to the discontinuous pressure approximation.

$$\text{continuous / linear :} \quad p = \mathbf{H}_p \mathbf{p} = [h_1 \quad h_2 \quad h_3]^T [\hat{p}_1 \quad \hat{p}_2 \quad \hat{p}_3] \quad (3.21)$$

There can be another option, which is to use the modified shape functions derived from the overlapping element in interpolating the pressure instead of using classical linear shape functions. However, our numerical experience suggest that we cannot expect further enhancement from using the modified shape functions derived from the overlapping element in interpolating the pressure instead of using

classical linear shape functions. The details of numerical tests are presented in the Appendix A1. For this reason, we choose to use classical linear shape functions.

We listed, for example, several kinds conventional mixed finite element in the Figure 3.1, whose stability are already analyzed by other authors. The elements labeled ‘Tri7/3’, ‘Tri6/3c’, ‘Quad9/3’, and ‘Quad9/4c’ are the conventional mixed finite elements which have been proven to be stable over periods of time. The element ‘Tri7/3’ is a triangular element using seven nodes to represent the displacement variables (three nodes located at each corner and edge, and one node located at the center). The displacement is approximated with quadratic space enriched with a cubic bubble function (P_2^+). The pressure is approximated in a discontinuous sense that each element uses three pressure variables with linear polynomial basis, (1, x , and y). The details of the element are analyzed in ⁵⁵.

The element ‘Tri6/3c’ and ‘Quad9/4c’ is also a well known stable element, also known as Taylor-Hood element of ($P_2 - P_1$) and ($Q_2 - Q_1$) type, respectively. A 6-node triangular element expanded by a quadratic space (P_2) is used for ‘Tri6/3c’ and a 9-node quadrilateral element expanded by a biquadratic space (Q_2) is used for ‘Quad9/4c’. Both element use continuous shape functions for the pressure approximation. The shape functions same as the ones used in classical linear triangular element (P_1) is used for ‘ $P_2 - P_1$ ’ element and the shape functions same as the ones used in classical bilinear quadrilateral element (Q_1) is used for ‘ $Q_2 - Q_1$ ’ element for approximating pressure field. These elements were first found by Taylor and Hood⁵⁶ in an experimental way, and the stability were analyzed by Bercovier and Pironneau ⁵⁷.

The ‘Quad9/3’ element, also denoted as ($Q_2 - Q_1$) element with discontinuous pressure field, is probably the most popular quadrilateral element showing a fair error convergence rate with a reasonable computational cost. The biquadratic space (Q_2) is used over 9-node quadrilateral element for the displacement field, and a bilinear space (Q_1) is used over the elementwise domain for the pressure field. The element is known to be stable, proved by Bercovier and Pironneau ⁵⁷.

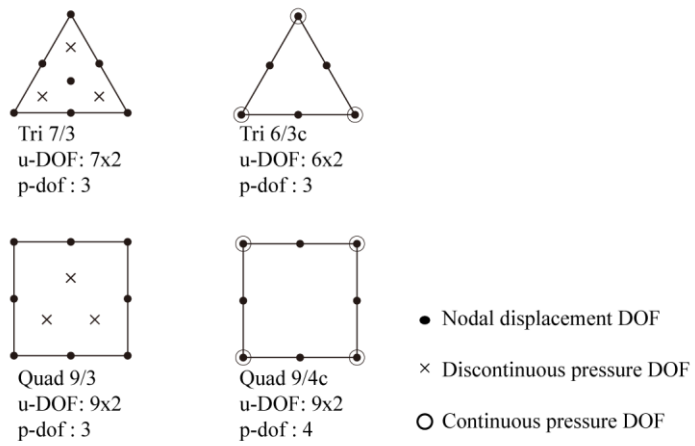


Figure 3.1. List of the conventional mixed finite elements.

In Figure 3.2 and 3.3, we present the possible combinations of displacement and pressure variables of mixed overlapping element. The notations used for the mixed overlapping elements shown in the Figure 3.2 and 3.3 are determined by following rules.

- i) 'OL' means the abbreviation for the overlapping element
- ii) The first number which follows after the letter 'OL' means the number of polynomial terms used for enriching the overlapping displacement. i.e. OL4/x element uses the overlapping displacement field enriched by 4 polynomial terms $(1, x, y, xy)$.
- iii) The last number which follows after the letter 'OLx/' means the number of polynomial terms used for approximating the pressure field. i.e. OLx/3 element approximate the pressure using 3 polynomial terms $(1, x, y)$.
- iv) The last number with the letter '3c' means that we use the continuous pressure approximation using the shape function of classical 3-node linear triangular element.

For three-dimensional overlapping element which is to be used in the practical example problem in Chapter 6, we use the combination of linear polynomial basis for the enriching the displacement field and a constant pressure field, which can be considered equivalent to the 'OL3/1' element in the two-dimensional case. We call it 'OL4/1' element for three-dimensional analysis, meaning that four polynomial terms $(1, x, y, z)$ are used in the enrichment of displacement field and one constant variable is used for the pressure field. We use the 'OL4/1' for three-dimensional analysis in application to protein dynamics problem treated in the Chapter 6.

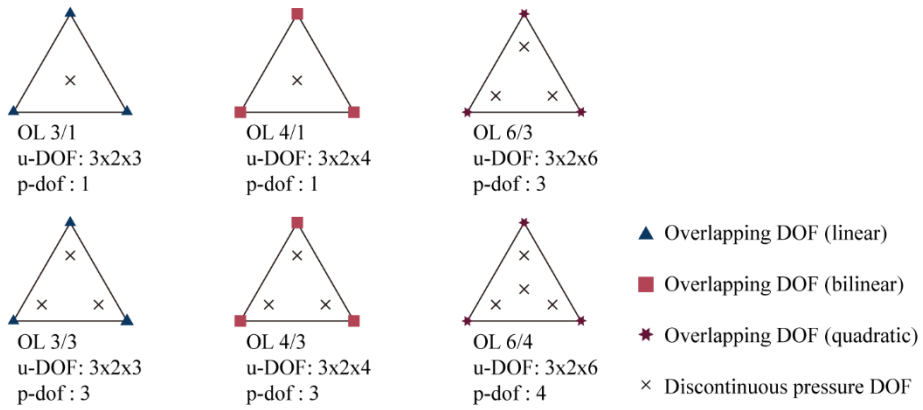


Figure 3.2. List of the combinations of mixed finite overlapping elements with the discontinuous pressure field.

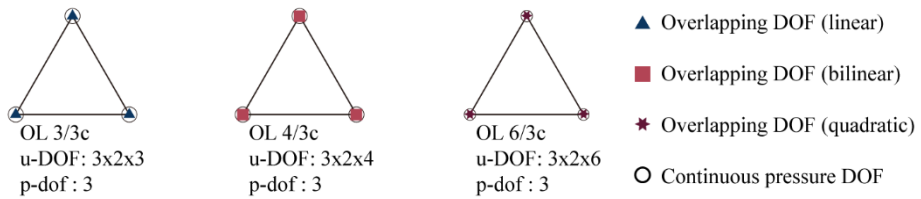


Figure 3.3. List of the combinations of mixed finite overlapping elements with the continuous pressure field.

Chapter 4

Stability of mixed overlapping element

4.1 Introduction

The error bound of the pure displacement-based formulation is known to be guaranteed once the fundamental conditions such as ellipticity and continuity are satisfied. This certified error bound ensures the consistent monotonic convergence and convergence rate according to the mesh refinement. Huang and Bathe also showed that the displacement-based overlapping element also shows monotonic convergence and consistent convergence rate, which was derived by using the concept of the Taylor series expansion on each local support domain I ³².

However, when it comes to the mixed formulation, whether the formulation is based on the traditional or the overlapping elements, the convergence is not always guaranteed depending on what interpolation is used for both the displacement and pressure approximation^{8, 38, 41}. An excessive number of pressure degree of freedoms is subject to cause volumetric locking problem. When the pressure is approximated at too high order, the constraint for the displacement variables, whose divergence must be small or zero, is too strong causing the element to act almost like the pure displacement-based formulation. On the other hand, if the pressure is approximated with the insufficient amount of pressure degree of freedoms, the rate of convergence of pressure as the mesh is refined is confined up to lower level, which affects the final solution to be poor. Therefore, the appropriate combinations of displacement and pressure degree of freedom should be carefully determined.

Therefore, another condition for the stable solution is required, the inf-sup condition, in addition to continuity and ellipticity conditions.

In this chapter, we introduce the procedure of the testing the stability of mixed overlapping element. We examine the stability of each presented mixed overlapping element by performing the numerical inf-sup test and investigating the pressure solution whether it shows a smooth and reasonable profile.

4.2 The inf-sup test

The inf-sup condition, so called the Brezzi-Babuška condition, provides an effective measure whether a certain mixed element is stable or not^{38, 46, 47}. If the finite element or overlapping element satisfies the basic continuity, ellipticity, and inf-sup condition, the element is assessed as a stable element, thus uniform accuracy is ensured. The general form of the inf-sup condition presented by Brezzi and Babuška is given as

$$\inf_{q_h \in P_h(\text{div} \mathbf{v}_h)} \sup_{\mathbf{v}_h \in V_h} \frac{\int_{\Omega} q_h \text{div} \mathbf{v}_h d\Omega}{\|\mathbf{v}_h\|_{V_h} \|q_h\|_{Q_h}} \geq \gamma_0 > 0 \quad (4.1)$$

where γ_0 is an inf-sup constant, a positive constant bounded above zero. Here, V_h is the space of finite element spaces where we seek for the displacement solution, and P_h means an L^2 -projector onto an auxiliary space Q_h where we usually seek for the pressure solution. The norm, $\|\cdot\|_{Q_h}$, means the L^2 -norm and the norm, $\|\cdot\|_{V_h}$, is measured by

$$\|\mathbf{v}\|_{V_h}^2 = \int_{\Omega} \sum_{i,j=1}^3 \left(\frac{\partial v_i}{\partial x_j} \right)^2 d\Omega \quad (4.2)$$

While the inf-sup condition Eq.(4.1) provides the effective assessment for the consistency and robustness of a mixed element, the evaluation of inf-sup constant itself is challengeable in testing various form of mixed element, sometimes requiring special techniques such as finding the Fortin's operator. To address this problem, we adopt the method of the numerical inf-sup testing which was previously presented by Chapelle and Bathe⁴⁸.

The numerical inf-sup test provides us to evaluate various problems, meshes, and elements quickly by evaluating the inf-sup value, γ_h , in the numerical sense. For a well-chosen set of meshes with a proper boundary condition, the numerical

inf-sup value is determined by following matrix equation ⁴⁸.

$$\begin{aligned}\gamma_h &= \inf_{q_h \in P_h(\text{div}\mathbf{v}_h)} \sup_{\mathbf{v}_h \in V_h} \frac{\int_{\Omega} q_h \text{div}\mathbf{v}_h d\Omega}{\|\mathbf{v}_h\|_V \|q_h\|_{Q_h}} \\ &= \inf_{\mathbf{w}_h} \sup_{\mathbf{v}_h} \frac{\mathbf{W}_h' \mathbf{G}_h \mathbf{V}_h}{\sqrt{\mathbf{V}_h' \mathbf{S}_h \mathbf{V}_h} \sqrt{\mathbf{W}_h' \mathbf{G}_h \mathbf{W}_h}}\end{aligned}\quad (4.3)$$

Here the norm matrix, \mathbf{S}_h , is defined by

$$\mathbf{V}_h' \mathbf{S}_h \mathbf{V}_h = \|\mathbf{v}_h\|_V^2 = \int_{\Omega} \left(\frac{\partial v_i}{\partial x_j} \right)^2 d\Omega \quad (4.4)$$

and \mathbf{G}_h is defined by

$$\mathbf{W}_h' \mathbf{G}_h \mathbf{V}_h = \int_{\Omega} P_h(\text{div}\mathbf{w}_h) \text{div}\mathbf{v}_h d\Omega \quad (4.5)$$

where P_h means an L^2 -projector onto an auxiliary space Q_h . The detailed procedure of obtaining \mathbf{G}_h and \mathbf{S}_h are described in the Section 4.3. Once the matrices \mathbf{G}_h and \mathbf{S}_h are evaluated, the inf-sup value can be obtained by solving following generalized eigenvalue problem.

$$\mathbf{G}_h \mathbf{V}_h = \lambda \mathbf{S}_h \mathbf{V}_h \quad (4.6)$$

If we let the first non-zero eigenvalue as λ_p , then the corresponding inf-sup value γ_h is simply $\sqrt{\lambda_p}$. The reader is recommend to refer to the work of Chapelle and Bathe (1993) ⁴⁸ for the detailed proof.

For the mixed elements using continuous pressure approximation, computing \mathbf{G}_h matrix is quite challengeable since the matrix \mathbf{G}_h is cannot be computed in a local element level and then assembled to a global matrix. Following alternate form can be used for the continuous pressure case.

$$\mathbf{G}'_h \mathbf{Q}_h = \lambda' \mathbf{K}_{pp} \mathbf{Q}_h \quad (4.7)$$

where \mathbf{G}'_h is simply

$$\mathbf{G}'_h = \mathbf{B}_h \mathbf{S}_h^{-1} \mathbf{B}_h^T \quad (4.8)$$

The generalized eigenvalue problem of Eq.(4.7) is equivalent to Eq.(4.6), so Eq.(4.7) can also be applied to the discontinuous pressure case.

Matrices for the numerical inf-sup test

The matrix \mathbf{S}_h is simply a matrix to represent the norm $\|\mathbf{v}_h\|_V$, and it can be computed by following equation.

$$\begin{aligned} \mathbf{V}'_h \mathbf{S}_h \mathbf{V}_h &= \mathbf{v}_h^T \begin{bmatrix} \tilde{\mathbf{S}}_h & 0 \\ 0 & \tilde{\mathbf{S}}_h \end{bmatrix} \mathbf{v}_h \\ \tilde{\mathbf{S}}_h &= \left[\left(\frac{\partial \mathbf{F}}{\partial x} \right)^T \frac{d\mathbf{F}}{dx} + \left(\frac{\partial \mathbf{F}}{\partial y} \right)^T \frac{d\mathbf{F}}{dy} \right] \end{aligned} \quad (4.9)$$

where \mathbf{F} denote the modified new shape functions calculated from the overlapping element.

The matrix \mathbf{G}_h for the discontinuous pressure case is obtained by following process. By the definition of \mathbf{G}_h matrix shown in Eq.(4.5), we need to express $\text{div} \mathbf{w}_h$ and $P_h(\text{div} \mathbf{w}_h)$ with \mathbf{w}_h being an arbitrary vector of displacement variables. The divergence is simply expressed as Eq.(4.10) where \mathbf{B}_V is the volumetric strain matrix provided in Eq.(3.14).

$$\text{div} \mathbf{w}_h = \mathbf{B}_V \hat{\mathbf{w}}_h = \left[\frac{d\mathbf{F}}{dx} \quad \frac{d\mathbf{F}}{dy} \right] \hat{\mathbf{w}}_h \quad (4.10)$$

By the definition of $P_h(\text{div}\mathbf{w}_h)$, an L^2 -projection of $\text{div}\mathbf{w}_h$ onto space Q_h , the relation between $P_h(\text{div}\mathbf{w}_h)$ and $\text{div}\mathbf{w}_h$ can be expressed in following form.

$$\int_{\Omega} [P_h(\text{div}\mathbf{w}_h) - \text{div}\mathbf{w}_h] q_h d\Omega = 0 \quad \text{for all } q_h \in Q_h \quad (4.11)$$

Here, $P_h(\text{div}\mathbf{w}_h)$ which is lying on a space Q_h can be expressed as

$$P_h(\text{div}\mathbf{w}_h) = [1 \quad x \quad y \quad \cdots] [\hat{p}_0 \quad \hat{p}_1 \quad \hat{p}_2 \quad \cdots]^T = \mathbf{q}_h^T \hat{\mathbf{p}}_h \quad (4.12)$$

here \hat{p}_i denote the independent variables for the pressure.

Since the Eq.(4.11) should be satisfied for all $q_h \in Q_h$, the relation Eq.(4.11) can be rewritten as Eq.(4.13) with vectors and matrix.

$$\int_{\Omega} \mathbf{q}_h (\mathbf{q}_h^T \hat{\mathbf{p}}_h) d\Omega - \int_{\Omega} \mathbf{q}_h (\mathbf{B}_V \hat{\mathbf{w}}_h) d\Omega = 0 \quad (4.13)$$

Solving the Eq.(4.13) for $\hat{\mathbf{p}}_h$ results in Eq(4.14).

$$\hat{\mathbf{p}}_h = \left(\int_{\Omega} \mathbf{q}_h \mathbf{q}_h^T d\Omega \right)^{-1} \left(\int_{\Omega} \mathbf{q}_h \mathbf{B}_V d\Omega \right) \hat{\mathbf{w}}_h \quad (4.14)$$

Subsequently, by plugging Eq.(4.14) into Eq.(4.12), we obtain the vector-matrix form of $P_h(\text{div}\mathbf{w}_h)$ as Eq.(4.15).

$$P_h(\text{div}\mathbf{w}_h) = \mathbf{q}_h^T \left(\int_{\Omega} \mathbf{q}_h \mathbf{q}_h^T d\Omega \right)^{-1} \left(\int_{\Omega} \mathbf{q}_h \mathbf{B}_V d\Omega \right) \hat{\mathbf{w}}_h = \mathbf{D}_h \hat{\mathbf{w}}_h \quad (4.15)$$

In Eq.(4.15), we introduced a new matrix \mathbf{D}_h for simplification.

Finally, using the newly introduced matrix, \mathbf{D}_h , the definition of \mathbf{G}_h in Eq.(4.5) can be rewritten as Eq.(4.16).

$$\begin{aligned}
\mathbf{W}_h^t \mathbf{G}_h \mathbf{V}_h &= \int_{\Omega} P_h(\operatorname{div} \mathbf{w}_h) \operatorname{div} \mathbf{v}_h d\Omega \\
&= \int_{\Omega} P_h(\operatorname{div} \mathbf{w}_h) P_h(\operatorname{div} \mathbf{v}_h) d\Omega \\
&= \hat{\mathbf{w}}_h \left(\int_{\Omega} \mathbf{D}_h^T \mathbf{D}_h d\Omega \right) \hat{\mathbf{v}}_h
\end{aligned} \tag{4.16}$$

Finally, the matrix, \mathbf{G}_h , can be evaluated as following.

$$\mathbf{G}_h = \int_{\Omega} \mathbf{D}_h^T \mathbf{D}_h d\Omega \tag{4.17}$$

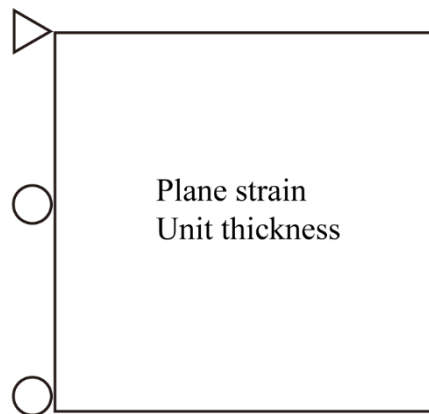
4.3 Numerical inf-sup test for a simple mechanical system

We show the inf-sup values and pressure distribution plots for the conventional mixed finite elements. Referring to the results of the conventional mixed finite element, the optimal combinations of mixed overlapping element are filtered out through the pass-fail results of the numerical inf-sup test, and then we investigate the pressure profiles to suggest the candidates for stable combinations.

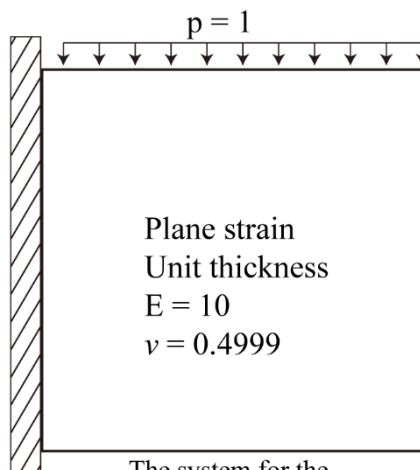
The mechanical systems used for the numerical inf-sup test and pressure distribution test are described in Figure 4.1. To perform the numerical inf-sup test, a cantilever plate of unit thickness with its upper left corner fixed in all directions and the left edge fixed in horizontal direction. To investigate the pressure distribution, we use the same geometry, but with the boundary conditions of left edge clamped. The clamped boundary condition is used to reveal more distinguishable pressure change along the solution domain. The upper side of the structure is enforced by a normal pressure p . The Young's modulus of 10 and the Poisson's ratio of 0.4999 are used. A plane strain condition is considered in both the numerical inf-sup test and the pressure distribution test.

The inf-sup values of conventional mixed finite element is shown in the Figure 4.2. The numerical inf-sup values, γ_h , are plotted versus $1/N$ where N is the square-root of total number of elements. As can be seen in the Figure 4.2, the numerical inf-sup values for presented conventional mixed finite element are bounded from below away from zero as the mesh refines. This is true for all three mesh patterns given, so can say that 'Tri7/3', 'Tri6/3c', 'Quad9/3', and 'Quad9/4c' have passed the numerical inf-sup test for given mesh patterns.

The pressure over the solution domain, plotted in the Figure 4.3, are also stable for most cases. The pressure distribution for 'Quad9/3' case shows some discontinuity across the elements. However, this can be considered as an intrinsic property that most discontinuous pressure approximation have. Since the severe instability (such as wiggles or checkerboard patterns with alternating plus-minus signs) is not observed, the element can be considered stable in the overall sense.



The system for the numerical inf-sup test



The system for the pressure distribution test

Figure 4.1. The mechanical systems used for the numerical inf-sup test and the pressure distribution test.

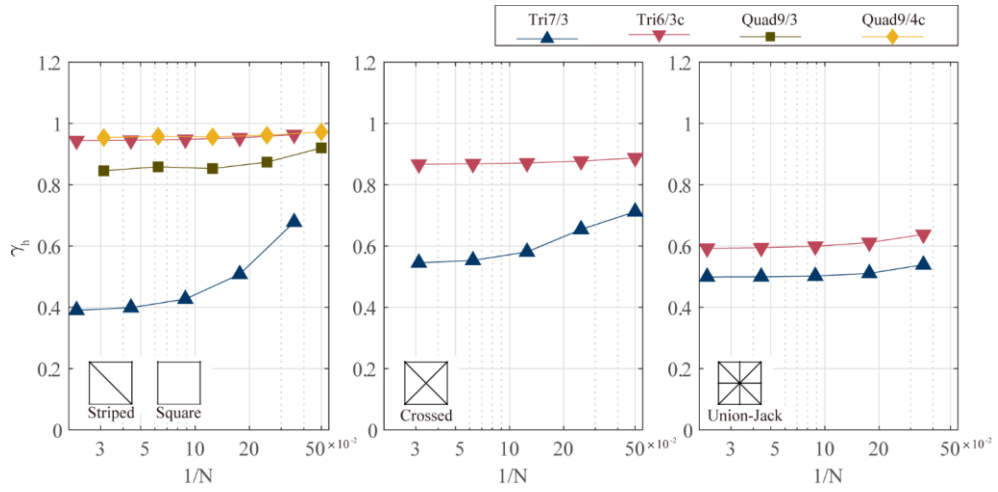


Figure 4.2. The numerical inf-sup values, γ_h , of the conventional stable mixed finite elements depending on the mesh refinement. The letter ‘N’ denotes the total number of elements.

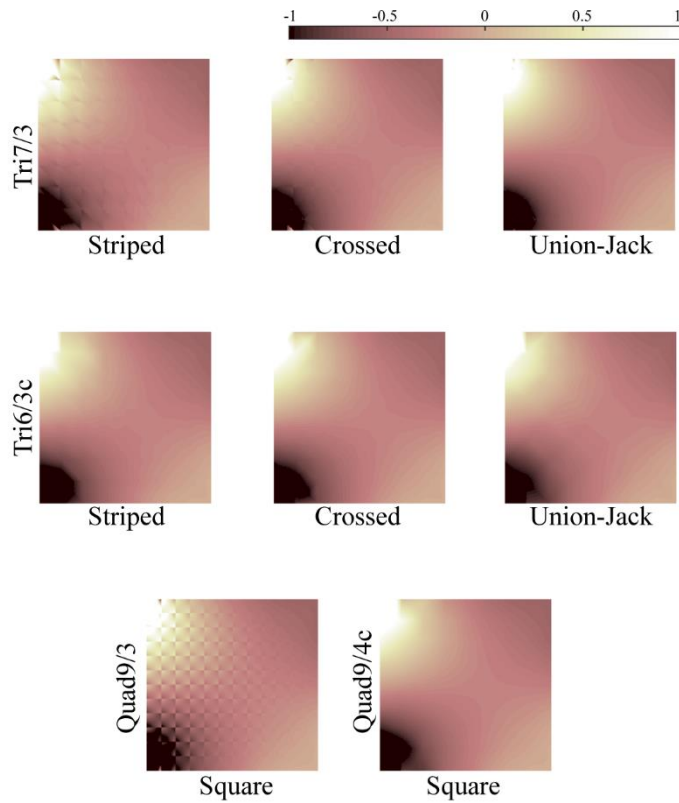


Figure 4.3. The pressure solutions of the conventional mixed element. Three different mesh patterns (striped, crossed, and Union-Jack pattern) are plotted for the triangular elements (Tri7/3 and Tri6/3c). A square pattern is used for the quadrilateral elements (Quad9/3, Quad9/4c).

Now we can refer to the stability test results of the conventional elements to evaluate our mixed overlapping element whether a certain combination is whether or not expected to be stable. The Figure 4.4 plots the inf-sup values of the mixed overlapping element with discontinuous pressure approximation. Firstly, the inf-sup values of ‘OL3/1’ and ‘OL4/1’ show boundedness. The values are converging to no lower than 0.8 for both striped and crossed patterned meshes, and 0.4 for Union-Jack mesh. The pressure distribution of ‘OL3/1’ and ‘OL4/1’ show the consistent results as the inf-sup test, where no severe instability occurs.

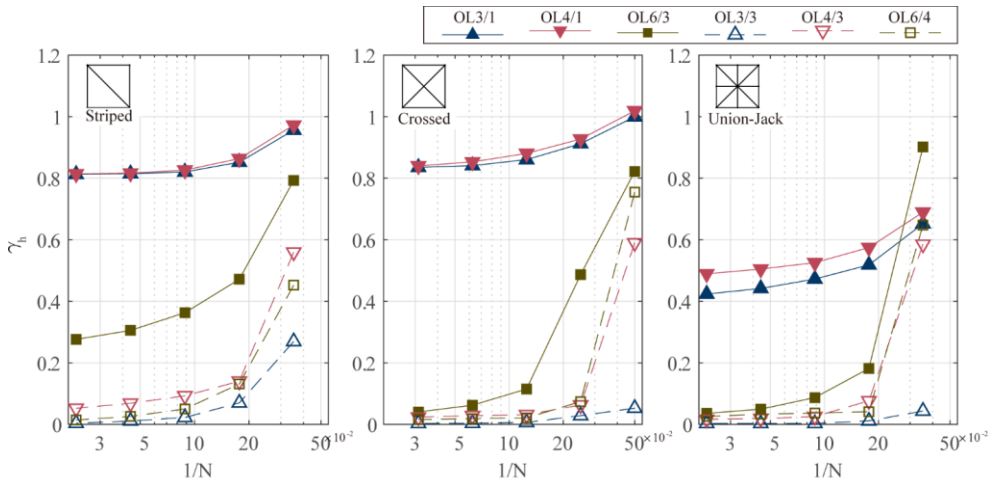


Figure 4.4. The numerical inf-sup values, γ_h , of the mixed overlapping element formulated with the discontinuous pressure approximation, depending on the mesh refinement. The letter ‘N’ denotes the total number of elements.

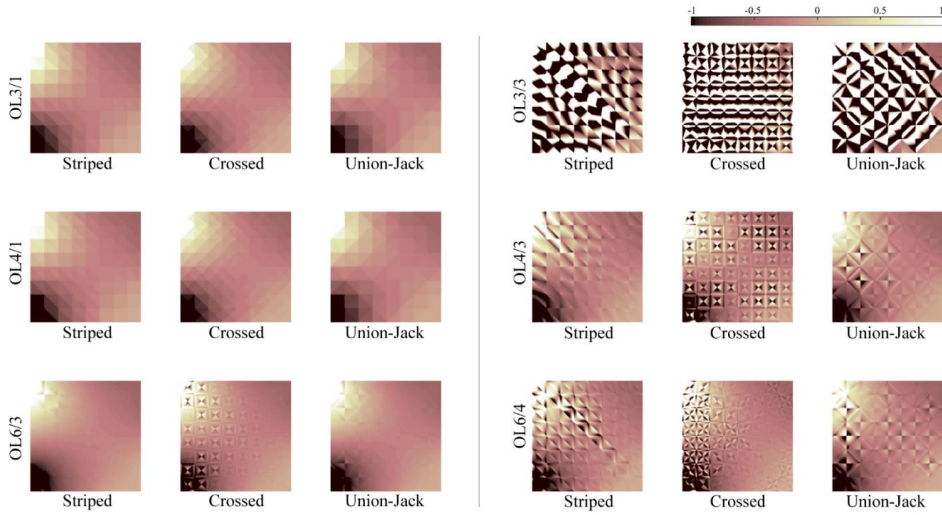


Figure 4.5. The pressure solutions of the mixed overlapping element with the discontinuous pressure approximation. Three different mesh patterns (striped, crossed, and Union-Jack pattern) are tested for each combination of mixed overlapping element.

The inf-sup values of ‘OL3/3’, ‘OL4/3’, and ‘OL6/4’ are clearly converging to zero as the mesh refines, which means that the mentioned elements are exposed to the risk of solution instability. As expected, those elements, regardless of mesh patterns, show severely wiggled distribution across the solution domain (Figure 4.5), which can lead to deteriorated solutions.

The ‘OL6/3’ case shows a quite interesting behavior. When a striped pattern is used, the inf-sup values of ‘OL6/3’ element seems to be bounded from below, which behaves similar to the stable ‘Tri7/3’ case. However, the inf-sup values converge to zero when the crossed and the Union-Jack patterns are used. From this fact, we can postulate that the element a strong dependence on what mesh pattern are used. In agreement with the insight from the inf-sup test, the mesh dependency of stability can be observed in the pressure distribution plotted in Figure 4.5. The pressure is smooth across the body in striped pattern case, whereas the pressure is distorted in the crossed and the Union-Jack cases. So, we can conclude that

‘OL6/3’ is inadequate for practical use.

Moving our focus onto the case of continuous pressure approximation case, the inf-sup values of ‘OL3/3c’, ‘OL4/3c’, and ‘OL6/3c’ show a clear boundedness for all the three mesh patterns (Figure 4.6). We can tell that the mixed overlapping element with the continuous pressure approximation pass the inf-sup condition and the stability is ensured. The same conclusion can be derived by investigating the pressure plots shown in the Figure 4.7, which show perfectly smooth distribution across the elements.

In summary, we filter out the stable mixed overlapping elements by performing the numerical inf-sup test and the pressure distribution test. The candidates for elements that can be used in a general problem are ‘OL3/1’, ‘OL4/1’, ‘OL3/3c’, ‘OL4/3c’, and ‘OL6/3c’ which are turn out to be stable, whereas ‘OL3/3’, ‘OL4/3’, and ‘OL6/3’ are not suitable for general use.

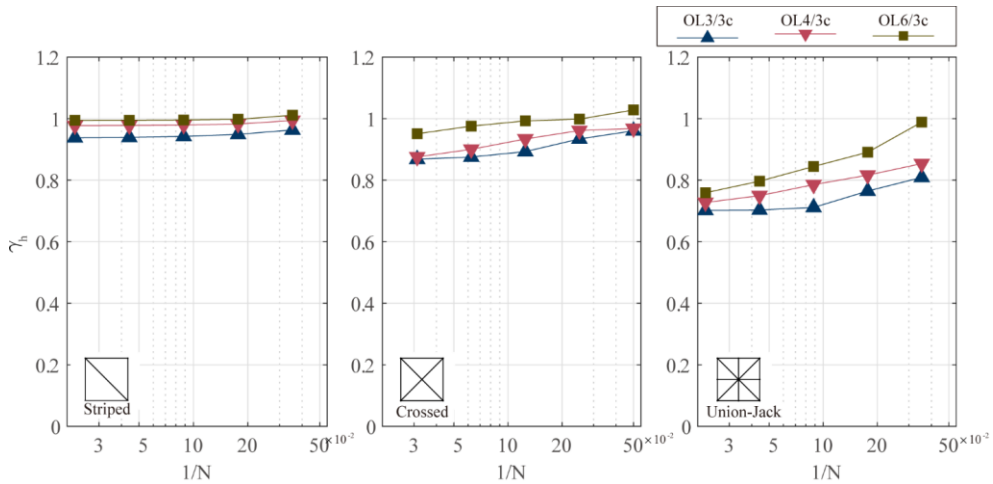


Figure 4.6. The numerical inf-sup values, γ_h , of the mixed overlapping element formulated with the continuous pressure approximation versus the mesh refinement.

The letter ‘N’ denotes the total number of elements

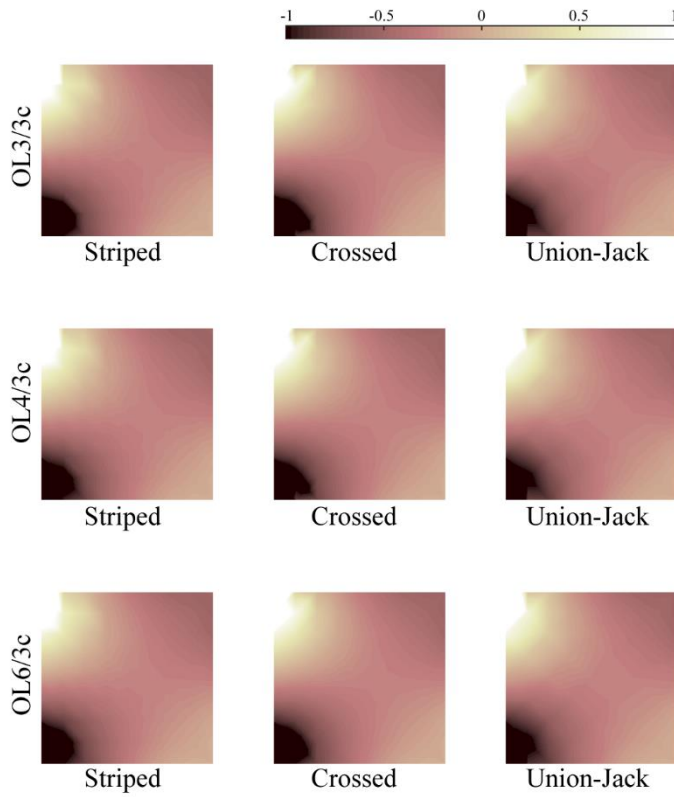


Figure 4.7. The pressure solutions of the mixed overlapping element with the continuous pressure approximation. Three different mesh patterns (striped, crossed, and Union-Jack pattern) are tested for each combination of mixed overlapping element.

4.4 Conclusion

The inf-sup test is the most general way to judge the stability of traditional mixed finite elements. We followed the procedure of inf-sup test to judge the stability of the proposed mixed overlapping elements.

We have performed the stability test for several mixed finite element presented in this study. The tested elements, with different combinations of displacement and pressure variables, were ‘OL3/1’, ‘OL4/1’, ‘OL6/3’, ‘OL3/3’, ‘OL4/3’, ‘OL6/4’, ‘OL3/3c’, ‘OL4/3c’, and ‘OL6/3c’ elements.

To examine the stability of mixed overlapping elements, first we performed a numerical inf-sup test, an efficient way of checking the stability of mixed finite element. Results of the inf-sup test showed that the mixed overlapping elements of ‘OL3/1’ are ‘OL4/1’ inf-sup stable among the mixed overlapping elements with discontinuous pressure approximation. The mixed overlapping element, ‘OL6/3’, seemed to be inf-sup stable when a striped patterned mesh is used, but the stability is not confirmed when a crossed or Union-Jack patterned mesh is used. All the mixed overlapping elements using continuous pressure field, ‘OL3/3c’, ‘OL4/3c’, and ‘OL6/3c’, passed the inf-sup test which we can conclude those elements are stable.

We performed an additional test by investigating smoothness of the pressure distribution of the solution of simple example problem. We obtained the results in consistency with the results of inf-sup test. The inf-sup stable elements, ‘OL3/1’, ‘OL4/1’, ‘OL3/3c’, ‘OL4/3c’, and ‘OL6/3c’ showed relatively smooth pressure profile over the domain, whereas the other elements show severe wiggled pattern in pressure distribution. The mesh dependency of ‘OL6/3’ element is also well captured in pressure distribution, same situation as in the inf-sup test. The pressure distribution of the element, ‘OL6/3’, seemed smooth enough when striped patterned mesh is used, but the pressure distribution is deteriorated when a crossed or Union-Jack patterned mesh is used.

Chapter 5

Numerical examples in 2D domain

5.1 Introduction

In this chapter, we present four numerical example problems in two-dimensional domain. We solve the example problems by using the stable mixed overlapping elements, which had already been filtered out in the Chapter 4 by performing some stability tests. The stable mixed overlapping elements chosen are ‘OL3/1’, ‘OL4/1’, ‘OL3/3c’, ‘OL4/3c’, and ‘OL6/3c’ elements. Apart from the stability point of view, in this chapter, we present some numerical examples to evaluate the accuracy and efficiency of mixed overlapping element in comparison with the conventional mixed finite elements.

First, we present and compare the results for the simple cantilever plate problem under normal pressure loading. Then we add harsher condition by applying shear loadings at the free end of the Cook’s membrane problem. Subsequently, we examine the bending behavior of a thick circular beam in which the classical triangular element has its weakness in expressing such bending behavior. Finally, we extend this bending problem to a very thin circular beam structure to examine the behavior of mixed overlapping elements in such the extreme case. By investigating these numerical problems, we expect to provide insights into which choice of element is optimal in a practical application. Through all the numerical examples, we consider a plane strain configuration with unit thickness.

5.2 Cantilever plate

In a first example, we investigated a cantilever plate problem to evaluate the efficiency of our mixed finite element, where the geometrical and material characteristics are given in the Figure 5.1. Three mesh models with different mesh refinement level are used to see the error convergence as described in Figure 5.1. The external pressure is applied uniformly normal to the top surface of clamped body.

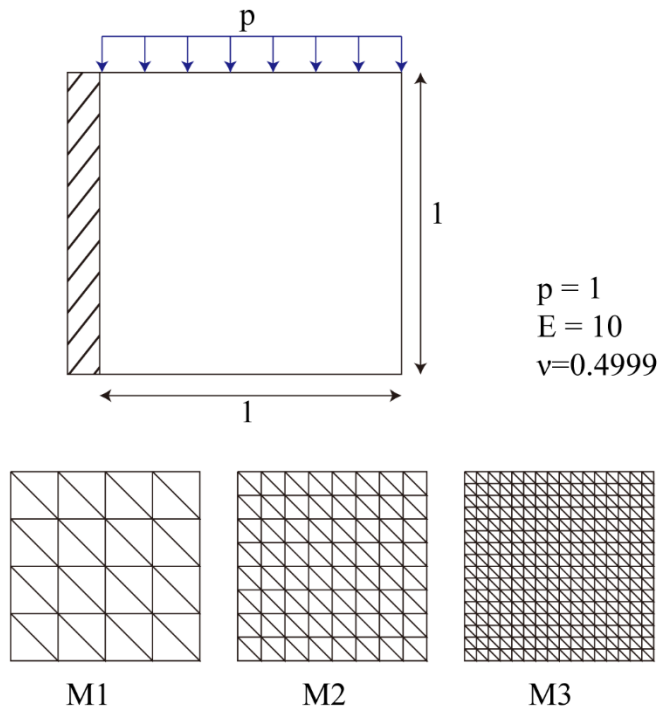


Figure 5.1. Description of the cantilever plate problem. The cantilever plate is under the normal pressure on the upper side with clamped boundary on the left side.

A set of meshes used in the numerical test is also plotted below the problem description.

We tested using the stable elements chosen in the previous section, which are ‘OL3/1’, ‘OL4/1’, ‘OL3/3c’, ‘OL4/3c’, and ‘OL6/3c’. The solution of the mixed overlapping elements and the conventional mixed finite elements converges in a similar convergence rate (Figure 5.2A and B).

The accuracy of ‘OL3/1’ shows more accurate results than ‘OL4/1’ for all mesh refinement levels, see Figure 5.2B. This implies that the linear enrichment of displacement field makes a better pair with the constant pressure assumption than the bilinearly enriched displacement field. A pressure assumed with a single variable seems not sufficient for ‘OL4/1’ element, degrading the solution accuracy of ‘OL4/1’ element. Comparing with the conventional elements, the ‘OL3/1’ element showed better performance than the ‘Tri7/3’ and ‘Tri6/3c’ elements, but slightly poorer than the quadrilateral elements (‘Quad9/3’ and ‘Quad 9/4c’).

In the Figure 5.2C and D, we plotted the percent error of tested elements depending on the number of displacement degree of freedoms implying the size of the problem. We can investigate the efficiency of the tested elements. The results are also listed in the Table 5.1 for more detailed numbers. The ‘OL3/1’ can achieve a percent error within 2 percent with 150 degree of freedoms, whereas the ‘Tri7/3’ and ‘Tri6/3c’ elements show 2.1 percent and 3.47 percent error with 226 and 162 degree of freedoms, same mesh. The ‘OL3/1’ achieves better accuracy with lower degree of freedoms. This trend is consistent for more refined mesh. The ‘OL3/1’ element shows 0.28 percent error with 1,734 degree of freedoms, whereas the ‘Tri7/3’ and ‘Tri6/3c’ element have 0.41 and 0.63 percent error with 3,202 and 2,178 degree of freedoms. However, the ‘OL3/1’ element is not as accurate or efficient as the quadrilateral elements. From this result, we can summarize that if we need to solve problems of complex geometry using the triangular elements where the quadrilateral meshing is restricted, the ‘OL3/1’ element might be a fair choice.

The mixed overlapping elements using the continuous pressure field, such as ‘OL4/3c’ and ‘OL6/3c’ showed the accuracy level similar to the quadrilateral elements. However, it is hard to tell that ‘OL4/3c’ and ‘OL6/3c’ have more

distinguishable efficiency than the quadrilateral elements, but have similar level of efficiency. Referring to the Figure **5.2C** and **D**, and the Table **5.1**, the number of degree of freedoms incorporated into ‘OL4/3c’ and ‘OL6/3c’ are similar to the quadrilateral elements to achieve certain accuracy order. Let us compare the computational efficiency of ‘OL4/3c’ with ‘Quad9/3’ element, which is the most accurate one confined to current example problem. The ‘OL4/3c’ requires 200 to 648 degree of freedoms to achieve the percent error between 0.26 to 0.56, while ‘Quad9/3’ requires 162 to 578 degree of freedoms to achieve the percent error between 0.21 to 0.44. The quadrilateral element ‘Quad9/3’ is slightly more efficient than ‘OL4/3c’. Likewise, ‘OL6/3c’ requires 300 to 972 degree of freedoms to achieve 0.15 and 0.36 percent error, which are slightly poorer than the ‘Quad9/3’ element. Still, having that the ‘OL4/3c’ and ‘OL6/3c’ are the most accurate among the triangular elements, those can provide nice options to achieve high accuracy versus computational loads. Lastly, the performance of ‘OL3/3c’ is not impressive showing the error level similar to ‘OL4/1’ element already mentioned above. It will be better choice to use ‘OL3/1’ element providing more accurate result. Also, ‘OL3/1’ has more benefit than ‘OL3/3c’ in the aspect of computational efficiency, because ‘OL3/1’ uses a single variable for pressure approximation. This single variable pressure approximation, in comparison with the continuous pressure approximation, provides us the diagonal stiffness matrix related to the pressure variables (\mathbf{K}_{pp} in Eq.(3.7)), which results in more efficient sparsity of overall stiffness matrix during the solution process.

Additional test data are available in Appendix **A2** and **A3**, which reinforce the effectiveness of mixed overlapping elements. In Appendix **A2**, we present the results for the same cantilever plate problem, but for the case when the material discontinuity are present inside the domain. In Appendix **A3**, we present the additional post processing results such as pressure profiles and xx-stress profiles.

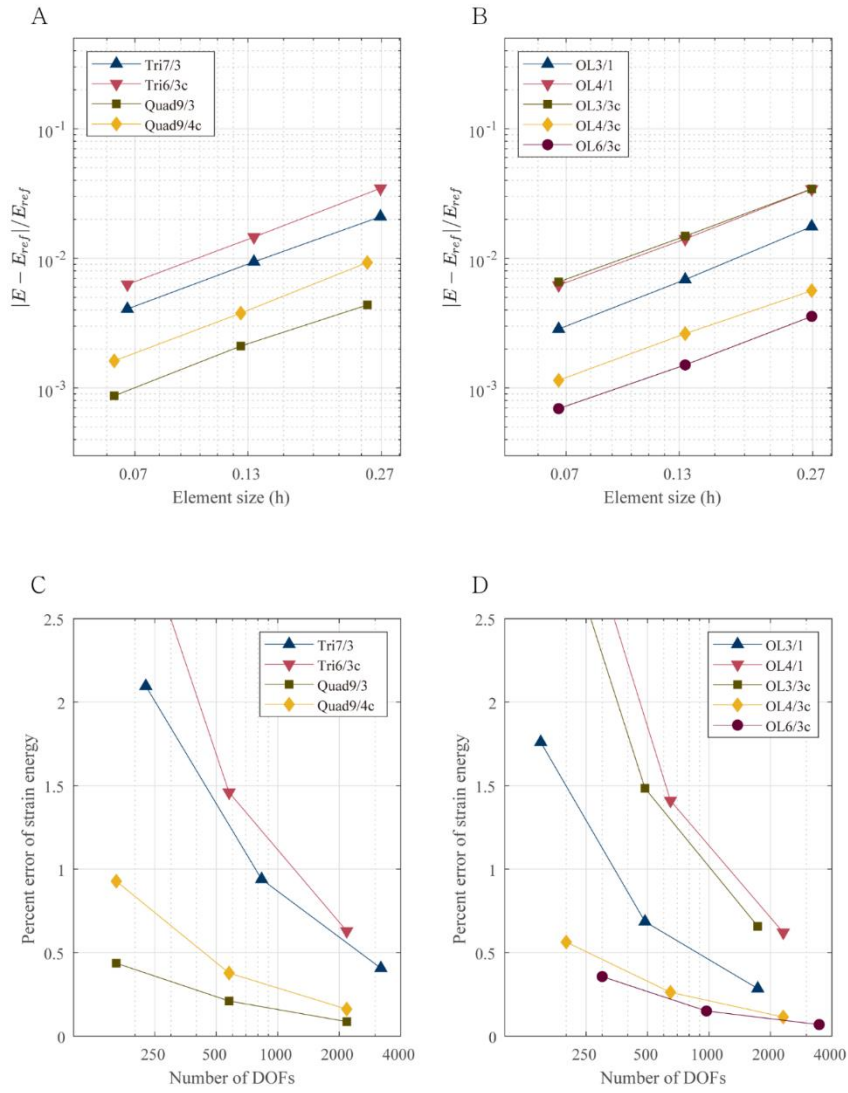


Figure 5.2. The strain energy error of cantilever plate problem. The convergence curve of (A) the conventional mixed finite elements and (B) the mixed overlapping elements in log scale. The percent error in strain energy of (C) the conventional mixed finite elements and (D) the mixed overlapping elements versus total number of the displacement degree of freedoms.

	Percent error [%]			Number of displacement degree of freedoms		
	M1	M2	M3	M1	M2	M3
Tri7/3	-2.10	-0.94	-0.41	226	834	3,202
Tri6/3c	-3.47	-1.46	-0.63	162	578	2,178
Quad9/3	-0.44	-0.21	-0.09	162	578	2,178
Quad9/4c	-0.93	-0.38	-0.16	162	578	2,178
OL3/1	1.76	0.69	0.28	150	486	1,734
OL4/1	3.42	1.41	0.62	200	648	2,312
OL3/3c	-3.44	-1.48	-0.66	150	486	1,734
OL4/3c	-0.56	-0.26	-0.11	200	648	2,312
OL6/3c	0.36	0.15	0.07	300	972	3,468

Table 5.1. The percent error of the cantilever plate problem compared with the number of displacement degree of freedoms.

5.3 Cook's membrane

For the second example, we analyzed a Cook's membrane benchmark test⁵⁸. The details of the geometrical and the material characteristics are described in the Figure 5.3. A uniformly distributed shear load is applied at the free end of the trapezoidal plate with its left boundary clamped on the wall. Overall situation is similar to the previous cantilever plate case, but the difference is that we expect more shear strain involved induced by the external shear loading.

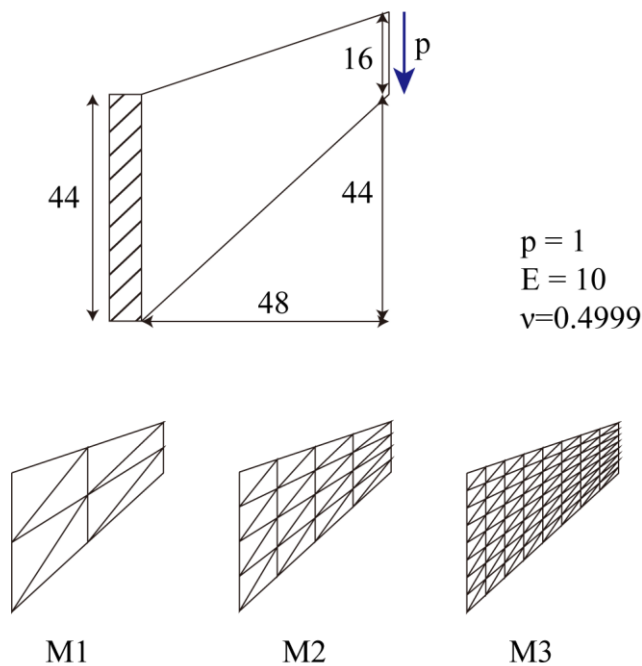


Figure 5.3. Description of the Cook's membrane problem. The Cook's membrane is under the tangential traction on the right side with clamped boundary on the left side. A set of meshes used in the numerical test is also plotted below the problem description.

In the accuracy of ‘OL3/1’ element shows more accurate result compared to ‘OL4/1’ element as shown if the convergence plot in the Figure 5.4B. We can develop similar logic to the previous cantilever plate example that using linear enrichment for the overlapping displacement field works better than the bilinear enrichment when a single variable is used for the pressure. In comparison with the conventional elements, the ‘OL3/1’ element is more accurate than the conventional triangular element, ‘Tri7/3’ and ‘Tri6/3c’. The ‘OL3/1’ element has 3.21 percent error in the coarsest mesh, whereas ‘Tri7/3’ and ‘Tri6/3c’ elements show 14.90 and 15.54 percent errors the Table 5.2. Having that the number of degree of freedoms involved in ‘OL3/1’ elements are similar to those traditional triangular elements, we can address that ‘OL3/1’ is more efficient than those traditional triangular elements (Table 5.2). Actually, ‘OL3/1’ element is as accurate and efficient as the traditional quadrilateral element such as ‘Quad9/3’ and ‘Quad9/4c’ element. Although the accuracy might be slightly poorer than traditional quadrilateral element in the coarsest mesh, we can reach the accuracy of those quadrilateral element as the mesh is refined (Table 5.2). The ‘OL3/1’ element requires 150 degree of freedoms to achieve the accuracy below one percent, while the quadrilateral elements require 162 degree of freedoms to reach the accuracy below one percent. It is noticeable that the error convergence of ‘OL3/1’ element is faster than ‘OL4/3c’ element. However, we hesitate to claim that the ‘OL3/1’ element is superior to the ‘OL4/3c’ element since the performance of those elements highly depend on the problems considered.

The ‘OL6/3c’ element, as expected, was the most accurate element, which show more accurate solution than any other elements including the conventional elements. The error of ‘OL6/3c’ were kept under one percent in all mesh set tested. In the aspect of efficiency, we can also argue that ‘OL6/3c’ is as efficient as other conventional quadrilateral elements. The ‘OL6/3c’ requires 108 degree of freedoms to achieve 0.99 percent error, while the ‘Quad9/4c’ element requires 162 degree of freedoms to reach 0.82 percent error. According the investigation, the mixed overlapping elements with the choice of ‘OL3/1’, ‘OL4/3c’, and ‘OL6/3c’ may

provide the competitive efficiency compared to the traditional finite elements.

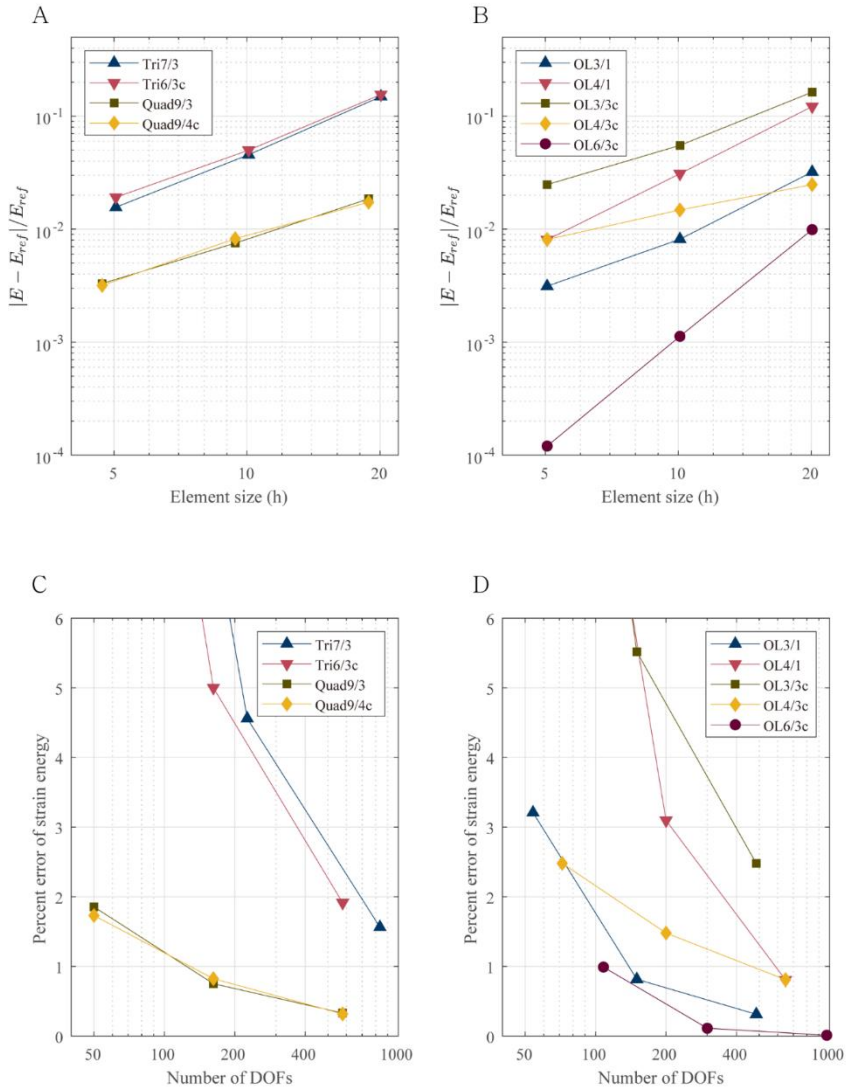


Figure 5.4. The strain energy error of Cook's membrane problem. The convergence curve of (A) the conventional mixed finite elements and (B) the mixed overlapping elements in log scale. The percent error of strain energy of (C) the conventional mixed finite elements and (D) the mixed overlapping elements versus total number of the displacement degree of freedoms.

	Percent error [%]			Number of displacement degree of freedoms		
	M1	M2	M3	M1	M2	M3
Tri7/3	-14.90	-4.56	-1.56	66	226	834
Tri6/3c	-15.54	-5.00	-1.91	50	162	578
Quad9/3	-1.85	-0.75	-0.33	50	162	578
Quad9/4c	-1.73	-0.82	-0.32	50	162	578
OL3/1	3.21	0.81	-0.31	54	150	486
OL4/1	12.18	3.10	0.81	72	200	648
OL3/3c	-16.33	-5.51	-2.48	54	150	486
OL4/3c	-2.48	-1.48	-0.81	72	200	648
OL6/3c	0.99	0.11	-0.01	108	300	972

Table 5.2. The percent error of the Cook's membrane problem compared with the number of displacement degree of freedoms.

5.4 Thick circular beam

The triangular element is known to have its weakness in expressing the bending of slender bodies compared to the quadrilateral elements, not to mention the beam elements devised for this special case. The displacement field approximated in the triangular element is frequently not sufficient to express the large shear strain or stress occurring during the bending process ⁸. In this example problem, we investigated a thick circular beam problem to examine the performance of the mixed overlapping elements when a severe bending is involved to a slender structure. We investigate the performance of the mixed overlapping element how well those elements capture the bending of slender bodies. The geometrical and material characteristics are described in the Figure 5.5. A set of tested meshes are also given in the Figure 5.5. A uniformly distributed shear load is applied at one free end of the structure while the other end clamped on the floor.

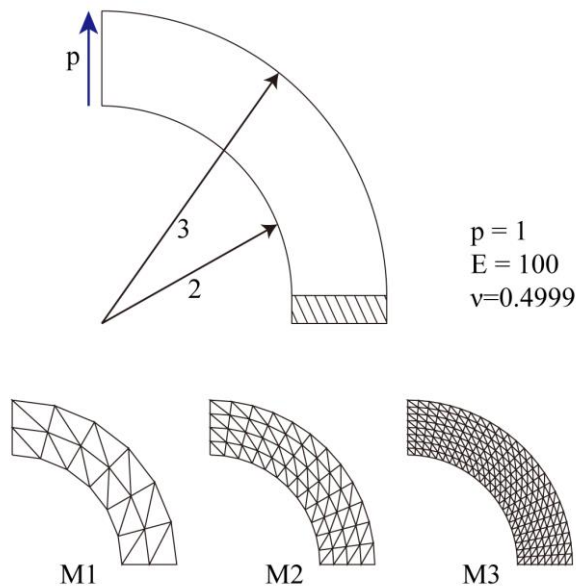


Figure 5.5. Description of the thick circular beam problem. The thick circular beam is under the tangential traction on the upper left end with clamped boundary on the lower right end. A set of meshes used in the numerical test is also plotted below the problem description.

The performance of 'OL6/3c' provides the most accurate solutions compared to other mixed overlapping elements Figure 5.6. It is remarkable that the accuracy 'OL6/3c' element is superior to all other triangular elements including both the conventional and overlapping finite elements, and comparable to the conventional quadrilateral elements. However, the loss of efficiency using 'OL6/3c' element is unavoidable compared to the conventional quadrilateral elements. The percent error of strain energy is 0.62 percent using 252 degree of freedoms, while the percent error is 0.39 percent with 130 degree of freedoms for 'Quad9/4c' elements (Table 5.3). Roughly speaking, nearly twice the degree of freedoms is required for the 'OL6/3c' element compared to the 'Quad9/4c' element. A user might have to consider the tradeoff between the convenience in triangular meshing for 'OL6/3c' element versus the computational efficiency of 'Quad9/4c' element.

The 'OL4/3c' element also showed a reasonable solution accuracy which are distributed along the similar level to solution accuracy of 'Quad9/4c' and 'OL6/3c'. However, in the aspect of the convergence shown in the Figure 5.6B, the rate of convergence is not as fast as other elements investigated. This slow convergence makes us hesitate to claim that the 'OL4/3c' element is an optimal choice, and more investigation is required which is provided in the following section, with extreme case.

On the other hand, 'OL3/1' element, regarding to the accuracy, shows relatively poor solutions compared to previous example problems. The convergence rate, shown in the Figure 5.6B seems reasonable, but the error levels in the coarse meshes is higher than the conventional mixed finite elements even including the conventional triangular elements. It seems that the linear enrichment of overlapping displacement field is insufficient for describing the bending behavior of thin structures.

In summary, when a bending is involved in slender structures, the optimal choice of mixed overlapping finite element is 'OL6/3c'.

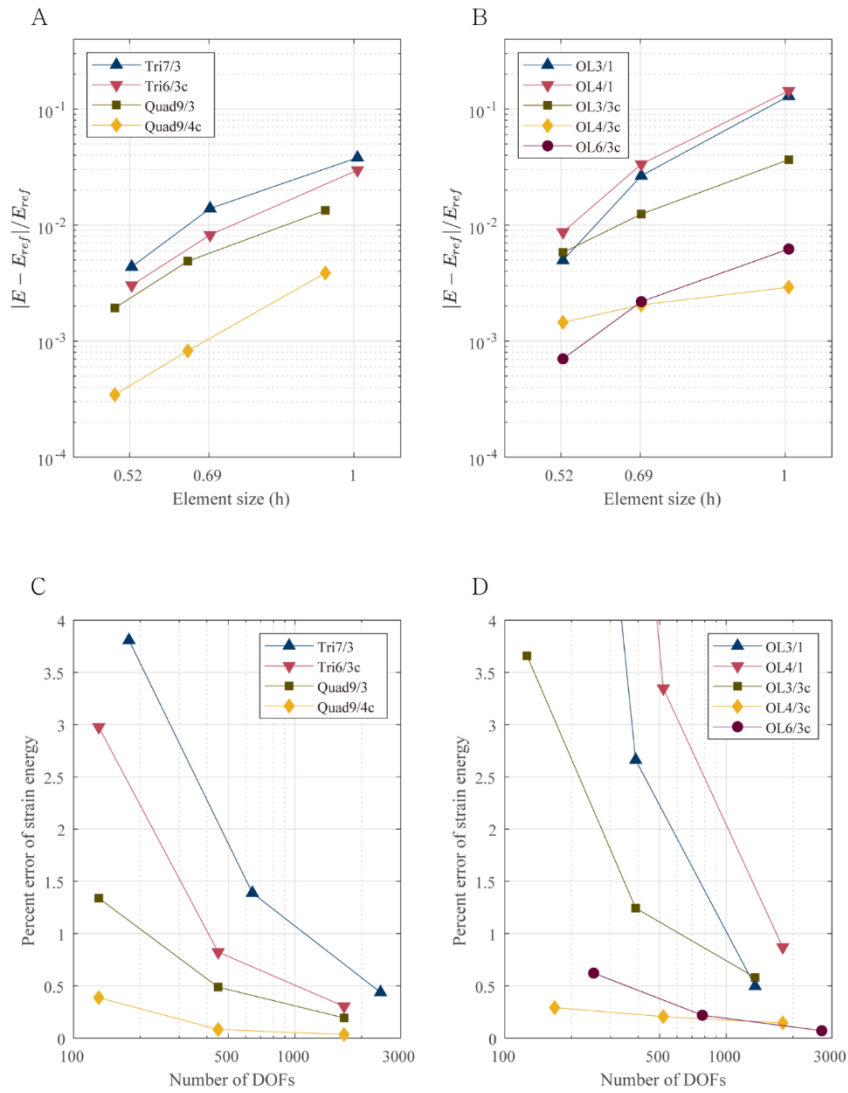


Figure 5.6. The strain energy error of thick circular beam problem. The convergence curve of (A) the conventional mixed finite elements and (B) the mixed overlapping elements in log scale. The percent error of strain energy of (C) the conventional mixed finite elements and (D) the mixed overlapping elements versus total number of the displacement degree of freedoms.

	Percent error [%]			Number of displacement degree of freedoms		
	M1	M2	M3	M1	M2	M3
Tri7/3	-3.81	-1.39	-0.44	178	642	2434
Tri6/3c	-2.98	-0.82	-0.30	130	450	1,666
Quad9/3	-1.34	-0.49	-0.19	130	450	1,666
Quad9/4c	-0.39	-0.08	-0.03	130	450	1,666
OL3/1	12.93	2.66	0.50	126	390	1,350
OL4/1	14.36	3.35	0.87	168	520	1,800
OL3/3c	-3.66	-1.24	-0.58	126	390	1,350
OL4/3c	-0.29	-0.20	-0.15	168	520	1,800
OL6/3c	0.62	0.22	0.07	252	780	2,700

Table 5.3. The percent error of the thick circular beam bending problem compared with the number of displacement degree of freedoms.

5.5 Thin circular beam

To further investigate the performance of mixed overlapping element in bending problem, we generate an extreme case of previous circular beam bending problem by introducing a very thin circular beam under shear loading. The details of geometrical and material characteristics are displayed in the Figure 5.7 as well as a set of meshes used in the numerical test.

The error convergence results given in the Figure 5.8A and B solidifies the conclusion derived in the previous thick circular beam problem.

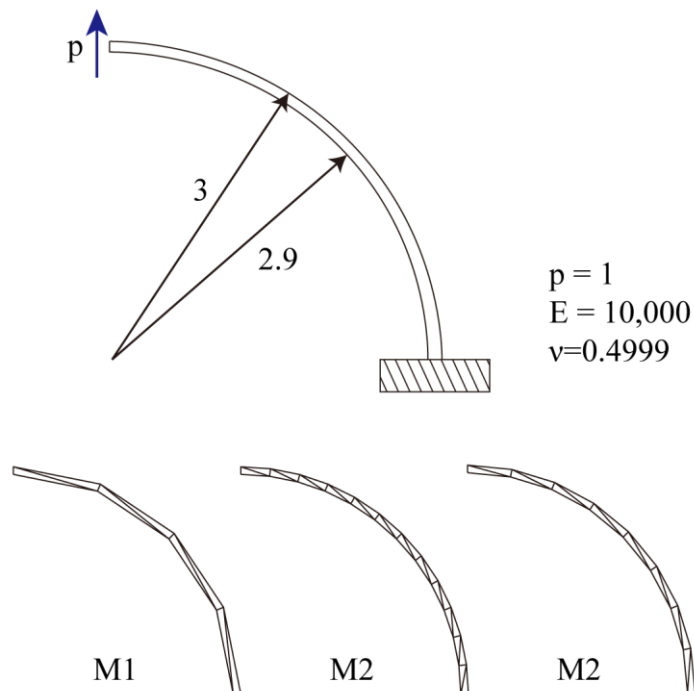


Figure 5.7. Description of the thin circular beam problem. The thin circular beam is under the tangential traction on the upper left end with clamped boundary on the lower right end. A set of meshes used in the numerical test is also plotted below the problem description.

The ‘OL6/3c’ is the only element that shows comparable result to the conventional quadrilateral elements. The convergence rate of ‘OL6/3c’ element is faster than any other tested elements including ‘Quad9/4c’ element, and the accuracy level is also comparable to those of conventional quadrilateral elements. The computational cost of ‘OL6/3c’ is roughly twice those of the conventional quadrilateral elements. The numbers of degree of freedoms are distributed between 120 and 312 to achieve 0.01 to 2.48 percent error in ‘OL6/3c’ element, while the numbers of degree of freedoms are distributed between 54 and 150 to achieve 0.54 to 2.89 percent error in conventional quadrilateral element (Table 5.4). There exists a tradeoff between the convenience in triangular meshing for ‘OL6/3c’ versus the computational efficiency of the quadrilateral elements.

The other mixed overlapping elements, including ‘OL3/1’, show poor solutions. The results imply that a linear or bilinear enrichment in overlapping displacement field is not sufficient for expressing bending behavior of thin structures, regardless of how many variables are used for the pressure approximation.

From the insights from the Sections 5.3 and 5.4, we conclude that the ‘OL6/3c’ should be selected when an extreme case such as bending of thin structures are treated, and that we can expect the accuracy level equivalent to those of conventional quadrilateral finite elements at the expense of some computational efficiency.

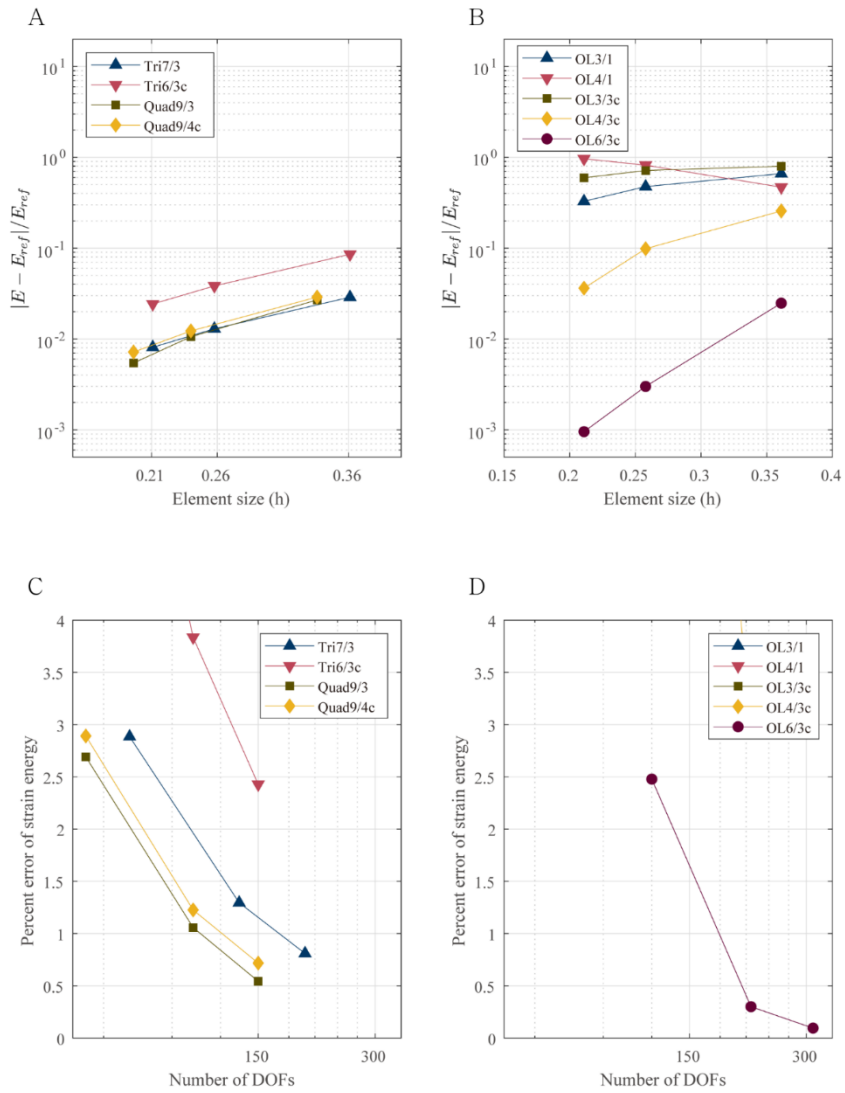


Figure 5.8. The strain energy error of thin circular beam problem. The convergence curve of (A) the conventional mixed finite elements and (B) the mixed overlapping elements in log scale. The percent error of strain energy of (C) the conventional mixed finite elements and (D) the mixed overlapping elements versus total number of the displacement degree of freedoms.

	Percent error [%]			Number of displacement degree of freedoms		
	M1	M2	M3	M1	M2	M3
Tri7/3	-2.88	-1.30	-0.81	70	134	198
Tri6/3c	-8.57	-3.84	-2.43	54	102	150
Quad9/3	-2.69	-1.06	-0.54	54	102	150
Quad9/4c	-2.89	-1.23	-0.72	54	102	150
OL3/1	-66.20	-47.64	-32.81	60	108	156
OL4/1	46.94	82.00	96.53	80	144	208
OL3/3c	-79.88	-71.62	-59.56	60	108	156
OL4/3c	-25.68	-9.85	-3.63	80	144	208
OL6/3c	2.48	0.30	0.10	120	216	312

Table 5.4. The percent error of the thin circular beam bending problem compared with the number of displacement degree of freedoms.

5.6 Conclusion

We investigated the accuracy and efficiency of mixed overlapping element by solving four numerical example problems in two-dimensional domain. The mixed overlapping elements used for the test are ‘OL3/1’, ‘OL4/1’, ‘OL3/3c’, ‘OL4/3c’, and ‘OL6/3c’ elements whose stability have been proven in Chapter 4 by performing numerical inf-sup test and examining the smoothness of the pressure distribution.

In general problems, such as cantilever plate problem and Cook’s membrane problem, the mixed overlapping element ‘OL3/1’ outperforms in the aspect of efficiency. The element, ‘OL3/1’, is more accurate than the conventional triangular mixed finite elements, such as ‘Tri7/3’ and ‘Tri6/3c’, even using smaller number of degree of freedoms. It is remarkable that ‘OL4/1’ element using a bilinear enrichment in displacement is poorer than ‘OL3/1’ element using a linear enrichment in displacement. This is contrary to the case of pure displacement based formulation where the bilinear enrichment is expected to be more accurate than the linear enrichment. In the case of displacement-pressure mixed formulation, the solution of ‘OL4/1’ can be degraded with a constant pressure space over-constraining the bilinearly enriched displacement space. Therefore, a linear enrichment of displacement is more adequate than a bilinear enrichment when a single pressure variable is used.

The element ‘OL6/3c’ showed the most accurate results. The accuracy of ‘OL6/3c’ element is similar or slightly better than the conventional quadrilateral mixed finite elements such as ‘Quad9/3’ and ‘Quad9/4c’, not to mention the conventional triangular elements. However, the quadratic enrichment in displacement can raise the total number of degrees of freedom and the continuous pressure assumption might raise the bandwidth of resulting stiffness matrix. For these reasons, ‘OL6/3c’ can be useful for the situations when the triangular meshing is only available, such as the case where the automatic meshing process is demanded for complex geometries where the quadrilateral meshing is restricted.

In particular problems, such as bending of a thick or thin circular beams, the mixed overlapping element, 'OL6/3c', solely outperforms the other elements. The accuracy of 'OL6/3c' is as accurate as the conventional mixed quadrilateral elements with slightly larger number of degrees of freedom. This implies that the linear and bilinear enrichment of displacement are still insufficient to express behavior of bending of thin structures. Only the quadratic enrichment well captures the bending behavior. This is the intrinsic limitations of linear and bilinear enrichment in displacement regardless of the mixed pressure variables. For example, the linearly and bilinearly enriched overlapping elements also show locking behavior in bending problem when the pure displacement based formulation is used.

In summary, the element 'OL3/1' is an accurate and efficient in general problems. However, if the analyzed system involves extreme cases like bending of a thin structure, using 'OL6/3c' element is preferable for those regions.

Chapter 6

Application to 3D problems : Protein dynamics

6.1 Introduction

Since the conformational dynamics of proteins plays an important role in determining their biological functions, it is important to predict the dynamics of proteins and to finally understand their functions. A lot of computational approaches for protein dynamics simulation have been suggested, such as the molecular dynamics simulation, all-atom based normal mode analysis, elastic network model, etc ⁵⁹⁻⁶². Molecular dynamics (MD) simulation is a classical and widely-used method to accurately predict the time-dependent trajectories of atoms by solving equations of motion based on full interatomic potential function ⁶¹. Although the method provides the solutions in quite a detailed manner, its demand for heavy calculation confines to analyzing only the small systems with the limited size of molecules and the limited time-scale. Instead, researchers concentrated on searching only the possible dominant motions by performing a normal mode analysis (NMA) perceiving that only the large collective motions of proteins participate in actual functioning. All-atom based NMA and elastic network model belong to this category ⁶³. However, NMA based models are performed in the environment of vacuum condition, neglecting the possible effect of the solvents.

On the other hand, finite element approach, which is of major interest in this study, can provide itself a prominent coarse-grained model ⁶⁴⁻⁶⁷. Also, the effect of

highly viscous solvent can be modeled simultaneously ⁶⁸. Since the motions of proteins occur in nanoscale level, intricate physics such as, elasticity of proteins in consideration with nonlocal theory or fluid dynamics considered at subcontinuum level, might enhance the quality of prediction. However, based on the knowledge that the conformal shapes of proteins are the major factor in determining those dynamic properties, we can generate a finite element protein model by considering the geometrical features of proteins. Once a finite element model is generated with its characteristic shapes well reflected, the stiffness and mass matrices can be calculated by assuming the proteins as homogeneous, isotropic linear elastic continua. The normal mode analysis can be performed using these stiffness and mass matrices by simply solving a generalized eigenvalue problem. The efficiency of finite element approach arises from the fact that the computational complexity can be controlled by adjusting the number of nodes of existing in the finite element protein models regardless of the size of the proteins. Since the boundary of proteins can be defined explicitly in the finite element model, we can consider the interaction between the boundary surface of protein and the solvent around the protein with more ease than the conventional atom-based models. That means, we can calculate the friction matrix, which can be used in Brownian mode analysis and Brownian dynamics simulation taking the effect of solvent into consideration.

The overall finite element procedures for the protein dynamics simulation is illustrated in the Figure **6.1**. From the molecular structure of interest, we generate a molecular surface representing the molecular structure. Then, we generate a solvent finite element model and a protein finite element model. The solvent finite element model reflects the viscous incompressible solvent environment around the protein's molecular surface, and the protein finite element model reflects the protein which is assumed as a compressible elastic body.

In this study, we generate two different procedures for finite element protein dynamics. The conventional procedure adopts 10-node tetrahedral mesh for both solvent and protein finite element models. In the new way of procedure, we adopt 4-node tetrahedral mesh for both solvent and protein model.

Since we perform an incompressible analysis in the solvent finite element model, using the 10-node tetrahedral mesh is an optimal option, which shows a stable solution when mixed with a constant pressure variable. The other options, such as 4-node tetrahedral mesh or 8-node hexahedral mesh, is not available in solvent finite element model. The 4-node tetrahedral mesh when mixed with a constant pressure variable behaves exactly same as the 4-node tetrahedral element with the pure displacement based formulation leading to volumetric locking phenomenon. The 8-node hexahedral mesh is often challengeable to discretize the complex regions of protein's molecular surface. Also 8-node hexahedral mesh when mixed with a constant pressure variable does not satisfy the inf-sup condition which leads to unstable checker-boarding pattern of pressure distribution. So, we should use the 10-node tetrahedral mesh mixed with a constant pressure variable for the solvent finite element model, which shows a stable solution. However, the use of 10-node tetrahedral mesh in solvent model confines us to use a 10-node tetrahedral mesh in protein model to match nodal coordinates of the surface nodes of proteins used in the solvent model and the protein model. Since a 4-node tetrahedral mesh is sufficient for a protein finite element model where compressible analysis is performed, the use of 10-node tetrahedral mesh in the protein finite element model leads to the loss of computational efficiency involving unnecessarily higher order elements.

To address this cost issue, we adopt the mixed overlapping element to the solvent finite element model. Since the stability of the mixed overlapping element with linear enrichment in displacement and a constant pressure variable was confirmed (in Section 4.4), we adopt a 4-node tetrahedral overlapping element with linear enrichment in the displacement and a constant pressure assumption. We label this element as 'OL4/1' element for it uses four polynomial terms for enrichment (1, x , y , z) and one pressure variable for pressure approximation. Once we calculate the friction matrix using the solvent finite element with 4-node tetrahedral mixed overlapping element, we can generate the protein finite element model using 4-node tetrahedral mesh also, which we expect the more enhanced efficiency in the

aspect of computational cost.

For convenience, we label the conventional procedure as ‘Tet10/1+Tet10’ which means that a conventional 10-node mixed tetrahedral element with a constant pressure variable is used for the solvent finite element model, and a conventional 10-node displacement-based tetrahedral element is used for the protein finite element model. Also, we label the new procedure as ‘OL4/1+Tet4’ which means that a 4-node mixed tetrahedral overlapping element with linearly enriched displacement and a constant pressure variable is used for the solvent finite element model, and a conventional 4-node displacement-based tetrahedral element is used for the protein finite element model.

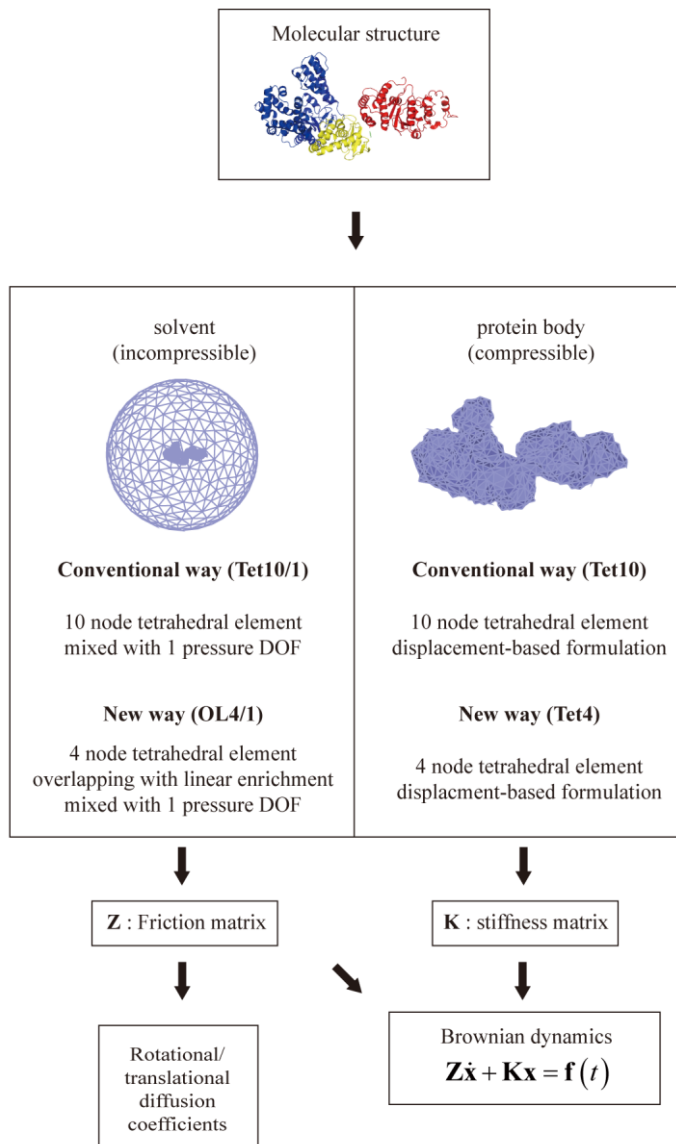


Figure 6.1. Finite element framework for the protein dynamics simulation. The X-ray crystal structure of Taq polymerase (Protein Data Bank ID 1TAQ) (*top*) is obtained from the Protein Data Bank and its molecular surface is calculated. Then, the finite element models for solvent and protein body are defined to calculate the friction matrix and stiffness matrix (*middle*). The matrices can be used for the calculation of diffusion coefficients, Brownian dynamics simulation, and Brownian mode analysis (*bottom*).

6.2 Generating finite element models for protein dynamics

6.2.1 Finite element modeling of protein

Finite element modeling consists of several steps including the construction of a molecular surface, generation of a three-dimensional volumetric mesh, and the calculation of stiffness and mass matrices. It begins with defining a molecular surface of the target protein, typically solvent-excluded-surface (SES), that is used to build a three-dimensional finite element model. The molecular surface is calculated by rolling a spherical probe, representing a solvent molecule, over the Van der Waals surface of the target protein structure ⁶⁹. We obtain the initial molecular surface using a freely available, MSMS version 2.6.1 ⁷⁰ (<http://mglttools.scripps.edu/packages/MSMS/>), that calculates the analytic surface first and then generates a triangulated surface mesh from the input atomic coordinates.

The initial molecular surfaces frequently contain several defects including self-intersection, non-manifolds, and isolated components that hinder the creation of clean and closed surfaces prerequisite to generate the volumetric mesh. Also, the initial molecular surface of proteins often consists of excessively many faces deteriorating the computational efficiency. Hence, successive mesh cleaning and reduction are usually performed in practice using a carefully designed sequence of mesh filtering algorithms available in an open source program, MeshLab ⁷¹ (<https://meshlab.sourceforge.net>). Automated mesh cleaning procedure used in this study is illustrated in detail in the Appendix **A4**.

The three-dimensional finite element model consisting of tetrahedrons is then constructed from the clean molecular surface using tessellation algorithms such as advancing front method and Delaunay triangulation. We use the commercial finite element analysis software, ADINA version 9.0.1 ⁷² (ADINA R&D, Inc., Watertown, MA, USA), for the volumetric meshing. Here, the characteristic shapes of proteins should sufficiently be depicted to effectively capture the functional motions of proteins ⁶⁷. For example, a complex geometry shown in Figure **6.2** (*left*) should be

used because it well depicts the characteristic shapes of proteins, painted red in the figure, whereas the characteristic shapes are neglected in a simple geometry shown in the Figure 6.2 (right). Tetrahedral meshing is unavoidable to describe the complex geometry of proteins because hexahedral meshing is often challengeable in complex geometry.

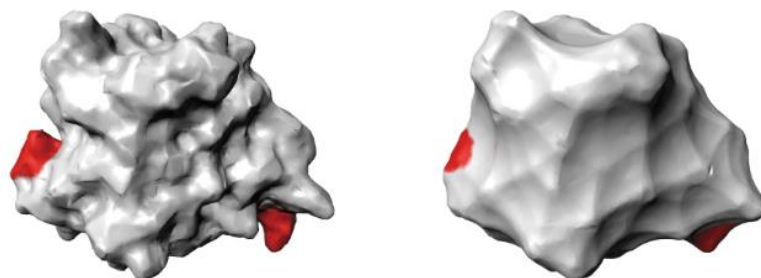


Figure 6.2. Molecular surface of C-terminal domain of bamC protein (Protein Data Bank ID: 2YH5) modeled with different surface parameters. The protein modeled with finer surface parameter (*left*) captures the detailed characteristic shapes of the protein than the protein modeled with coarse surface parameter (*right*).^①

^① This Figure is reproduced from: Giseok Yun, Jaehoon Kim, Do-Nyun Kim, *A critical assessment of finite element modeling approach for protein dynamics*, Journal of Computer-Aided Molecular Design, 2017, Springer

Since the incompressible analysis is not necessary in constructing the stiffness matrices from the protein finite element model, we use a pure displacement based formulation not the displacement-pressure mixed formulation. As a consequence, we use 10-node tetrahedral discretization for the conventional procedure, and we use 4-node tetrahedral discretization for the new procedure.

The stiffness and mass matrices are then calculated by assuming the proteins as homogeneous, isotropic, linear elastic bodies. The mass density of the protein model is defined to be the molecular mass per unit volume, and Poisson's ratio is set to 0.3. Young's modulus of the protein model is an adjustable parameter, which is obtained here by fitting the fluctuation profiles of the alpha-carbon atoms obtained using the finite element method to those calculated by performing the atomistic block normal analysis using a molecular dynamics simulation program, CHARMM⁷³.

6.2.2 Finite element modeling of solvent

We generate the solvent finite element model by meshing the empty space around the protein geometry. The molecular surface is generated using the program MSMS ver. 2.6.1⁷⁰ (<http://mgltools.scripps.edu/packages/MSMS/>). Then, the surface is coarsened using the surface simplification algorithm QSLIM, as implemented in MeshLab⁷¹ (<https://meshlab.sourceforge.net>). We embed the molecular surface in the voids represented by eleven layers of spheres whose radii vary from 1.4 to 400 times the largest dimension of a protein. The coarsened molecular surface and the spheres are imported into the finite element analysis program ADINA version 9.0.1⁷² (ADINA R&D, Inc., Watertown, MA, USA) for meshing (Figure 6.3). Here, as we have done in protein body modelling, we generate two different meshes for the solvent finite element model. First, we mesh the solvent geometry composed of molecular surface and the spheres with 10-node tetrahedral elements for the conventional procedure. We generate another mesh by using 4-node tetrahedral elements to mesh the solvent geometry. The 4-node tetrahedral model is used for a new procedure implementing the mixed overlapping element. Note that the protein body itself is not modeled, but the space around the protein is used.

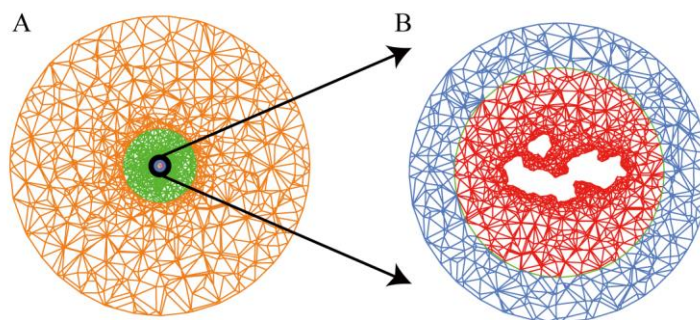


Figure 6.3. The cross-section of the mesh between the protein (Taq Polymerase) surface and the sphere. (A) All the eleven layers of the mesh are shown. (B) Only the two innermost layers of the mesh are shown. ^②

^② This figure is reproduced from: Computers and Structures, **196**, Reza Sharifi Sedeh, Giseok Yun, Jae Young Lee, Klaus-Jürgen Bathe, Do-Nyun Kim, *A framework of finite element procedures for the analysis of proteins*, pp.24-35, Copyright Elsevier.

6.2.3 Calculation of Friction matrix

For the calculation of the stiffness matrix, we consider following governing equations of the Stokes flow⁸.

$$\text{momentum:} \quad \frac{\partial \tau_{ij}}{\partial x_j} + f_i^B = 0 \quad (6.1)$$

$$\text{constitutive:} \quad \tau_{ij} = -p\delta_{ij} + 2\mu e_{ij} \quad (6.2)$$

$$\text{continuity:} \quad v_{i,i} = 0 \quad (6.3)$$

where

v_i = velocity of fluid flow in direction x_i

τ_{ij} = components of stress tensor

f_i^B = componenets of body force vector, here zero

p = pressure

δ_{ij} = Kronecker delta

μ = fluid (laminar) viscosity

e_{ij} = components of velocity strain tensor = $\frac{1}{2} \left(\frac{\partial v_i}{\partial x_j} + \frac{\partial v_j}{\partial x_i} \right)$

When the finite element approach is adopted to express these equations, we obtain the coefficient matrix identical to the matrix obtained in the incompressible analysis of a solid material considering that $[\mu]$ is equal to the shear modulus and velocities are interpreted as displacements. So, we can perform a three-dimensional structural analysis with implementing the displacement-pressure mixed finite element formulation since an incompressible analysis is considered.

For the conventional procedure, 10-node tetrahedral elements are used where the displacement are interpolated using 10 nodes (4 at the corners and 6 on the edges of a tetrahedron) and the element pressure is assumed to be constant. We use the notation “Tet10/1” element for the displacement-pressure mixed element which means that the element uses ten displacement degree of freedoms and one pressure degree of freedom.

For the new procedure, 4-node tetrahedral elements are used where the displacement are interpolated using linearly enriched overlapping displacement field (presented in the Section **2.3**) and the element pressure is assumed to be constant. We use the notation “OL4/1” element for the displacement-pressure mixed element, which means that the overlapping displacement field is enriched with four polynomial terms $(1, x, y, z)$ and one pressure degree of freedom is used.

Using the solvent finite element model (generated in the Section **6.2.2**), we apply unit velocities in succession, to each of the nodal degrees of freedom on the protein surface, with each time all other degrees of freedom on the protein surface set to zero. The resulting nodal forces acting onto protein surface nodes for a unit velocity applied to a surface node are corresponding column entries in the friction matrix \mathbf{Z} ⁶⁸.

6.3 Diffusion coefficients

The diffusion coefficient can provide an effective measure for validating the entries of the finite element friction matrix \mathbf{Z} . We proceed the validation by comparing the diffusion coefficients calculated from the friction matrix with analytical solution (for simple geometries) and data obtained in physical experiments. The detailed procedure for calculating the diffusion coefficients is described in the Appendix A5.

6.3.1 Diffusion coefficient of a reference sphere

We calculate the diffusion coefficients of a sphere of radius $r_{in} = 25 \text{ \AA}$ located in 20°C water. We embed the sphere in an incompressible medium, modeling water, of spherical geometry with radius r_{out} as shown in the Figure 6.4. Poisson's ratio of the medium is set to 0.4999 and its shear modulus is chosen equal to $60.34 \text{ Da}/(\text{ps \AA})$, which is the viscosity, μ , of water at 20°C . Considering the dynamic behavior and molecular properties of proteins, dalton, angstrom, and picosecond ($1 \text{ ps} = 10^{-12} \text{ s}$) are chosen as units for the mass, length, and time scales, respectively. As described in the Section 6.2.2, we generate two different versions of solvent finite element model using 'Tet10/1' and 'OL4/1' elements.

The reference values of the translational and rotational diffusion coefficients of the sphere with the radius of 25 \AA in 20°C water obtained from analytical solutions⁷⁴ are

$$D_t^{anal} = \frac{k_B T}{6\pi\mu r_{in}} = 8.57 \times 10^{-3} \text{ \AA}^2 / \text{ps} \quad (6.4)$$

$$D_r^{anal} = \frac{k_B T}{8\pi\mu r_{in}^3} = 1.03 \times 10^{-5} \text{ ps}^{-1} \quad (6.5)$$

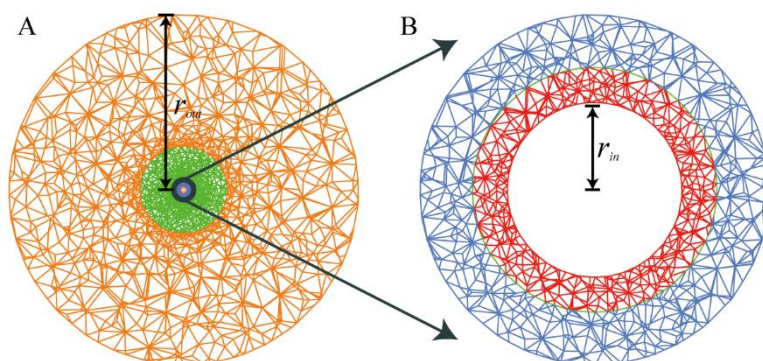


Figure 6.4. The cross-section of the mesh between the inner and outer spherical surfaces. (A) All the eleven layers of the mesh are shown. (B) Only the two innermost layers of the mesh are shown.^③

We use the same mesh discretization for both ‘Tet10/1’ and ‘OL4/1’ for validation meaning that the same number of elements are used for both finite element models consisting of 37,670 elements. However, the number nodes is different because ‘Tet10/1’ element uses additional midpoint nodes located at edges of each tetrahedron, while ‘OL4/1’ element uses only the nodes located at the corners of each tetrahedron. The solvent finite element model for ‘Tet10/1’ uses 171,865 nodes and the solvent finite element model for ‘OL4/1’ uses 6,380 nodes. The difference in the number of nodes results in the difference in the size of stiffness matrices used for calculating the friction matrix \mathbf{Z} . The size of stiffness matrices (lengths of column vectors of symmetric stiffness matrices) of the solvent finite element model are 515,595 for ‘Tet10/1’ version and 76,560 for ‘OL4/1’ version. Since the size of stiffness matrix for ‘Tet10/1’ is about seven times higher than the size of matrix for ‘OL4/1’, we can expect that ‘OL4/1’ be more computationally efficient when calculating the friction matrix. Additionally, final size of the friction matrix depends the number of nodes located on the surface boundary of the inner sphere (or protein) where the resulting nodal forces are

^③ This figure is reproduced from: Computers and Structures, **196**, Reza Sharifi Sedeh, Giseok Yun, Jae Young Lee, Klaus-Jürgen Bathe, Do-Nyun Kim, *A framework of finite element procedures for the analysis of proteins*, pp.24-35, Copyright Elsevier.

measured and collected. The numbers of surface nodes are 2,812 for ‘Tet10/1’ model and 463 for ‘OL4/1’ model. As a consequence, the resulting size of the friction matrix of ‘OL4/1’ model is reduced to one-sixth to the friction matrix size of ‘Tet10/1’. The detailed numeric information of finite element models for ‘Tet10/1’ and ‘OL4/1’ are also given in the Table **6.1**.

Although the computational cost is reduced largely in ‘OL4/1’ model, the percent errors in the rotational and translational diffusion coefficients were not significantly deteriorated compared to ‘Tet10/1’ model (Table **6.2**). The error in the translational diffusion coefficient is 0.21 percent in ‘OL4/1’ model, while the error in the translational diffusion coefficient is 0.04 percent in ‘Tet10/1’ model. Likewise, the error in the rotational diffusion coefficient is 0.6 percent in ‘OL4/1’ model, while the error in the rotational diffusion coefficient is 0.47 percent in ‘Tet10/1’ model.

In summary, we can achieve a friction matrix with reasonable accuracy and enhanced computational efficiency by using ‘OL4/1’ elements for the solvent finite element model.

	Tet10/1	OL4/1
Number of elements	37,670	37,670
Number of nodes	171,865	6,380
Size of stiffness matrix	515,595	76,560
Number of surface nodes	2,812	463
Size of friction matrix (surface node x 3)	8,436	1,389

Table 6.1. The comparison of solvent models for ‘Tet10/1’ and ‘OL4/1’.

	Tet10/1	OL4/1
Translational diffusion coefficient ($10^{-2} \text{ \AA}^2/\text{ps}$)	8.58	8.59
Rotational diffusion coefficient (10^{-5} ps^{-1})	1.03	1.02
Percent error (translational)	0.04	0.21
Percent error (rotational)	0.47	0.60

Table 6.2. The diffusion coefficients and percent errors of a reference sphere model calculated by ‘Tet10/1’ and ‘OL4/1’ models.

6.3.2 Diffusion coefficients of other proteins

Using the same procedure as the **Section 3.4.1**, we calculated the rotational and translational diffusion coefficients of ten different proteins (Table **6.3**) calculated by ‘Tet10/1’ model and ‘OL4/1’ model. The molecular surface of the protein is embedded in the incompressible medium (water) modeled with about 100,000 tetrahedral elements. The calculated diffusion coefficients are compared with the experimental values. All the experimental and calculated diffusion coefficients are given for the viscosity of water at 20°C, except for two proteins (Protein Data Bank ID : 2DN2, 1DWR) which are provided for the viscosity of 66.24 Da/(ps Å). All the reported experimental diffusion coefficients are obtained from the work of García de la Torre ⁷⁵, except for those of two proteins (Protein Data Bank ID : 2DN2, 1DWR) from the work of Miller ⁷⁶. As shown, the calculated diffusion coefficients both from ‘Tet10/1’ model and ‘OL4/1’ model match very well with the experimentally measured data, particularly considering the case of translation.

To compare the computational costs of ‘Tet10/1’ model and ‘OL4/1’ model, we listed, in the Table **6.4**, the size of the stiffness matrix of the solvent finite element model and the size of resulting friction matrix calculated from ‘Tet10/1’ model and ‘OL4/1’ model. Ten different proteins are considered for the comparison of the computational cost.

The stiffness matrices calculated from ‘Tet10/1’ model have the size of 556,995 to 635,817, whereas the stiffness matrices calculated from ‘OL4/1’ model have the size of 78,972 to 106,176. The stiffness matrices from ‘Tet10/1’ model have approximately six to seven times the stiffness matrices from ‘OL4/1’ model. This implies that the required computational time for ‘OL4/1’ model is much less than the time required for ‘Tet10/1’ model when solving the solvent finite element model and calculating the friction matrix.

In addition, the size of the friction matrix, which is three times the number of protein’s surface nodes, play an important role in the Brownian dynamics simulation. The number of protein’s surface node determines the number of nodes inside the protein’s body, and eventually determines the final size of the stiffness

matrix of finite element protein model used in the Brownian dynamics simulation. The friction matrices calculated from ‘Tet10/1’ model have the size of 4,674 to 12,060, whereas the friction matrices calculated from ‘OL4/1’ model have the size of 1,173 to 3,021. The friction matrices calculated from ‘Tet10/1’ model have approximately four times the friction matrices calculated from ‘OL4/1’. This means that using the overlapping element scheme is advantageous in computational efficiency when performing the Brownian dynamics simulation, which will be treated again in the next section **6.4**.

Rotational diffusion coefficient (10^{-5} ps ⁻¹)			Translational diffusion coefficient (10^{-2} Å ² /ps)			Weight (kDa)	PDB ID
Tet10/1	OL4/1	Experiment	Tet10/1	OL4/1	Experiment		
4.87	4.67	4.17	1.46	1.46	1.29	7	4PTI
2.46	2.35	N.A.	1.17	1.16	1.07	14	1RBX
2.63	2.56	2.6	1.17	1.18	1.09	14	193L
1.97	1.86	1.72	1.08	1.07	1.02	18	1DWR
1.36	1.28	N.A.	0.95	0.94	0.93	26	2CGA
0.84	0.80	0.75	0.81	0.80	0.78	37	1BEB
0.61	0.59	0.44	0.72	0.71	0.69	65	2DN2
0.23	0.22	N.A.	0.52	0.52	0.5	143	2GPD
0.18	0.18	N.A.	0.49	0.49	0.45	158	1ADO
0.16	0.15	N.A.	0.46	0.46	0.4	233	2MIN

Table 6.3. The diffusion coefficients calculated by conventional ‘Tet10/1’ model and ‘OL4/1’ model. The experimental values are also included for 10 different proteins whose atomic structures are obtained from Protein Data Bank (PDB).

Size of stiffness matrix of the solvent FE model		Size of friction matrix		Structure weight (kDa)	PDB ID
Tet10/1	OL4/1	Tet10/1	OL4/1		
556,995	78,972	4,674	1,173	7	4PTI
616,092	93,216	9,186	2,301	14	1RBX
603,603	97,740	10,914	2,733	14	193L
575,382	84,636	7,254	1,818	18	1DWR
599,718	87,840	8,970	2,247	26	2CGA
635,817	104,700	12,000	3,000	37	1BEB
612,900	90,276	14,520	2,304	65	2DN2
629,265	106,176	12,060	3,021	143	2GPD
624,774	103,440	11,982	3,000	158	1ADO
620,535	100,260	10,887	2,727	233	2MIN

Table 6.4. The size of the stiffness matrix of the solvent FE model, and the size of the friction matrix of resulting friction matrix. The matrices calculated from ‘Tet10/1’ model and ‘OL4/1’ model are compared for ten different proteins.

6.4 Brownian dynamics simulation

We perform the Brownian dynamics simulation for two different procedures, the conventional and the new way. In conventional procedure, we use the friction matrix calculated from ‘Tet10/1’ model, and use the stiffness matrix calculated using 10-node tetrahedral element. We label this procedure as ‘Tet10/1+Tet10’ model. In the new procedure, we use the friction matrix calculated from ‘OL4/1’ model, and use the stiffness matrix calculated using 4-node tetrahedral element. We label this new procedure as ‘OL4/1+Tet4’ model.

To present and compare the results from Brownian dynamics simulation from two different procedures, we considered three sample proteins with different molecular weights: Lysozyme (14.4 kDa), Taq polymerase (94.4 kDa), and GroEL (810.1 kDa). The initial structures of Lysozyme, Taq polymerase, and GroEL are taken, respectively, from the works by M. Vaney et al.⁷⁷ (Protein Data Bank ID 193L), by Y. Kim et al.⁷⁸ (Protein Data Bank ID 1TAQ), and by C. Bartolucci et al.⁷⁹ (Protein Data Bank ID 1XCK).

6.4.1 Procedures for Brownian dynamics

We follow the same procedure of previous work done by Sedeh et al.⁶⁸ for calculating Brownian dynamics trajectories. The equations of Brownian dynamics simulation is given as following neglecting the inertial forces of classical Langevin equation⁸⁰.

$$\mathbf{Z}\dot{\mathbf{x}} + \mathbf{K}\mathbf{x} = \mathbf{f}(t) \quad (6.6)$$

Here, the friction matrix, \mathbf{Z} , is calculated from the solvent finite element model, and the stiffness matrix \mathbf{K} , is calculated from the protein finite element model as illustrated in the section 6.2. The force vector, $\mathbf{f}(t)$, is an vector composed of external stochastic forces with the following conditions.

$$\begin{aligned}\langle f_i(t) \rangle &= 0 \\ \langle f_i(t) \cdot f_j(t') \rangle &= 2k_B T Z_{ij} \delta(t-t')\end{aligned}\tag{6.7}$$

The bracket notations in above equation (eq.2) means the time-averaged value, k_B is Boltzmann's constant, T is the temperature, $\delta(t-t')$ is the Dirac delta function, $f_i(t)$ is the i -th component of $\mathbf{f}(t)$, and \mathbf{Z}_{ij} is the ij -th component of the friction matrix \mathbf{Z} .

We perform the time integration for the Brownian dynamics equation (eq.20) using the predefined simulation duration and time step size to obtain the time trajectories of a protein finite element model⁶⁸. We illustrate the detailed procedures for time integration in the Appendix **A6**.

6.4.2 Results

We determine the duration and the time-step size of the simulation, for each sample protein, by following the rules established in the works by Sedeh et al.⁶⁸. First, the largest relaxation time of Taq polymerase is ~ 537 ps. We simulated the time trajectories for the time duration of 300,030 ps, which is about 559 times the relaxation time. The time duration was defined for the simulation data to be compared with the experimental dynamic form factor data, which are available up to $\sim 30,000$ ps. We excluded the results of the first 50 ps and used the results for the next 300,000 ps for sampling the time trajectory of atom coordinates. We use the time-step size of 1 ps. The appropriate duration and the time-step size for Lysozyme and GroEL are determined by employing the same ratios from the maximum relaxation time as we used in the Taq polymerase simulation. For example, the simulation time is the 559 times the largest relaxation time, and the time step size is $1/537^{\text{th}}$ of the largest relaxation time. The largest relaxation time of Lysozyme and GroEL are ~ 119 ps and 60,792 ps. We perform the Brownian dynamics simulation for 66,492 ps with the time-step size of 0.22 ps for Lysozyme,

and simulation for 33,967,671 ps with the time-step size of 133.21 ps for GroEL. We performed a total of ten Brownian dynamics simulations for each sample protein and collect the average values. We present the root-mean-square fluctuations of residues from calculated from the Brownian dynamics simulation and compared with those calculated using the molecular dynamics simulation in Figure 6.5, 6.6, and 6.7. The root-mean-square fluctuations of each residue are calculated at the location of its corresponding α -carbon atom. Root-mean-square fluctuations is the quantity to characterize the conformational variance of a protein structure, and can be computed from the molecular trajectories obtained using a molecular dynamics or Brownian dynamics simulation. The root-mean-square fluctuation values of atom i can be expressed as

$$\langle \Delta r_i^2 \rangle^{1/2} = \left\langle \left((x_i(t) - \bar{x}_i)^2 + (y_i(t) - \bar{y}_i)^2 + (z_i(t) - \bar{z}_i)^2 \right)^{1/2} \right\rangle \quad (6.8)$$

where $x_i(t)$, and $y_i(t)$, and $z_i(t)$ denote the atomic coordinates of atom i at time t with translational and rotational rigid body motions removed, and \bar{x}_i , \bar{y}_i , and \bar{z}_i denote the mean position of atom i over the simulation time. As can be seen in the Figure 6.5, 6.6, and 6.7, the root-mean-squared fluctuation calculated from the Brownian dynamics simulation with the new procedure ('OL4/1+Tet4') and the conventional procedure ('Tet10/1+Tet4') show high correspondence with each other. In addition, the root-mean-squared fluctuation from both the conventional and new Brownian dynamics procedures well follow those calculated from the molecular dynamics simulation. To illustrate the quantities in detail, we also calculated the Pearson correlation between the root-mean-square fluctuation calculated from the Brownian dynamics simulation and the molecular dynamics simulation to compare the accuracy of the results for the Brownian dynamics simulation. Pearson correlation coefficient is defined as

$$\rho_{Pearson} = \frac{\sum_i (X_i - \mu_X) \cdot (Y_i - \mu_Y)}{\sqrt{\sum_i (X_i - \mu_X)^2 \sum_i (Y_i - \mu_Y)^2}} \quad (6.9)$$

where X_i and Y_i indicate the root-mean-square fluctuations amplitudes at atom i with their mean values, μ_X and μ_Y , obtained using the Brownian dynamics and molecular dynamics trajectories, respectively. We list the values of calculated Pearson correlation coefficients in the Table **6.5**, **6.6**, and **6.7**, which show high correlation between different approaches.

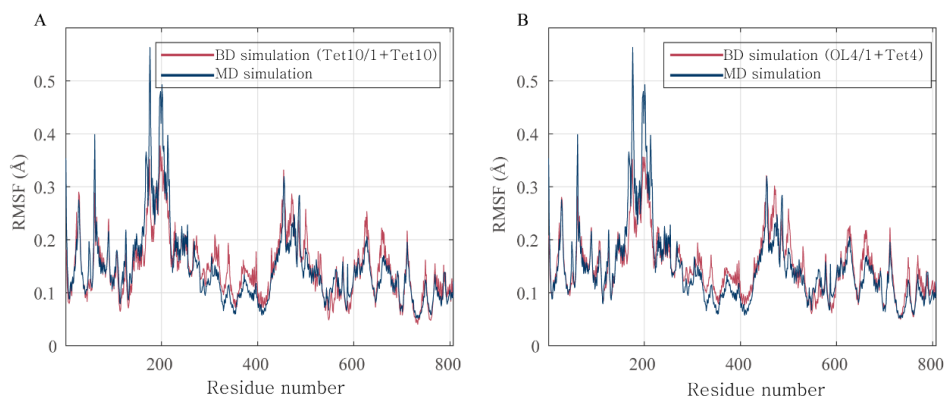


Figure 6.5. The root-mean-square fluctuations (RMSFs) of residues of Taq polymerase obtained using the Brownian dynamics (BD) trajectories compared with those calculated using the molecular dynamics (MD) simulation. The Brownian dynamics trajectories are obtained from (A) the conventional procedure (Tet10/1+Tet10) and (B) the new procedure (OL4/1+Tet4).

	BD simulation (Tet10/1+Tet10)	BD simulation (OL4/1+Tet4)	MD simulation
BD simulation (Tet10/1+Tet10)	1	0.99	0.88
BD simulation (OL4/1+Tet4)	0.99	1	0.89
MD simulation	0.88	0.89	1

Table 6.5. Pearson correlation of root-mean-square fluctuations of Taq polymerase obtained using the Brownian dynamics simulation with two different procedures and the molecular dynamics (MD) simulation.

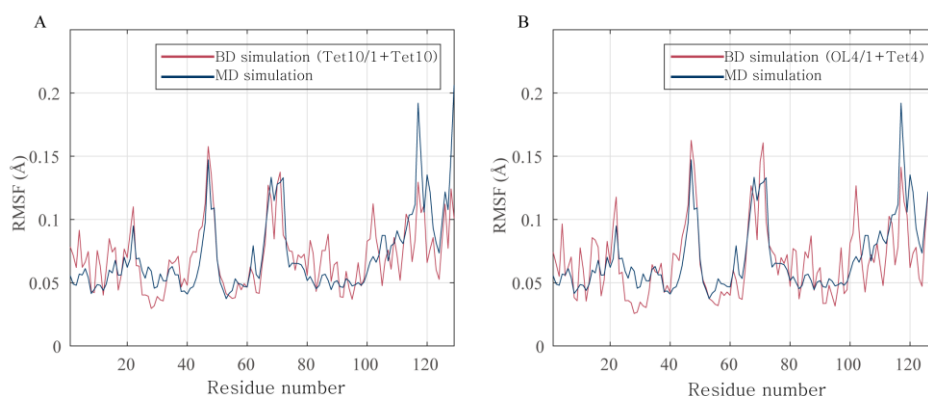


Figure 6.6. The root-mean-square fluctuations (RMSFs) of residues of Lysozyme obtained using the Brownian dynamics (BD) trajectories compared with those calculated using the molecular dynamics (MD) simulation. The Brownian dynamics trajectories are obtained from (A) the conventional procedure (Tet10/1+Tet10) and (B) the new procedure (OL4/1+Tet4).

	BD simulation (Tet10/1+Tet10)	BD simulation (OL4/1+Tet4)	MD simulation
BD simulation (Tet10/1+Tet10)	1	0.99	0.73
BD simulation (OL4/1+Tet4)	0.99	1	0.73
MD simulation	0.73	0.73	1

Table 6.6. Pearson correlation of root-mean-square fluctuations of Lysozyme obtained using the Brownian dynamics simulation with two different procedures and the molecular dynamics (MD) simulation.

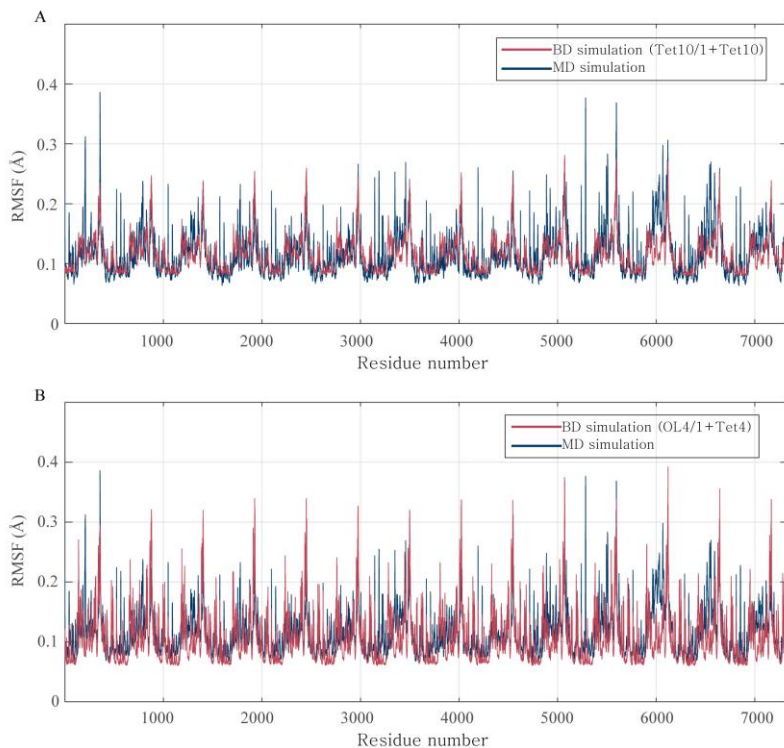


Figure 6.7. The root-mean-square fluctuations (RMSFs) of residues of GroEL obtained the molecular dynamics (MD) simulation. The Brownian dynamics trajectories are obtained from (A) the conventional procedure (Tet10/1+Tet10) and (B) the new procedure (OL4/1+Tet4).

	BD simulation (Tet10/1+Tet10)	BD simulation (OL4/1+Tet4)	MD simulation
BD simulation (Tet10/1+Tet10)	1	0.90	0.59
BD simulation (OL4/1+Tet4)	0.90	1	0.65
MD simulation	0.59	0.65	1

Table 6.7. Pearson correlation of root-mean-square fluctuations of GroEL obtained using the Brownian dynamics simulation with two different procedures and the molecular dynamics (MD) simulation.

6.4.3 Computational efficiency

In the aspect of computational efficiency, the finite element based Brownian dynamics simulation has several advantages over the classical molecular dynamics simulation. In a classical molecular dynamics simulation, the degrees of freedom increase with the molecular weight of analyzed proteins, which often limits the molecular size and the simulated time scale.

On the other hand, in finite element Brownian dynamics, we consider only the representative molecular surface of analyzed proteins, which means that users can control the total number of degrees of freedoms by adjusting the refinement level of triangular discretization of molecular surface. Since the low mode response of a protein is largely governed by only its overall shape⁶⁴⁻⁶⁷, appropriate finite element models are constructed using a similar number of nodes for proteins of similar shapes regardless of the size and weight of the proteins. Hence, the number of atoms comprising a protein is not a direct consideration in the finite element modeling of a protein for a Brownian dynamics simulation.

Despite this efficiency of finite element based Brownian dynamics, the conventional procedure for the Brownian dynamics simulation still has a disadvantageous factor, the usage of 10-node tetrahedral elements, which affects the computational cost in negative way. In conventional procedure, ‘Tet10/1’ element is an optimal choice among the conventional mixed finite elements to treat the incompressible analysis involved in the solvent model. The lower order mixed tetrahedral element, such as ‘Tet4/1’ element, behaves exactly same as the pure displacement based element (Tet4), which is not appropriate for the incompressible analysis. The lower order mixed hexahedral element, such as ‘Hex8/1’ element, still has an instability issue showing the checkerboard patterns in pressure distribution. Also the meshing process might be laborious to generate hexahedral discretization for the complex geometries of proteins. The adoption of ‘Tet10/1’ element for the solvent model confines the pairing protein model to use ‘Tet10’ element only, since the surface nodes of the solvent and the protein models should be matched. Using the higher order element (Tet10) for the protein model (where

the linear tetrahedral element is sufficient) causes unnecessarily large number of nodes generated in the protein model.

In the new procedure, however, we can treat both the solvent and protein model using 4-node tetrahedral meshes. For the incompressible analysis in the solvent model, the mixed overlapping element, 'OL4/1', can provide a reasonable solution using 4-node tetrahedral meshes. Subsequently, we can use 4-node tetrahedral (Tet4) elements for the paring protein model, still matching the surface nodes of the solvent and the protein models. Therefore, the number of nodes generated in the protein model can be reduced largely by using only the 'Tet4' elements for the protein model.

We compare the number of nodes generated by two different procedures for three analyzed proteins in the Figure **6.8A**. The detailed numbers are also listed in Table **6.8**, **6.9**, and **6.10**. In the conventional procedure, the number of nodes generated are, respectively, 11,279, 9,756, and 12,827 for Lysozyme, Taq polymerase and GroEL. In the new procedure, the number of nodes generated are, respectively, 2,053, 1,808, and 2,235 for Lysozyme, Taq polymerase and GroEL. The conventional procedure generates the nodes for about five times the new procedure.

Subsequently, we compare the computational time taken in two different procedures for three analyzed proteins in the Figure **6.8B**. The detailed numbers are also listed in Table **6.8**, **6.9** and **6.10**. The conventional procedure requires 31.5 to 49.37 hours per simulation whereas the new procedure requires only 0.83 to 1.84 hours per simulation. The new procedure, roughly speaking, is about thirty times faster than the conventional procedure.

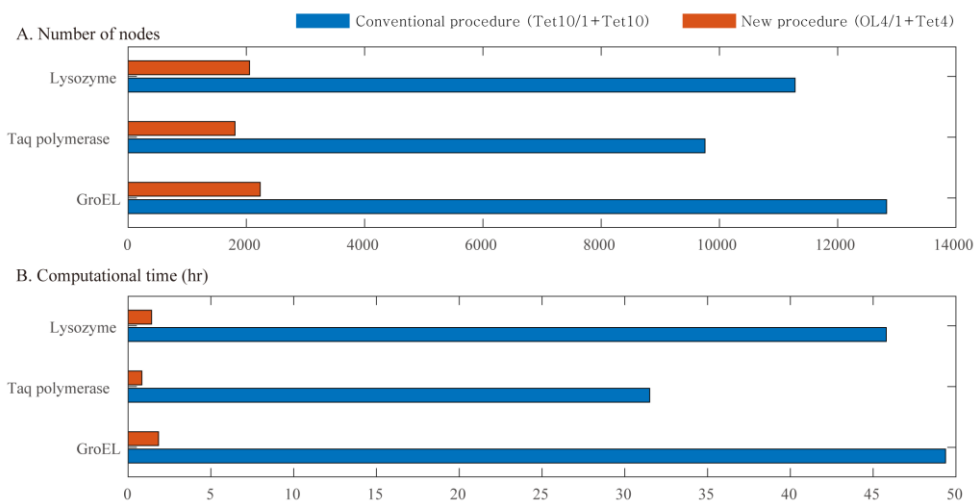


Figure 6.8. The comparisons of (A) the number of nodes and (B) the computational time between two different procedures for the Brownian dynamics simulation. Brownian dynamics for both procedures were simulated using the same computational machine (Intel[®] Xeon[®] CPU E-5-2407 with 2.2GHz (CPU)).

Lysozyme (14.4 kDa)		
Brownian dynamics simulation Intel® Xeon® CPU E-5-2407 with 2.2GHz (CPU)		
	Conventional procedure (Tet10/1+Tet10)	New procedure (OL4/1+Tet4)
Simulated physical time (ps)	66,492	66,492
Time step size (ps)	0.22	0.22
Number of nodes	11,279	2,053
Computational time (hr)	45.79	1.42
Molecular dynamics simulation GPU-cluster: Intel® Xeon® CPU-E5-3630 with 2.4GHz + NVIDIA® Tesla® K80, 6EA		
Number of atoms	27,536	
Time step size (ps)	0.002	
Computational time for 10,000- ps-long simulation (hr)	4.96	

Table 6.8. Analysis information of Brownian dynamics simulation and molecular dynamics simulation for Lysozyme.

Taq polymerase (94.4 kDa)		
Brownian dynamics simulation Intel® Xeon® CPU E-5-2407 with 2.2GHz (CPU)		
	Conventional procedure (Tet10/1+Tet10)	New procedure (OL4/1+Tet4)
Simulated physical time (ps)	300,050	300,050
Time step size (ps)	1.0	1.0
Number of nodes	9,756	1,808
Computational time (hr)	31.50	0.83
Molecular dynamics simulation GPU-cluster: Intel® Xeon® CPU-E5-3630 with 2.4GHz + NVIDIA® Tesla® K80, 6EA		
Number of atoms	162,761	
Time step size (ps)	0.002	
Computational time for 10,000- ps-long simulation (hr)	19.68	

Table 6.9. Analysis information of Brownian dynamics simulation and molecular dynamics simulation for Taq polymerase.

GroEL (810.1 kDa)		
Brownian dynamics simulation Intel® Xeon® CPU E-5-2407 with 2.2GHz (CPU)		
	Conventional procedure (Tet10/1+Tet10)	New procedure (OL4/1+Tet4)
Simulated physical time (ps)	33,967,671	33,967,671
Time step size (ps)	133.21	133.21
Number of nodes	12,827	2,235
Computational time (hr)	49.37	1.84
Molecular dynamics simulation GPU-cluster: Intel® Xeon® CPU-E5-3630 with 2.4GHz + NVIDIA® Tesla® K80, 6EA		
Number of atoms	535,480	
Time step size (ps)	0.002	
Computational time for 10,000- ps-long simulation (hr)	68.55	

Table 6.10. Analysis information of Brownian dynamics simulation and molecular dynamics simulation for GroEL.

6.5. Conclusion

The finite element procedures for the Brownian dynamics simulation provides an efficient way of analyzing the dynamic properties of proteins compared to the classical molecular dynamics simulation. Still the conventional procedure for the Brownian dynamics simulation has its limitations in the aspect of computational cost, since that the adoption of higher order tetrahedral element is enforced in analyzing the incompressible solvent model. The use of higher order element in the solvent model leads to the use of higher order element in the protein model, which finally causes the resulting finite element model to be computationally burdensome. To address this issue, we adopt 4-node tetrahedral mesh and use the mixed overlapping element, 'OL4/1', to solve the incompressible problem of the solvent model. Adopting the 'OL4/1' element to the solvent model makes it possible to use a lower order element, 'Tet4' element, for the pairing protein model. Using this new procedure, we can obtain the similar Brownian dynamics trajectories of proteins with high accuracy. By using the lower order element for the protein model, in the new procedure, we can reduce the number of nodes largely compared to the conventional procedure, which uses higher order element for the protein model. This new procedure of Brownian dynamics simulation is presented as an application example of mixed overlapping element examined in this study.

Chapter 7

Concluding remark

We presented the procedure for the displacement-pressure mixed formulation using the overlapping element for the incompressible analysis. Unlike the conventional mixed finite elements, which were confined only to the high-order elements for the stability issue, we could achieve the mixed formulation of the overlapping element using lower-order triangles or tetrahedrons. In overlapping element, using the low-order triangles or tetrahedrons was possible due to its displacement function spaces enlarged by the local field functions and the enrichment functions. The stability tests proceeded by the numerical inf-sup test and the examination of pressure solutions imply that the mixed overlapping elements of ‘OL3/1’, ‘OL4/1’, ‘OL3/3c’, ‘OL4/3c’, and ‘OL6/3c’ show the stability regardless of the mesh patterns. Subsequent performance test, by solving the numerical example problems using those stable mixed overlapping elements, show that the ‘OL3/1’ element outperforms in general problems compared to the conventional high-order triangular elements. The ‘OL6/3c’ element was the mixed overlapping element showing the best accuracy even when the extreme case, such as bending of thin structures, are considered at the expense of some computational efficiency. So in general, ‘OL3/1’ would be a fair choice, but for extreme case where the higher accuracy is required, ‘OL6/3c’ could be a good choice.

Moreover, we showed a practical example of three-dimensional problem introducing the finite element procedure of protein dynamics. The conventional

procedure adopted the high-order tetrahedral element to solve the incompressible media around the protein structure which causes the increase of computational cost. However, the new procedure adopting the mixed overlapping element of linearly enriched overlapping element mixed with a constant pressure has achieved in reducing the computational cost significantly without the loss of accuracy.

We expect our study can provide a guideline for selecting the proper mixed overlapping element for the incompressible analysis.

For further studies, we expect to enhance the performance of mixed overlapping elements by reducing the computational cost even more which have been raised due to the degrees of freedom corresponding to the enriched polynomial terms or by enhancing the displacement approximation itself. Although the concept of overlapping element is established upon the solid backgrounds such as meshless methods, there remains demands for the overlapping element to be much more enhanced in the aspect of displacement approximation. For example, enlarged displacement function space of overlapping element lets the mixed formulation to be possible. However, for discontinuous pressure group, our study shows that higher order pressure assumptions, other than constant pressure assumption, are not available due to the inf-sup instability. It will be worth developing the overlapping element further to achieve the higher order mixed formulation to be possible without further increasing the enrichment order of overlapping element. For this reason, alternative methods using different interpolation scheme, such as isogeometric analysis, enhanced assumed strain method, etc. In addition, in order to achieve more efficiency, additional stability tests can be done for the coupling elements, which lie between the traditional finite element and the overlapping element, so we can use the mixed traditional finite element in combination with the mixed overlapping element as in the AMORE paradigm.

Chapter A

Appendix

A1. Remarks on pressure interpolation

We used standard linear shape functions in approximating pressure field for the mixed overlapping elements of continuous pressure type, such as ‘OL3/3c’, ‘OL4/3c’, and ‘OL6/3c’. Since we adopt the concept of overlapping element to approximate the displacement field, it is natural to question whether it is possible to use the new shape functions derived from the overlapping element also in approximating the pressure field instead of using standard shape functions.

In addition to the mixed overlapping elements with those pressure interpolated by standard linear shape functions (the ones presented in the Section 3.3), we organized additional test set of mixed overlapping elements whose pressure fields are approximated by overlapping element with linear and bilinear polynomial basis.

We present the inf-sup test results, in the Figure A1.2 and Figure A1.3, when the new shape functions derived from the linearly and bilinearly enriched overlapping element are used in pressure approximation. The test result of ‘OL3/3c’ element clearly show that the inf-sup values are converging to zero when the pressure field of ‘OL3/3c’ element is modified by the linearly or bilinearly enriched overlapping element. Also, the inf-sup values of ‘OL4/3c’ and ‘OL6/3c’ elements with those pressure field interpolated by the overlapping shape functions are highly dependent on the mesh patterns which we cannot tell that those elements are stable.

We also compared the convergence curve of the strain energy error of cantilever plate problem dealt in the Section 5.2. The convergence curves compared in Figure A1.4 clearly shows that the mixed overlapping elements with those pressure field interpolated by the standard linear shape functions is superior to the other test set using overlapping pressure interpolation.

The inf-sup test and convergence test suggest that we cannot expect further benefits from using the modified shape functions derived from the overlapping element instead of using standard linear shape functions.

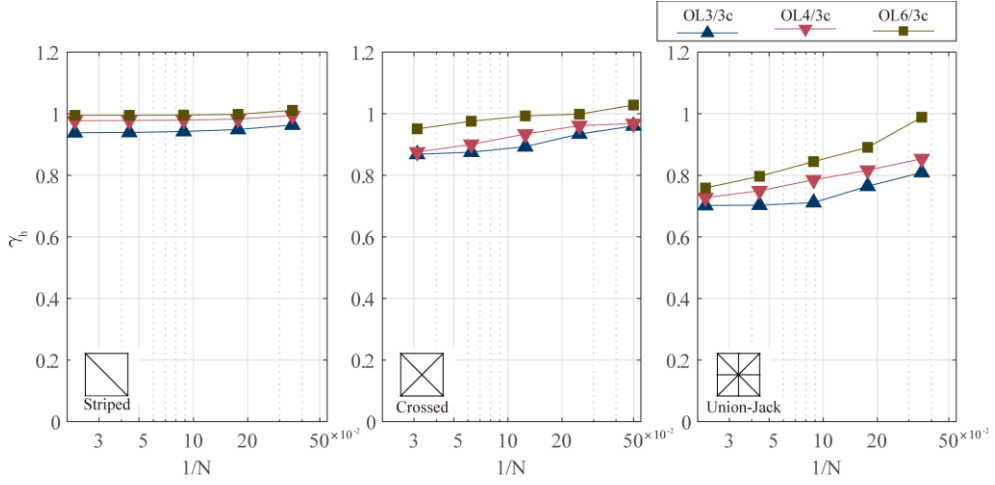


Figure A1.1. The numerical inf-sup values of the mixed overlapping element formulated with the continuous pressure approximated by the standard linear shape functions.

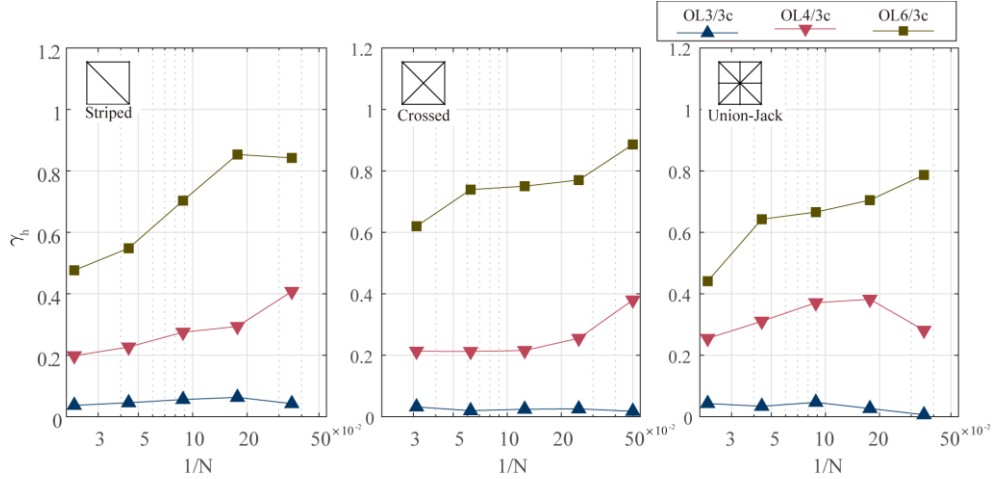


Figure A1.2. The numerical inf-sup values of the mixed overlapping element formulated with the continuous pressure approximated by the overlapping element enriched by linear polynomial basis.

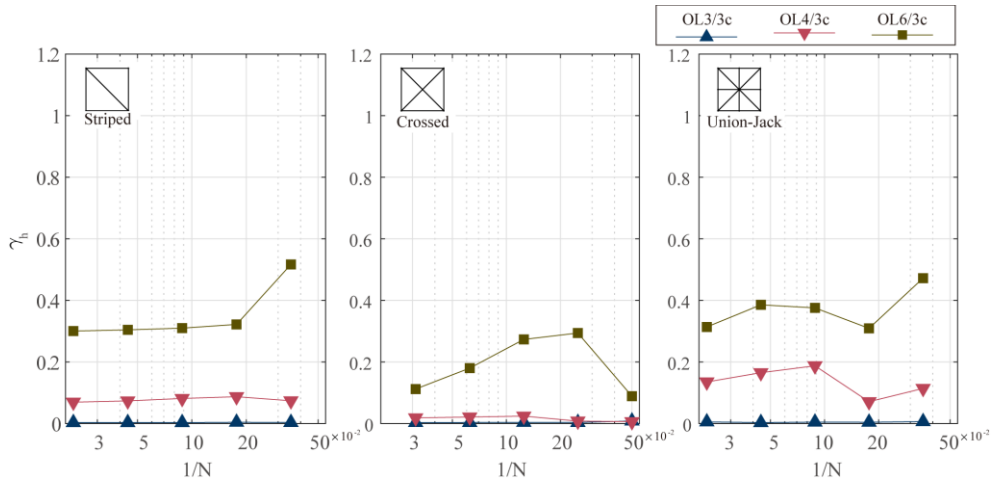


Figure A1.3. The numerical inf-sup values of the mixed overlapping element formulated with the continuous pressure approximated by the overlapping element enriched by bilinear polynomial basis.

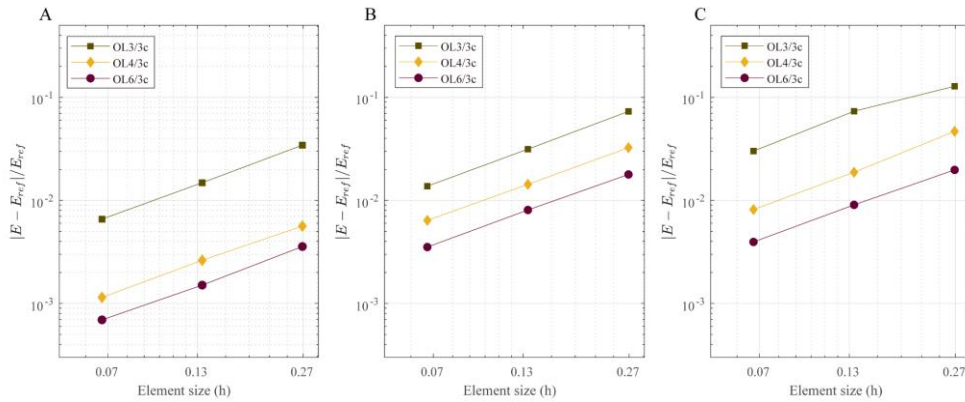


Figure A1.4. The convergence curve of the mixed overlapping element formulated with the continuous pressure approximated by (A) the standard linear shape functions (B) the modified shape function of linearly enriched overlapping element (C) the modified shape function of bilinearly enriched overlapping element.

A2. The profiles of pressure and xx-stress

We plotted the pressure distribution in Figure A2.1, and the xx-stress (τ_{xx}) distribution in Figure A2.2. The pressure and the xx-stress distribution are obtained, respectively, from the pressure solution and the displacement solution of the cantilever plate problem treated in the Section 5.2. The xx-stress distribution obtained from the displacement solution also show smooth profile along the solution domain as well as the pressure distribution directly obtained from the pressure solution.

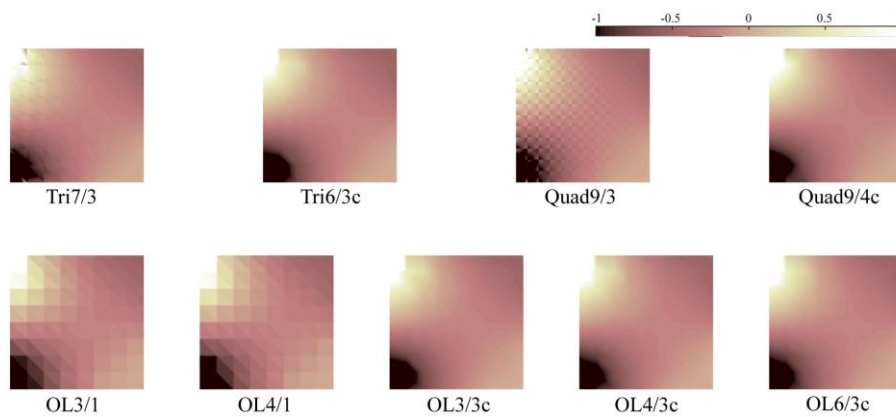


Figure A2.1. The distribution of pressure calculated from the pressure solution.

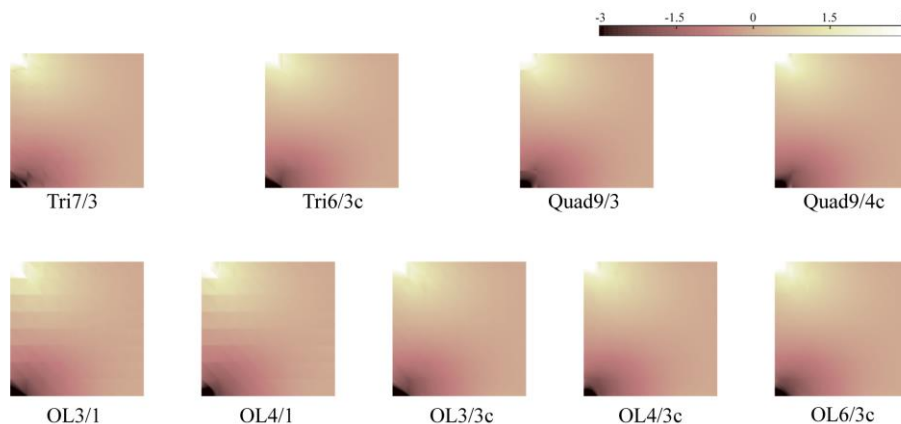


Figure A2.2. The distribution of xx-stress (τ_{xx}) calculated from the displacement solution.

A3. The cantilever plate with material discontinuity

In addition to the simple cantilever plate problem introduced in the Section 5.2, we further examined the performance of each mixed overlapping elements when the material discontinuity are present inside the problem domain. We describe the geometrical and material characteristics of such example problem in the Figure A3.1. The cantilever plate is divided vertically into two different regions with different material properties.

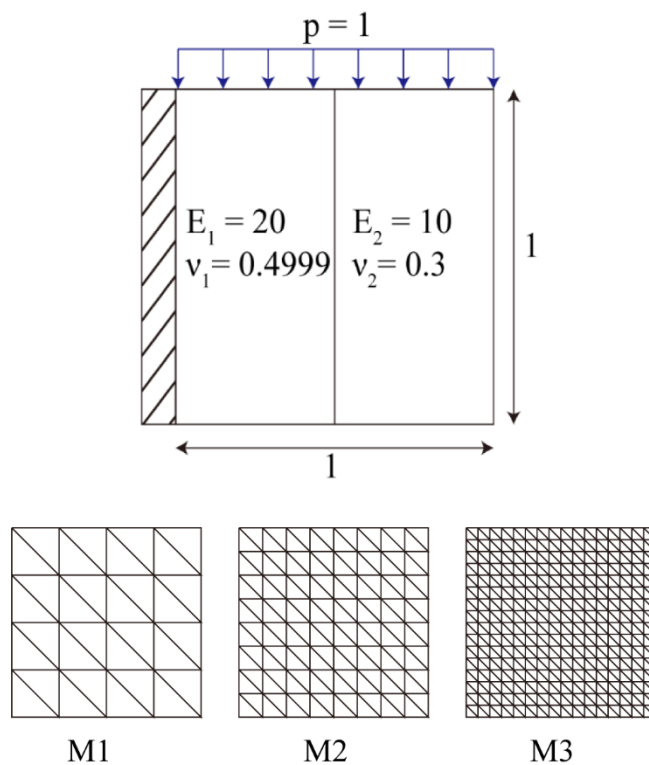


Figure A3.1. Description of the cantilever plate problem with material discontinuity. A set of meshes used in the numerical test is also plotted below the problem description.

The result of the numerical test presented in the Figure A3.2 implies that the proposed mixed overlapping elements also work efficiently compared to the conventional mixed finite elements. The mixed overlapping element ‘OL3/1’ is superior to conventional ‘Tri7/3’ and ‘Tri6/3c’ elements. The accuracy of ‘OL4/3c’ and ‘OL6/3c’ is comparable to conventional quadrilateral mixed finite elements. The pressure profiles (Figure A3.3) of mixed overlapping elements seem stable as the conventional finite elements.

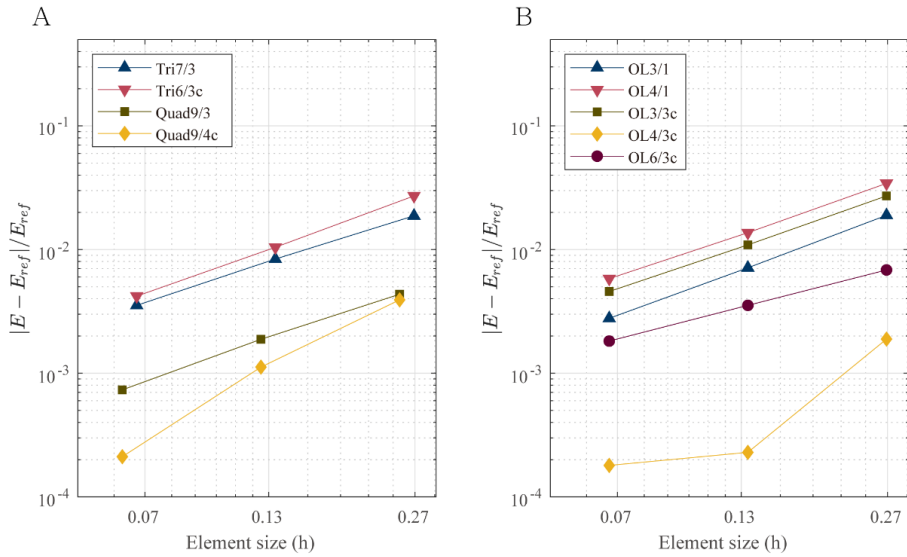


Figure A3.2. The strain energy error of cantilever plate problem with material discontinuity. The convergence curve of (A) the conventional mixed finite elements and (B) the mixed overlapping elements in log scale.

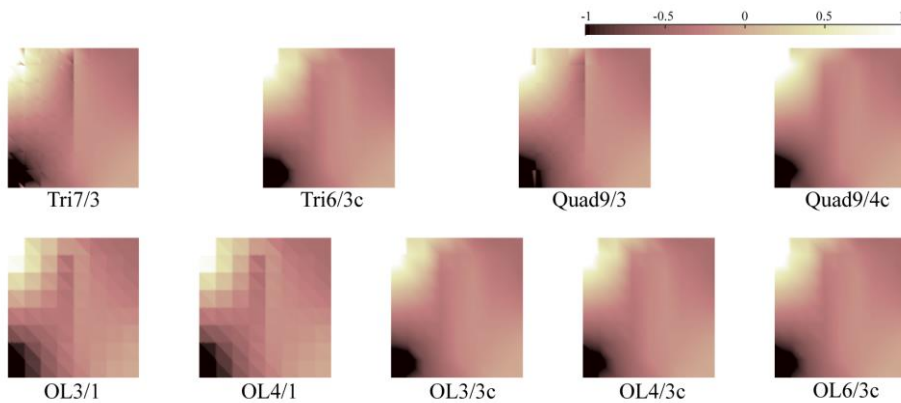


Figure A3.3 The distribution of pressure when material discontinuity are present.

A4. Mesh filtering steps

Molecular surfaces constructed by MSMS usually contain some mesh defects that makes the molecular surfaces inappropriate for FE analysis. Furthermore, surfaces of large molecules tend to have enormous number of faces requiring a large amount of computational time and resources. Therefore, reduction of the number of faces is additionally required for these large structures. The removal of defects and the reduction of the faces are conducted by a bundle of mesh filtering processes. These processes are often repetitive and laborious since each filtering operation frequently induces other types of defects. We use a sequence of filtering algorithms implemented in an open-source mesh processing program: MeshLab version 1.3.3. The filtering processes start with “Merge close vertices” filter to merge all the vertices nearer than the preset threshold. The intersecting faces are removed by “Select self-intersecting faces” and “Delete” options. Likewise, faces attached to the non-manifold edges and non-manifold vertices are removed with “Select non-manifold edges”, “Select non-manifold vertices”, and “Delete” options. Consequently, the surface with holes where the defected faces removed is obtained. The surface with holes is to be filled with proper faces with “Close holes” option. Faces on the boundaries are examined, deleted, and again filled with “Select borders” and “Delete” options in case that the faces are not perfectly filled with “Close holes” option. Lastly, “Remove isolated pieces” filter is applied to eliminate isolated floating components. This filter searches for and eliminate the components whose number of connected faces are less than the user-set value. These series of filtering process is repeated until the input surface meets the condition for proper FE model. The surface conditions for proper FE model are following: non-intersecting, manifold, singlecomponent, and fully closed. In addition, “Quadric edge collapse decimation” filter can be added ahead if the size of the mesh is desired to be reduced. This filter reduces the number of faces as a percentage of the initial size. Since the sudden drop of the mesh size causes many defects, it is recommended to use the percentage value of 0.8 or higher and executed repeatedly until reaching the target number of faces.

A5. Calculation of the diffusion coefficients

The first step is to establish a 6×6 global resistance tensor, Ξ . The resistance tensor is usually defined to express the hydrodynamic resistance of an object⁷⁴. To calculate Ξ from the local nodal actions, we partition the $3M \times 3M$ friction matrix $\tilde{\mathbf{Z}}$ into M^2 3×3 blocks, $\tilde{\mathbf{Z}}^{(i,j)}$, where i and j denote surface nodes. $\tilde{\mathbf{Z}}_{mn}^{(i,j)}$ is the mn component of the 3×3 matrix $\tilde{\mathbf{Z}}^{(i,j)}$, and gives the friction force generated at node i in the m direction ($m=1, 2, 3$) for the unit velocity applied at node j in the n direction ($n=1, 2, 3$).

Then Ξ can be obtained using the following equations

$$\Xi_{\text{tt}} = \sum_i \sum_j \tilde{\mathbf{Z}}^{(i,j)} \quad (\text{A5.1})$$

$$\Xi_{\text{tr}} = \sum_i \sum_j \mathbf{U}_i \tilde{\mathbf{Z}}^{(i,j)} \quad (\text{A5.2})$$

$$\Xi_{\text{rr}} = \sum_i \sum_j \mathbf{U}_i \tilde{\mathbf{Z}}^{(i,j)} \mathbf{U}_j^T \quad (\text{A5.3})$$

$$\Xi = \begin{pmatrix} \Xi_{\text{tt}} & \Xi_{\text{tr}}^T \\ \Xi_{\text{tr}} & \Xi_{\text{rr}} \end{pmatrix} \quad (\text{A5.4})$$

where \mathbf{U}_i is the matrix converting the force components in $\tilde{\mathbf{Z}}^{(i,j)}$ to moment components in Ξ_{tr} about the coordinate axes.

$$\mathbf{U}_i = \begin{pmatrix} 0 & -z_i & y_i \\ z_i & 0 & -x_i \\ -y_i & x_i & 0 \end{pmatrix} \quad (\text{A5.5})$$

Thus Ξ_{tt} , Ξ_{tr} , and Ξ_{rr} are the 3×3 blocks of Ξ which correspond to the friction forces and moments generated for the protein in translation, rotation, and translation-rotation coupling, respectively, and x_i , y_i , and z_i are the coordinates of

node i in the stationary Cartesian reference frame.

The 6×6 diffusion matrix \mathbf{D} that we seek is obtained from Ξ using the generalized Einstein relationship

$$\mathbf{D} = \begin{pmatrix} \mathbf{D}_{tt} & \mathbf{D}_{tr}^T \\ \mathbf{D}_{tr} & \mathbf{D}_{rr} \end{pmatrix} = k_B T \Xi^{-1} \quad (\text{A5.6})$$

where \mathbf{D} , like Ξ , has been also partitioned into 3×3 blocks ⁷⁴. The translational (D_t) and rotational (D_r) diffusion coefficients are then obtained as follows

$$D_t = \frac{1}{3} \text{Tr}(\mathbf{D}_{tt}) \quad (\text{A5.7})$$

$$D_r = \frac{1}{3} \text{Tr}(\mathbf{D}_{rr}) \quad (\text{A5.8})$$

where the symbol Tr indicates the trace of a tensor. Consequently, translational (f_t) and rotational (f_r) friction coefficients can be obtained using the following equations ⁷⁴.

$$f_t = k_B T / D_t \quad (\text{A5.9})$$

$$f_r = k_B T / D_r \quad (\text{A5.10})$$

A6. Integration of Brownian dynamics equation

The Brownian dynamics equations are obtained by neglecting the inertial forces of classical Langevin equation ⁸⁰.

$$\mathbf{Z}\dot{\mathbf{x}} + \mathbf{K}\mathbf{x} = \mathbf{f}(t) \quad (\text{A6.1})$$

The Brownian modes are computed solving the generalized eigenvalue problem.

$$\mathbf{Z}\boldsymbol{\varphi}_i = \tau_i \mathbf{K}\boldsymbol{\varphi}_i \quad (\text{A6.2})$$

where $\boldsymbol{\varphi}_i$ is the i^{th} Brownian mode, and τ_i is the i^{th} eigenvalue, that is, the relaxation time associated with $\boldsymbol{\varphi}_i$.

The Brownian dynamics equation Eq.(A6.1) is solved using the trapezoidal rule, an implicit time integration scheme. For the solution, we rewrite the Brownian dynamics equation into the form

$$\mathbf{Z}\dot{\mathbf{x}} + \mathbf{K}\mathbf{x} = \mathbf{C}d\mathbf{w} \quad (\text{A6.3})$$

$$\mathbf{C} = \begin{bmatrix} \tilde{\mathbf{C}} & \mathbf{0} \\ \mathbf{0} & \mathbf{0} \end{bmatrix} \quad (\text{A6.4})$$

where $\mathbf{f}(t)$ is expressed in a form that we can more easily deal with in the numerical integration.

In Eq.(A6.4), \mathbf{C} is a $3N \times 3N$ matrix and $\tilde{\mathbf{C}}$ is a $3M \times 3M$ matrix, where N denotes the total number of nodes in the protein finite element model. The matrix $\tilde{\mathbf{C}}$ is given by the Cholesky decomposition of $2k_B T \tilde{\mathbf{Z}}$.

$$\tilde{\mathbf{C}}\tilde{\mathbf{C}}^T = 2k_B T \tilde{\mathbf{Z}} \quad (\text{A6.5})$$

The vector $d\mathbf{w}$ is a random vector of Gaussian distribution with zero mean and variance of $1/\Delta t$, where Δt is the time-step size used in the step by step solution. Since this vector is a random vector, we performed multiple Brownian dynamics.

The calculation of the displacement and the velocity vectors is now achieved through the following steps:

- 1) Calculate the effective load vector ${}^{t+\Delta t}\hat{\mathbf{R}}$ at time $t + \Delta t$ using

$${}^{t+\Delta t}\hat{\mathbf{R}} = \mathbf{C}d{}^{t+\Delta t}\mathbf{w} + \mathbf{Z}\left[(2/\Delta t){}^t\mathbf{x} + {}^t\dot{\mathbf{x}}\right] \quad (\text{A6.6})$$

- 2) Solve for the displacement vector ${}^{t+\Delta t}\mathbf{x}$ at time $t + \Delta t$ using

$$\hat{\mathbf{K}}{}^{t+\Delta t}\mathbf{x} = {}^{t+\Delta t}\hat{\mathbf{R}} \quad (\text{where } \hat{\mathbf{K}} = \mathbf{K} + (2/\Delta t)\mathbf{Z}) \quad (\text{A6.7})$$

- 3) Compute the velocity vector ${}^{t+\Delta t}\dot{\mathbf{x}}$ at time $t + \Delta t$ using

$${}^{t+\Delta t}\dot{\mathbf{x}} = (2/\Delta t)\left({}^{t+\Delta t}\mathbf{x} - {}^t\mathbf{x}\right) - {}^t\dot{\mathbf{x}} \quad (\text{A6.8})$$

The time trajectories of a protein finite element model are thus obtained for a predefined simulation duration and time step size.

Bibliography

1. McHenry, D., *A lattice analogy for the solution of stress problems*. Journal of the Institution of Civil Engineers, 1943. **21**(2): p. 59-82.
2. Hrennikoff, A., *Solution of problems of elasticity by the framework method*. Journal of Applied Mechanics, 1941. **8**(4): p. A169-A175.
3. Newmark, N. *Numerical methods of analysis of bars, plates, and elastic bodies*. in *Selected Papers By Nathan M. Newmark: Civil Engineering Classics*. 1949. ASCE. p. 314-344.
4. Southwell, R.V., *Relaxation Methods in Theoretical Physics: A Continuation of the Treatise, Relaxation Methods in Engineering Science*. Vol. 2. 1946: Clarendon Press.
5. Argyris, J.H. and S. Kelsey, *Energy theorems and structural analysis*. Vol. 60. 1960: Springer.
6. Turner, M.J., et al., *Stiffness and deflection analysis of complex structures*. Journal of the Aeronautical Sciences, 1956. **23**(9): p. 805-823.
7. Clough, R.W., *The finite element in plane stress analysis*. Proceedings of the 2nd ASCE Conference On Electric Computation, 1960.
8. Bathe, K.-J., *Finite element procedures*. 1996, Prentice Hall, second edition. 2014: available on the KJ Bathe M.I.T. website.
9. Belytschko, T., Liu, W.K., Moran, B., and Elkhodary, K., *Nonlinear finite elements for continua and structures*. 2013: John Wiley & Sons.
10. Crisfield, M.A., *Finite elements and solution procedures for structural analysis: linear analysis*. Vol. 1. 1986: Pineridge Press.
11. Hughes, T.J., *The finite element method: linear static and dynamic finite element analysis*. 2012: Courier Corporation.
12. Simo, J., *Topics on the Numerical Analysis and Simulation of Plasticity*.

- Handbook of Numerical Analysis, 1998, **6**: p. 183-499.
13. Simo, J.C. and T.J. Hughes, *Computational inelasticity*. Vol. 7. 2006: Springer Science & Business Media.
 14. Kim, J. and Bathe K.-J., *The finite element method enriched by interpolation covers*. Computers & Structures, 2013. **116**: p. 35-49.
 15. Belytschko, T., Lu Y.Y., and Gu L., *Element-free Galerkin methods*. International Journal for Numerical Methods in Engineering, 1994. **37**(2): p. 229-256.
 16. Liu, G.R. and Liu, M.B., *Smoothed particle hydrodynamics: a meshfree particle method*. 2003: World scientific.
 17. De, S. and Bathe, K.-J., *The method of finite spheres*. Computational Mechanics, 2000. **25**(4): p. 329-345.
 18. De, S. and Bathe, K.-J., *The method of finite spheres with improved numerical integration*. Computers & Structures, 2001. **79**(22-25): p. 2183-2196.
 19. De, S. and Bathe, K.-J., *Towards an efficient meshless computational technique: the method of finite spheres*. Engineering Computations, 2001. **18**(1/2): p. 170-192.
 20. Ham, S. and Bathe, K.-J., *A finite element method enriched for wave propagation problems*. Computers & Structures, 2012. **94**: p. 1-12.
 21. Ham, S., B. Lai, and Bathe, K.-J., *The method of finite spheres for wave propagation problems*. Computers & Structures, 2014. **142**: p. 1-14.
 22. Bathe, K.J. and Almeida, C.A., *A simple and effective pipe elbow element—linear analysis*. Journal of Applied Mechanics, 1980. **47**(1): p. 93-100.
 23. Bathe, K.-J., Almeida, C.A., and Ho, L.W., *A simple and effective pipe elbow element—some nonlinear capabilities*. Computers & Structures, 1983. **17**(5-6): p. 659-667.
 24. Bathe, K.-J. and Almeida C.A., *A simple and effective pipe elbow element—interaction effects*. Journal of Applied Mechanics, 1982. **49**(1): p.

- 165-171.
25. Bathe, K.-J. and Chaudhary A., *On the displacement formulation of torsion of shafts with rectangular cross-sections*. International Journal for Numerical Methods in Engineering, 1982. **18**(10): p. 1565-1568.
 26. Moës, N. and Belytschko T., *Extended finite element method for cohesive crack growth*. Engineering fracture mechanics, 2002. **69**(7): p. 813-833.
 27. Melenk, J.M. and Babuška I., *The partition of unity finite element method: basic theory and applications*. Computer methods in applied mechanics and engineering, 1996. **139**(1-4): p. 289-314.
 28. Babuška, I. and Melenk J.M., *The partition of unity method*. International Journal for Numerical Methods in Engineering, 1997. **40**(4): p. 727-758.
 29. Zhang, L. and Bathe, K.-J., *Overlapping finite elements for a new paradigm of solution*. Computers & Structures, 2017. **187**(15): p. 64-76.
 30. Zhang, L., Kim K.-T., and Bathe, K.-J., *The new paradigm of finite element solutions with overlapping elements in CAD—Computational efficiency of the procedure*. Computers & Structures, 2018. **199**(1): p. 1-17.
 31. Huang, J. and Bathe, K.-J., *Quadrilateral overlapping elements and their use in the AMORE paradigm*. Computers & Structures, 2019. **222**(1): p. 25-35.
 32. Huang, J. and Bathe, K.-J., *On the convergence of overlapping elements and overlapping meshes*. Computers & Structures, 2021. **244**: 106429.
 33. Bathe, K.-J., *The AMORE paradigm for finite element analysis*. Advances in Engineering Software, 2019. **130**: p. 1-13.
 34. Bathe, K.-J. and L. Zhang, *The finite element method with overlapping elements—a new paradigm for CAD driven simulations*. Computers & Structures, 2017. **182**(1): p. 526-539.
 35. Atluri, S.N., Gallagher R.H., and Zienkiewicz O.C., *Hybrid and mixed finite element methods(Book)*.1983: Wiley-Interscience.
 36. Strang, G. and Fix G.J., *An analysis of the finite element method(Book- An analysis of the finite element method.)*. 1973: Prentice-Hall.

37. Zienkiewicz, O., Taylor, R., and Baynham, J., *Mixed and irreducible formulations in finite element analysis*. 1983: John Wiley & Sons.
38. Brezzi, F. and Fortin M., *Mixed and hybrid finite element methods*. Vol. 15. 2012: Springer Science & Business Media.
39. Hansbo, P. and Larson M.G., *Discontinuous Galerkin and the Crouzeix–Raviart element: application to elasticity*. ESAIM: Mathematical Modelling and Numerical Analysis, 2003. **37**(1): p. 63-72.
40. Hughes, T.J., Franca L.P., and Balestra M., *A new finite element formulation for computational fluid dynamics: V. Circumventing the Babuška-Brezzi condition: A stable Petrov-Galerkin formulation of the Stokes problem accommodating equal-order interpolations*. Computer methods in applied mechanics and engineering, 1986. **59**(1): p. 85-99.
41. Auricchio, F., Beirão da Veiga L., Brezzi, F., Lovadina, C., *Mixed finite element methods*. Encyclopedia of Computational Mechanics Second Edition, 2017: John Wiley & Sons.
42. Lovadina, C., *Analysis of strain-pressure finite element methods for the Stokes problem*. Numerical Methods for Partial Differential Equations: An International Journal, 1997. **13**(6): p. 717-730.
43. Apel, T. and Nicaise S., *The inf-sup condition for low order elements on anisotropic meshes*. Calcolo, 2004. **41**(2): p. 89-113.
44. Apel, T., Nicaise S., and Schöberl J., *Crouzeix-Raviart type finite elements on anisotropic meshes*. Numerische Mathematik, 2001. **89**(2): p. 193-223.
45. Apel, T. and Randrianarivony H.M., *Stability of discretizations of the Stokes problem on anisotropic meshes*. Mathematics and Computers in Simulation, 2003. **61**(3-6): p. 437-447.
46. Babuška, I., *The finite element method with Lagrangian multipliers*. Numerische Mathematik, 1973. **20**(3): p. 179-192.
47. Brezzi, F., *On the existence, uniqueness and approximation of saddle-point problems arising from Lagrangian multipliers*. Publications mathématiques et informatique de Rennes, 1974. **S4**: p. 1-26.

48. Chapelle, D. and Bathe, K.-J., *The inf-sup test*. Computers & Structures, 1993. **47**(4-5): p. 537-545.
49. Sukumar, N. and Malsch E., *Recent advances in the construction of polygonal finite element interpolants*. Archives of Computational Methods in Engineering, 2006. **13**(1): p. 129-163.
50. Sukumar, N. and Tabarraei A., *Conforming polygonal finite elements*. International Journal for Numerical Methods in Engineering, 2004. **61**(12): p. 2045-2066.
51. Chai, Y. and Bathe, K.-J., *Transient wave propagation in inhomogeneous media with enriched overlapping triangular elements*. Computers & Structures, 2020. **237**: 106273.
52. Kim, K.-T., Zhang L., and Bathe, K.-J., *Transient implicit wave propagation dynamics with overlapping finite elements*. Computers & Structures, 2018. **199**: p. 18-33.
53. Löhner, R. and Parikh P., *Generation of three-dimensional unstructured grids by the advancing-front method*. International Journal for Numerical Methods in Fluids, 1988. **8**(10): p. 1135-1149.
54. Shenton, D. and Cendes Z., *Three-dimensional finite element mesh generation using Delaunay tessellation*. IEEE Transactions on Magnetics, 1985. **21**(6): p. 2535-2538.
55. Crouzeix, M. and Raviart P.-A., *Conforming and nonconforming finite element methods for solving the stationary Stokes equations I*. ESAIM: Mathematical Modelling and Numerical Analysis-Modélisation Mathématique et Analyse Numérique, 1973. **7**(R3): p. 33-75.
56. Taylor, C. and Hood P., *A numerical solution of the Navier-Stokes equations using the finite element technique*. Computers & Fluids, 1973. **1**(1): p. 73-100.
57. Bercovier, M. and Pironneau O., *Error estimates for finite element method solution of the Stokes problem in the primitive variables*. Numerische Mathematik, 1979. **33**(2): p. 211-224.

58. Cook, R.D., *Improved two-dimensional finite element*. Journal of the Structural Division, 1974. **100**(9): p. 1851-1863.
59. García, A.E. and Harman J.G., *Simulations of CRP:(cAMP) 2 in noncrystalline environments show a subunit transition from the open to the closed conformation*. Protein science, 1996. **5**(1): p. 62-71.
60. Chennubhotla, C., Rader, A.J., Yang, L.-W., and Bahar, I., *Elastic network models for understanding biomolecular machinery: from enzymes to supramolecular assemblies*. Physical biology, 2005. **2**(4): p. S173.
61. Brünger, A.T., Kuriyan J., and Karplus M., *Crystallographic R factor refinement by molecular dynamics*. Science, 1987. **235**(4787): p. 458-460.
62. De Groot, B., Hayward, S., van Aalten, D.M.F., Amadei, A., and Berendsen, H.J.C., *Domain motions in bacteriophage T4 lysozyme: a comparison between molecular dynamics and crystallographic data*. Proteins: Structure, Function, and Bioinformatics, 1998. **31**(2): p. 116-127.
63. Levitt, M., Sander C., and Stern P.S., *The normal modes of a protein: Native bovine pancreatic trypsin inhibitor*. International Journal of Quantum Chemistry, 1983. **24**(S10): p. 181-199.
64. Bathe, M., *A finite element framework for computation of protein normal modes and mechanical response*. Proteins: Structure, Function, and Bioinformatics, 2008. **70**(4): p. 1595-1609.
65. Kim, D.-N., Nguyen C.-T., and Bathe M., *Conformational dynamics of supramolecular protein assemblies*. Journal of structural biology, 2011. **173**(2): p. 261-270.
66. Kim, J., Kim J.-G., Yun, G., Lee, P.-S., and Kim, D.-N., *Toward modular analysis of supramolecular protein assemblies*. Journal of chemical theory and computation, 2015. **11**(9): p. 4260-4272.
67. Yun, G., Kim, J., and Kim D.-N., *A critical assessment of finite element modeling approach for protein dynamics*. Journal of computer-aided molecular design, 2017. **31**(7): p. 609-624.
68. Sedeh, R.S., Yun, G., Lee, J.Y., Bathe, K.-J., and Kim, D.-N., *A framework*

- of finite element procedures for the analysis of proteins.* Computers & Structures, 2018. **196**: p. 24-35.
69. Connolly, M.L., *The molecular surface package.* Journal of molecular graphics, 1993. **11**(2): p. 139-141.
70. Sanner, M.F., Olson A.J., and Spehner J.C., *Reduced surface: an efficient way to compute molecular surfaces.* Biopolymers, 1996. **38**(3): p. 305-320.
71. Cignoni, P., Callieri, M., Corsini, M., Dellepiane, M., Ganovelli, F., and Ranzuglia, G., *Meshlab: an open-source mesh processing tool.* in *Eurographics Italian chapter conference.* 2008. Salerno, Italy.
72. The ADINA finite element program (2017). ADINA R&D, I., Watertown, MA, USA. www.adina.com.
73. Brooks, B.R., Bruccoleri, R.E., Olafson, B.D., States, D.J., Swaminathan, S., and Karplus, M., *CHARMM: a program for macromolecular energy, minimization, and dynamics calculations.* Journal of computational chemistry, 1983. **4**(2): p. 187-217.
74. Carrasco, B. and de la Torre J.G., *Hydrodynamic properties of rigid particles: comparison of different modeling and computational procedures.* Biophysical journal, 1999. **76**(6): p. 3044-3057.
75. de la Torre, J.G., Huertas M.L., and Carrasco B., *Calculation of hydrodynamic properties of globular proteins from their atomic-level structure.* Biophysical journal, 2000. **78**(2): p. 719-730.
76. Miller, B.T., Zheng, W., Venable, R.M., Pastor, R.W., and Brooks, B.R., *Langevin network model of myosin.* The Journal of Physical Chemistry B, 2008. **112**(19): p. 6274-6281.
77. Vaney, M., Maignan, S., Riès-Kautt, M., and Ducruix, A., *High-resolution structure (1.33 Å) of a HEW lysozyme tetragonal crystal grown in the APCF apparatus. Data and structural comparison with a crystal grown under microgravity from SpaceHab-01 mission.* Acta Crystallographica Section D: Biological Crystallography, 1996. **52**(3): p. 505-517.
78. Kim, Y., Eom, S.H., Wang, J., Lee, D.-S., Suh, S.W., and Steitz, T.A.,

- Crystal structure of Thermus aquaticus DNA polymerase.* Nature, 1995. **376**(6541): p. 612-616.
79. Bartolucci, C., Lamba, D., Grazulis, S., Manakova, E., Heumann, H., *Crystal structure of wild-type chaperonin GroEL.* Journal of molecular biology, 2005. **354**(4): p. 940-951.
80. Kottalam, J. and Case D., *Langevin modes of macromolecules: applications to crambin and DNA hexamers.* Biopolymers: Original Research on Biomolecules, 1990. **29**(10-11): p. 1409-1421.

국 문 초 록

유한요소법은 공학 분야의 복잡한 미분 방정식을 해결하는데 유용한 견고하고 효율적인 수치 기법이다. 하지만 유한요소법의 필수 절차인 메쉬 생성 과정은 많은 번거로움이 수반된다. 복잡한 형상을 갖는 물체를 사각형 또는 육면체 메쉬로 구성하는 것은 매우 어려우며, 때로는 불가능하기도 하다. 한편 원하는 정확도의 결과를 얻기 위해 고차 요소를 사용한다면 계산 비용 측면에서 불리해진다. 또한 메쉬의 세밀도 및 적절한 보간 차수를 결정하는 것은 추가적인 노력이 수반된다. 간단한 삼각형 또는 삼각뿔 메쉬를 이용하면서 동시에 높은 정확도를 달성할 수 있다면, 메쉬의 생성 측면 그리고 계산의 효율성에 있어서 이상적일 것이다. 본 연구에서는 최근 제시된 오버래핑 요소를 활용하여 이러한 메쉬의 어려움과 계산 비용 문제를 극복하고자 한다.

비압축성 구조 해석은 계산 효율 측면에 있어 또 다른 어려운 과제이다. 비압축성 해석은 변위-압력 혼합법을 활용하는데, 이러한 혼합요소는 요소의 정확성에 더불어 안정성의 측면도 고려해야 한다. 혼합요소의 안정성을 고려하면 고전적인 방법으로는 높은 차수의 요소의 활용이 불가피하며 이는 계산 효율에 불리하게 작용한다.

본 연구에서는 오버래핑 요소를 변위-압력 혼합법과 조합하여 효율적인 비압축성 구조 해석법을 제시하고자 한다. 오버래핑 요소는 간단한 낮은 차수의 삼각형 또는 삼각뿔 메쉬를 활용하되, 변위의 함수 공간이 로컬 필드 함수와 확장 함수에 의해 확장되기 때문에 요소의 안정성을 유지하면서 변위-압력 혼합법 적용이 가능하다. 이에, 혼합오버래핑 요소에 활용될 수 있는 변위/압력 변수 개수의 조합들을 제시하고 각각의 조합에 대한 안정성 테스트를 진행하여 안정적인 조합들을 도출한다. 더불어 선정된 안정적인 혼합오버래핑 요소에 대한 예제 문제 풀이를 통해 고전적 혼합요소 대비 정확하고 효율적인 요소들을 선정한다. 마지막으로 단백질 동역학을 다루는 3차원 문제에 혼합오버래핑 요소를 적용하여 개발된 요소의 활용 예시로 소개한다. 해당 문제에 혼합오버래핑 요소를 적용하여 정확성을 유지한 채 높은 계산 효율을 달성할 수 있다.

주요어 : 유한요소법, 향상된 유한 요소, 오버래핑 요소,
혼합유한요소법, 혼합오버래핑 요소의 안정성

학 번 : 2016-33943